Design and Implementation of the Tip/Tilt Compensation System for Raven, a Multi-Object Adaptive Optics System

by

Reston Nash
B.Eng, University of Victoria, 2010

A Thesis Submitted in Partial Fulfillment
of the Requirements for the Degree of

MASTER OF APPLIED SCIENCE

in the Department of Mechanical Engineering

SUPERVISORY COMMITTEE

Design and Implementation of the Tip/Tilt Compensation System for Raven, a Multi-Object Adaptive Optics System

by

Reston Nash
B.Eng, University of Victoria, 2010

Supervisory Committee

Dr. Colin Bradley (Department of Mechanical Engineering)
Co-Supervisor

Dr. Pan Agathoklis (Department of Electrical Engineering)
Co-Supervisor

ABSTRACT

Supervisory Committee
Dr. Colin Bradley (Department of Mechanical Engineering)
Co-Supervisor
Dr. Pan Agathoklis (Department of Electrical Engineering)
Co-Supervisor

Multi-Object Adaptive Optics promises to be a useful tool for the upcoming class of Extremely Large Telescopes. Like current adaptive optics systems, MOAO systems compensate optical aberrations caused by atmospheric turbulence, but with the added benefit of being able to compensate multiple portions of a telescope's field at the same time. To ensure the success of the eventual MOAO systems built for the ELTs, several demonstrator instruments have been designed and tested on current telescopes. Raven is one of these demonstrators, designed by the University of Victoria Adaptive Optics Lab for the Subaru 8.2 meter telescope to feed the InfraRed Camera and Spectrograph. Raven corrects the light of two science targets using wavefront information from three natural guide stars, and a single laser guide star. The topic of this thesis is the design and implementation of Raven's tip/tilt compensation system, used to stabilize the output image positions on IRCS's 0.140" slit. Tip/tilt correction of the science targets is done using a combination of motorized pick-off arms, piezoelectric tip/tilt platforms, and deformable mirrors. Through digital filtering and calibration, it is shown that these actuators are able to collectively keep the output science images stationary during simulated laboratory observations. A performance reduction due to residual tip/tilt errors is expected to be less than 5%. Raven goes on-sky in mid-2014, and it will be the first MOAO instrument to attempt scientific observations.

TABLE OF CONTENTS

LIST OF TABLES

LIST OF FIGURES

NOMENCLATURE

Units

Symbol	Name	Notes
°	degree	
rad	radian	
'	arcminute	1/60 of a degree. Used for large, on-sky measurements.
"	arcsecond	1/3600 of a degree. Used for small, on-sky measurements.
m	meter	
mm	millimeter	10^{-3} of a meter
μm	micron	10^{-6} of a meter
Hz	Hertz	Cycles per second
kHz	Kilohertz	1000 cycles per second

Acronyms

AO	Adaptive Optics
AOS	Adaptive Optics Sequencer
AO188	Subaru 188 actuator AO system
CCD	Charge-Coupled Device
CDM	Calibration Deformable Mirror
CLWFS	Closed-Loop Wavefront Sensor
CU	Calibration Unit
DM	Deformable Mirror
EE	Ensquared Energy
ELT	Extremely Large Telescope
EMCCD	Electron Multiplying Charge-Coupled Device
FoV	Field of View
FoR	Field of Regard
IR	Infrared
IRCS	Subaru Infrared Camera and Spectrograph
LGS	Laser Guide Star
LWP	Long Wave Pass beam splitter
MOAO	Multi-Object Adaptive Optics System
NAOJ	National Astronomical Observatory of Japan
NGS	Natural Guide Star
OLWFS	Open-loop Wavefront Sensor
RTC	Real-Time Computer
SDM	Science Deformable Mirror
T/T	Tip/Tilt
TTP	Tip/Tilt Platform
WFS	Wavefront Sensor

1 INTRODUCTION

The age of the **extremely large telescopes** (ELTs) is dawning. This new class of optical telescope will utilize primary mirrors larger than 20 meters in diameter; more than double the size of the current class of very large telescopes (VLTs). The three planned ELTs are: the European Extremely Large Telescope (E-ELT)[1], having a 42 m primary mirror, the Thirty Meter Telescope (TMT)[2], having a 30 m primary mirror, and the Giant Magellan Telescope (GMT)[3], having an effective primary mirror diameter of 21m. Two fundamental motivations exist for creating a larger telescope. First, the primary mirror's light collecting area increases with the square of its diameter, decreasing the required exposure time for a given observation. Second, a telescope's resolution is directly proportional to its primary mirror diameter, so data collected with a larger telescope can be examined with finer detail. The formula for the maximum achievable angular resolution of a telescope, known as the **diffraction limit**, is given by Eqn. 1-1.

$$R_{\text{Diffraction}} = 1.22 \frac{\lambda}{D}$$

Where R is the diffraction limited angular resolution of the telescope, λ is the observing wavelength, and D is diameter of the telescope's primary mirror. Theoretically, a bigger telescope is a better telescope, as larger primary mirrors should provide better resolution. However, Eqn. 1-1 assumes that the primary mirror size is the only factor limiting resolution, ignoring a wide range of issues that would drastically inhibit it, if left uncorrected. It is therefore the responsibility of a telescope's engineering team to ensure that their devices allow their telescope to operate as close to the diffraction limit as possible. One of the main challenges facing astrophysical instrument designers is counteracting the optical impact of the turbulence in the air above the telescope. Consequently, all of the proposed ELTs will be outfitted with sophisticated **adaptive optics** (AO) systems.

AO technology has been very successful on the VLTs, providing remarkable improvements to their resolution and overall functionality. However, new AO system architectures will be required to use ELTs to their full potential. **Multi-Object Adaptive Optics** (MOAO) systems are one of several promising advancements in the AO field that are expected to work well with ELTs. As this method is relatively new, successful demonstrations are required. Doing this builds confidence, while forcing engineers to confront fundamental design challenges. Several MOAO demonstrators have been built with a wide range of technical mandates. The most recent MOAO demonstrator is **Raven**[4], being designed and built by the University of Victoria Adaptive Optics Lab for the Subaru 8.2m telescope. Raven will be installed on Subaru's infrared (IR) Nasmyth platform where it will receive light from the telescope, restore its resolution, and pass it to Subaru's **InfraRed Camera and Spectrograph** (IRCS).

This thesis presents the design and implementation of Raven's **tip/tilt compensation system**. Tip/tilt (T/T) errors are the most basic optical aberration, and are similar to the effects observed when a movie is shot with a shaky camera. Tilting the camera causes the recorded image to shift from the target, but the overall resolution stays the same. When

observing with large telescopes, there are a variety of potential sources of tip/tilt error including: atmospheric turbulence, telescope tracking error, field rotation, and differential atmospheric refraction. Conversely, there are several methods and devices for compensating tip/tilt. Creating an efficient and robust tip/tilt compensation system for Raven is the ultimate goal of the research presented here. An overview of Subaru's design, spectroscopy, atmospheric turbulence, adaptive optics, and MOAO technology, is required before a detailed description of Raven can be presented.

1.1 DESCRIPTION OF THE SUBARU TELESCOPE

The Subaru Telescope is an optical-infrared reflecting telescope, built in a Ritchey-Chretien configuration[5]. It has an 8.2m diameter primary mirror, providing a diffraction limit of 0.050" in H-Band ($\lambda = 1.5 - 1.8\mu m$). Its usable field of view is 3.5'[a] and it has a plate-scale of 0.532mm/"[b]. Subaru is operated by The National Astronomical Observatory of Japan (NAOJ), and is located at the 4200 m summit of Mauna Kea, on the Big Island of Hawaii. A diagram of Subaru is shown in Figure 1-1.

---

[a] About 10% the angular diameter of the moon

[b] Arcminutes are usually denoted by a ' symbol and arcseconds by a " symbol. 60 arcseconds are in an arcminute and 60 arcminutes are in a degree
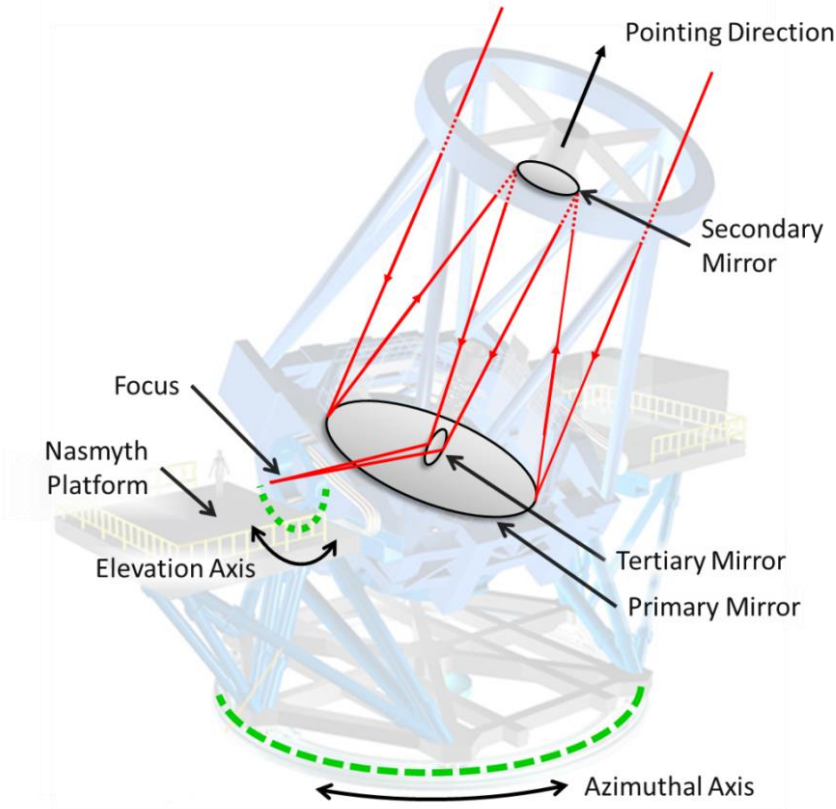
Figure 1-1: The Subaru Telescope. Astronomical light (shown in red) enters the telescope and reflects off the 8.2m primary mirror, then the secondary and tertiary mirrors. The light finally forms a focus on the Nasmyth platform. Subaru is mounted on an altazimuthal mount for altering its pointing direction (bearing axes shown as dashed green lines)

Light entering Subaru first reflects off a concave primary mirror, and then reflects off a convex secondary mirror, before finally reflecting off a flat tertiary mirror. The light is passed coaxially through the bearing of the telescope's elevation axis, finally forming a focus on the Nasmyth Platform. Subaru has two Nasmyth Platforms, one for observing in the visible spectrum and one for observing in the infrared (IR). The telescope is mounted on a motorized **altazimuthal mount** to alter its pointing direction. This type of mount consists of a horizontal rotation axis for changing elevation angle, mounted on a vertical rotation axis for changing the azimuthal angle. The Nasmyth Platforms are coupled to the azimuthal axis, so instruments placed on them will remain level regardless of the telescope's pointing direction.

Subaru's facility AO system, AO188, operates on the IR Nasmyth Platform, where it accepts light from the telescope and passes it to IRCS. Similarly, Raven is designed for

use on the IR Nasmyth Platform, and will also feed IRCS. As IRCS is a spectrograph, an overview of spectroscopy is given in the next section.

1.2 SUMMARY OF ASTRONOMICAL SPECTROSCOPY

A spectrograph is device used to determine an astronomical target's composition and velocity[c], by analyzing its observed wavelength spectrum (its color). A simple schematic of a spectrometer is shown in Figure 1-2. IRCS functions in a similar fashion.
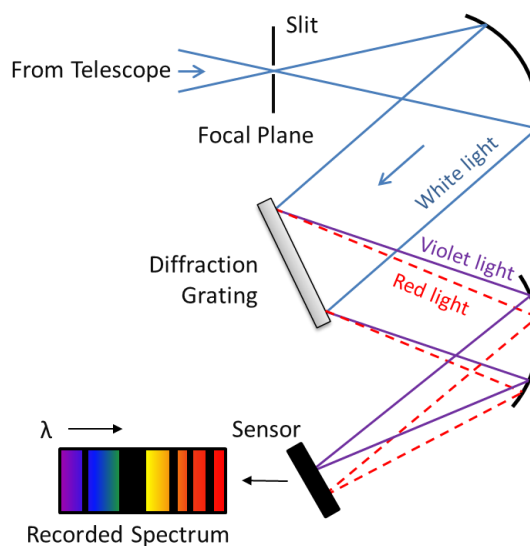
Figure 1-2: Schematic of a spectrometer. A portion of the light from the telescope's focal plane passes through a slit. The light is collimated and reflected off a diffraction grating that splits the light into its spectrum, so its spectral intensity can be recorded with a sensor.

A narrow slit in the telescope's focal plane acts as a line source for the remainder of the spectrometer. Light from the slit is first collimated, and then reflected off a diffraction grating, which splits the light into its spectrum. The recorded intensity profile will indicate the wavelengths emitted by the target. As an example, the spectrum of a Helium lamp is shown in Figure 1-3.

---

[c] Specifically, the objects radial velocity towards or away from Earth
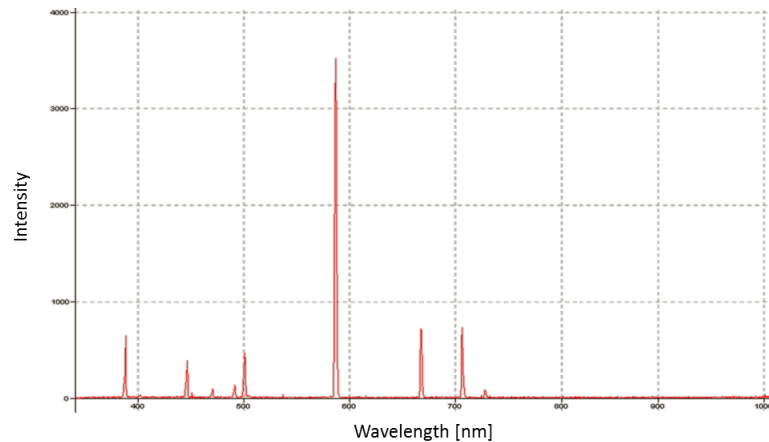
Figure 1-3: Wavelength Spectrum of a Helium lamp

Comparing the recorded intensity spikes to accepted data can indicate the material composition of the object. If the object is moving towards or away from the observer, the Doppler Effect will shift the observed wavelength spectrum. By measuring the shift of the measured spectra compared to accepted data, the object's radial velocity can be calculated. Determining the composition and velocity of astronomic objects is very important for understanding astrophysical and cosmological processes.

When performing spectroscopy, the responsibility of the telescope and AO system is to pass the maximum amount of available scientific light though the spectrograph's slit. Choosing the slit size is a trade-off; thinner slits provide higher spectral resolution, but require longer exposure times as less light can be collected. IRCS's slit width is 0.140", just under three times Subaru's diffraction limit. **Ensquared energy** is a metric commonly used for quantifying an AO instrument's efficiency for delivering science light into a rectangular aperture, such as a slit.

1.3 ENSQUARED ENERGY

Ensquared energy (EE) is the metric used to quantify Raven's overall performance. It is defined as the ratio between the amount of light passed through a rectangular aperture during operation, compared to the amount of light that would be passed through the same aperture if the system was operating at its diffraction limit. For an AO system feeding a spectrograph, the EE would be the ratio of light entering the slit, compared to how much

would enter if the system was functioning perfectly. Figure 1-4 shows what different EE values might look like.
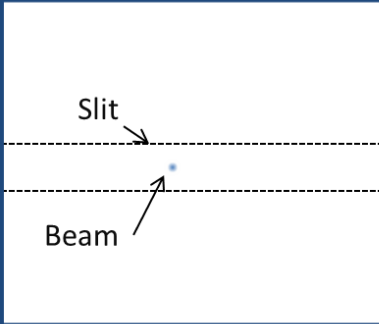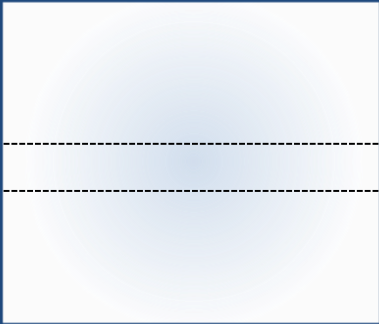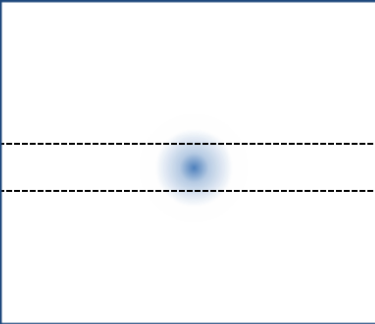
Atmosphere Removed	Without AO Correction	With AO Correction
Slit ↘ ------------------- • ↗ Beam		
EE=95%	EE=10%	EE=75%

Figure 1-4: Examples of different values of ensquared energy. Science light is shown in blue, and the dashed black line indicates the slit.

In spectroscopy, a large percentage EE means more light is going through the slit, allowing an object's spectra to be recorded with minimal exposure time. Optical aberrations from atmospheric turbulence will reduce EE of any large telescope.

Other methods exist for measuring an AO system's performance. The Strehl ratio and the full-width-at-half-max, are both commonly used. However, these methods lend themselves better to instruments used for recording high-contrast images, and not spectral analysis.

1.4 LIGHT PROPAGATION THROUGH THE ATMOSPHERE

1.4.1 SPATIAL STRUCTURE OF ATMOSPHERIC TURBULENCE

Light from an astronomic target emanates in all directions, forming spherical wavefronts. A **wavefront** represents a surface of light created at the same time by the same source. Over the vast distances in space, these spheres become large enough that sections can be approximated as planar, and a planar wavefront is a fundamental requirement for a telescope instrument to operate at its diffraction limit. As the telescope-bound light travels from space it eventually reaches Earth's atmosphere. Once in the atmosphere, the light's once planar wavefront becomes distorted, taking on a rippled

shape. The distortion is due to the temperature dependence of air's refractive index[6], meaning light traveling through different air temperatures will have different velocities. Within the atmosphere, horizontal layers of approximately constant temperature air are turbulently mixed together at their boundaries, creating a non-uniform air temperature profile above the telescope. Figure 1-5 summarizes this process.
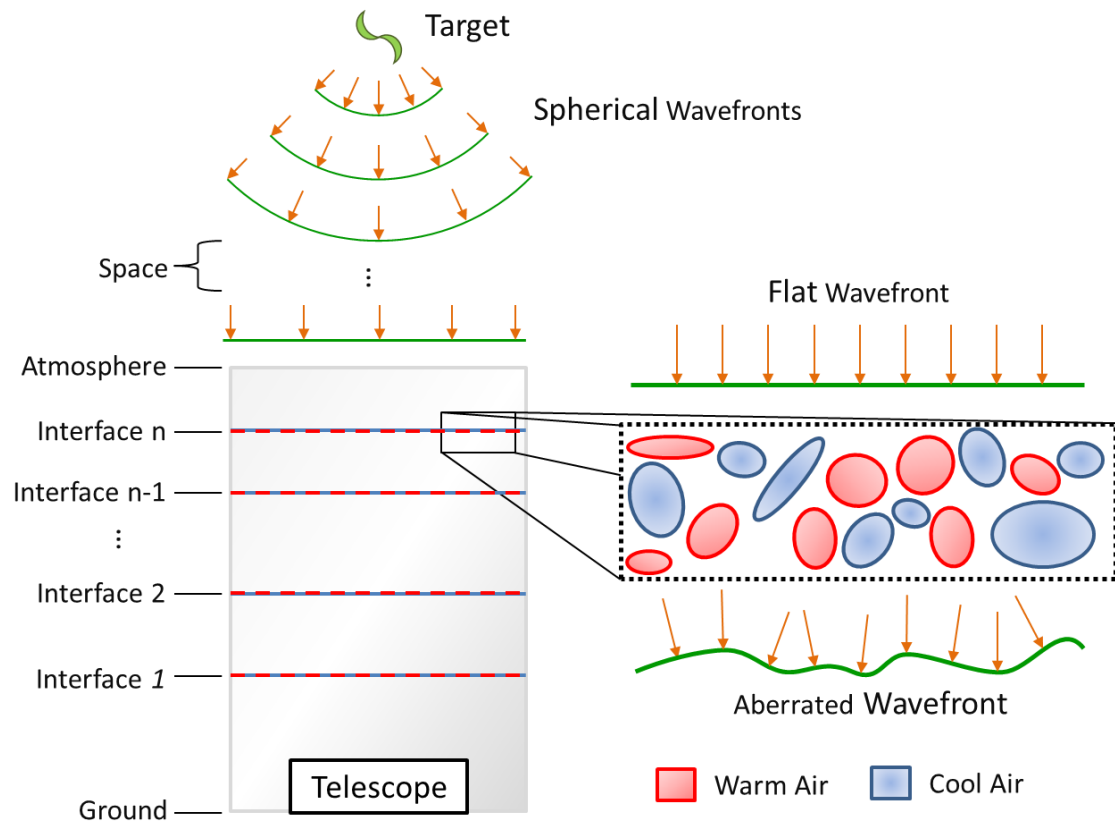
Figure 1-5: Light propagating from a star through the atmosphere. Wavefronts (green), become planar over the large distances of space. Upon entering the atmosphere they become distorted at the turbulent interfaces of atmospheric air layers

Evaluating the effects of atmospheric wavefront aberrations on an observation requires an understanding of turbulence, light propagation, and resolution. Starting with the relationship between turbulence and light propagation, the spatial variance of air's refractive index is defined by the **index structure function**, shown in Eqn. 1-2.

$$D_N(\boldsymbol{\rho}) = \langle |n(\boldsymbol{r}) - n(\boldsymbol{r} + \boldsymbol{p})|^2 \rangle \qquad \textbf{1-2}$$

Where $n(\boldsymbol{r})$ is the refractive index of a point of air at location $\boldsymbol{r}$, and $n(\boldsymbol{r} + \boldsymbol{p})$ is the refractive of a point of air spatially separated from the first point by distance $\boldsymbol{p}$. Assuming the atmospheric refractive index fluctuations are homogenous and isotropic, this index structure function be combined with the Kolmogorov-Obukhov laws of turbulence[7], and can be reduced to Eqn. 1-3.

$$D_N(\rho) = C_N^2 \rho^{2/3}; \ l_0 \ll \rho \ll L_0 \qquad \qquad \textbf{1-3}$$

The newly introduced term C_N^2 is known as the **index structure constant**[d], and is a measure of the energy of the local refractive index inhomogeneities. The simplifications of Eq. 1-3 are only valid when the separation distance ρ is between the smallest and largest turbulent structure sizes. Outside of these values, known as the **inner scale** (l_0) and **outer scale** (L_0), the Kolmogorov laws do not accurately represent real turbulence.

Several different numeric approximations exist for the C_N^2 profile as a function of altitude (h), with a common representation being the **Hufnagel-Valley model**[8, 9] given by:

$$C_N^2(h) = A\left[2.2 \times 10^{-23} h^{10} \exp(-h)\left(\frac{V_w}{\overline{V_w}}\right)^2 + 10^{-16}\exp(-h/1.5)\right] \qquad \textbf{1-4}$$

Where A is a scaling factor, and $V_w/\overline{V_w}$ is the ratio of the wind speed at 10km to the average wind speed in the upper atmosphere. Figure 1-6 shows the form of C_N^2 using Eqn. 1-4 with values determined by Olivier[10] based on measurements from Roddier[11] for the summit of Mauna Kea. It can be seen that the values for C_N^2 are highest in the first few hundred meters of altitude, referred to as the ground layer of turbulence.

---

[d] Though its name may suggest otherwise, the index structure constant is not a constant value, but a function of altitude that can drastically vary with time
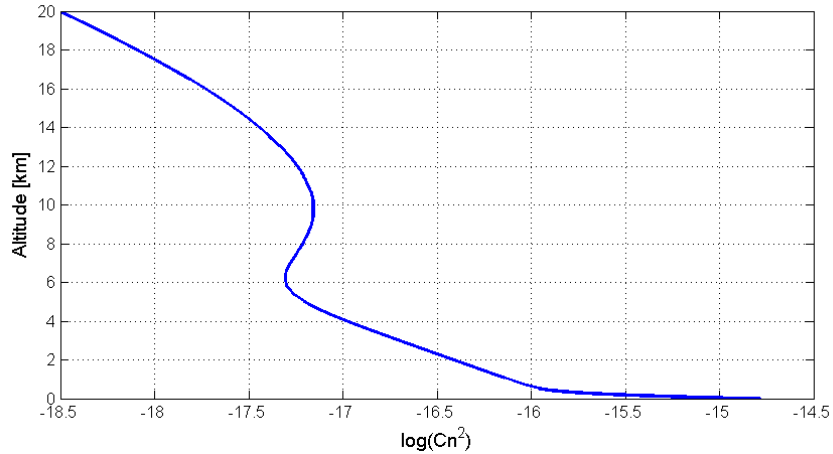
Figure 1-6: Refractive-index structure function for the Hilo airport using the Hufnagel-Valley model. Most of the atmospheric energy is in the first few hundred meters, referred to as ground layer turbulence

The previous formulas have not been especially useful for telescope designers. Fried took the crucial step of combing them with optical resolution formulas, resulting in the Fried parameter[12], r_0, which is one of the most important terms in adaptive optics. The formula for r_0 is shown in Eqn. 1-5.

$$r_0 = 0.185\lambda^{6/5}\left[\sec(\phi)\int C_N^2(h)\,\mathrm{d}h\right]^{-3/5} \qquad \textbf{1-5}$$

Where λ is the observed wavelength, and ϕ is the zenith angle of the target (the telescope's pointing angle measured from vertical). The Fried parameter was explicitly formulated to determine the maximum aperture diameter before atmospheric conditions would significantly impact image quality. This definition leads to Eqn. 1-6 for the **seeing limit**, which is the maximum achievable angular resolution when observing through an atmosphere without AO correction.

$$R_{\text{Seeing}} = \frac{\lambda}{r_0} \qquad \textbf{1-6}$$

Unlike the formula for the diffraction limit, the seeing limit is not dependent on the telescope's primary mirror size. As an example, if atmospheric effects are not corrected, a telescope with a 30m primary mirror looking through an atmosphere with an r_0 of 15cm

would have the same resolution as a telescope with a 15cm primary mirror. The Fried parameter is conventionally given in centimeters at a wavelength of 500nm. The $\lambda^{6/5}$ term in its definition indicates observing at longer wavelengths will provide a larger r_0 and potentially higher resolution images. Consequently AO systems typically observe using infrared light instead of visible light. The time dependencies of atmospheric turbulence are discussed in the next section.

1.4.2 TEMPORAL PROPERTIES OF ATMOSPHERIC TURBULENCE

Optical aberrations in the atmosphere are dynamic, evolving over time due to wind. Consequently AO systems must make corrections in real time, and determining a system's temporal requirements is critical. Greenwood[13] formulated the minimum **servo bandwidth** required for an AO correction system to maintain a diffraction limited image:

$$f_G = 2.31\lambda^{-6/5}\left[\sec\phi\int_0^L C_N^2(h)V_w^{5/3}(h)\mathrm{d}h\right]^{3/5} \qquad \textbf{1-7}$$

Where V_W is the atmospheric wind velocity profile as a function of altitude. A popular model for the profile was developed by Bufton[14], to fit data recorded near Mauna Kea:

$$V(h) = 5 + 30\exp\left\{-\left(\frac{h-9400}{4800}\right)^2\right\} \qquad \textbf{1-8}$$

The wind profile starts at 5 m/s at the ground, then rises to 35 m/s at a height of 9.4 km, before descending to 0 m/s at high altitude. Inserting Eqn. 1-8 into Eqn. 1-7, and using the index structure coefficient function from Eqn. 1-4, yields a **Greenwood Frequency** of 33 Hz for Subaru. In practice, sampling frequencies need to be 5-10 times the servo bandwidth for sufficient tracking. Accordingly, AO system sampling frequencies of 100-500 Hz are commonly used.

1.5 OVERVIEW OF ADAPTIVE OPTICS TECHNOLOGY

Adaptive optics systems are designed to constantly correct an astronomical target's wavefront while it is being observed. A set of specialized tools and techniques exist for

doing this. **Wavefront sensors** (WFSs) are used to measure the wavefront distortions, **deformable mirrors** (DMs) are used to correct it, and **real-time computers** (RTCs) are used for control.

1.5.1 SINGLE CONJUGATE AO SYSTEM ARCHITECTURE

The simplest functional AO method is known as **single-conjugate adaptive optics** (SCAO). In this configuration, a single WFS is used to measure the wavefront error, and a single DM is used to correct it. The WFS and DM are linked by a **real time computer** (RTC), containing the algorithms required to transform wavefront sensor measurements to DM commands. Light from a science target is usually too faint for the wavefront sensor to function properly, so a nearby bright **natural guide star** (NGS) is commonly used instead. A schematic diagram of an SCAO system is shown in Figure 1-7.
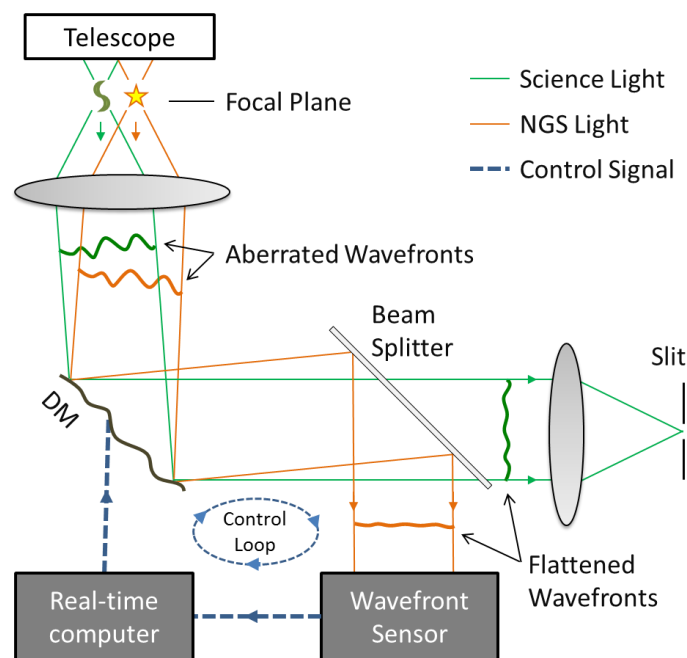
Figure 1-7: Schematic of a single Conjugate AO system. Science light and NGS light are collimated and reflect off a DM to flatten their wavefronts. A beam-splitter sends NGS light to a WFS, and science light to a spectrograph slit. A closed loop control loop between the WFS, DM and the NGS light is created using a real-time computer

Light from the science target and NGS, coming from the telescope, is first collimated, and then reflected off a DM. The DM shape needs to be half the opposite shape of the aberrated wavefront shape, to account for the doubling that occurs during a reflection.

The wavefronts of both the science target and the NGS will be flattened, but will retain residual errors due to system latency, DM fitting error, and inconsistencies between the NGS wavefront and the science wavefront. A beam splitter separates the different targets, sending NGS light to the WFS, and the science light to a recording device, shown in the figure as a spectrograph slit. As the science light is usually in the infrared, and the NGS light is usually visible, a dichroic beam-splitter is often used. A closed loop control system is formed between the DM and WFS using a real-time computer.

1.5.2 LIMITATIONS OF SINGLE CONJUGATE AO

Due to their slight angular separation, light from the science target and its guide star will travel slightly different paths through the atmosphere. This non-commonalty, called **anisoplanatism**[15], prevents the guide star's wavefront from being an exact match for the science target's wavefront. Figure 1-8 shows a simplified version of anisoplanatism, sampled at three different altitudes.
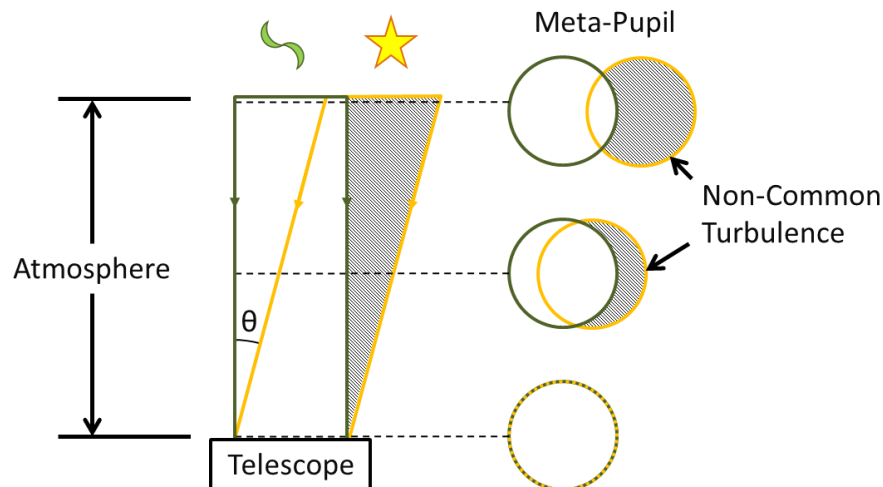
Figure 1-8: Anisoplanatism. The light from the science target (green) travels through a slightly different path than the light from the guide star (yellow), due to their angular separation. The hatched regions represent the non-commonality between the two paths, which is larger at higher altitudes.

The wavefront difference between the two sources increases with their angular separation. Subsequently, to allow proper correction, the science target must be close enough to its guide star so that their wavefronts can be approximated as the same. This region, called the **isoplanatic patch**, is illustrated in Figure 1-9.
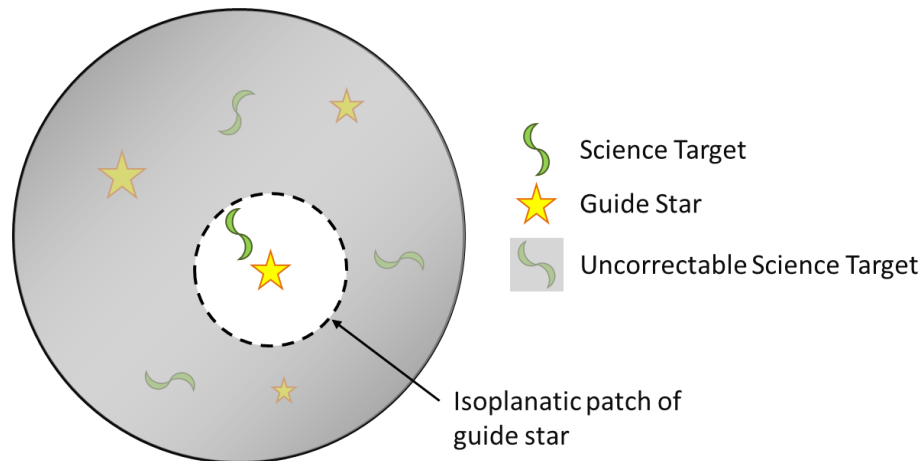
Figure 1-9: Typical SCAO field. Science targets must be within the isoplanatic patch of a guide star in order to be observable.

Science targets without a nearby guide star within their isoplanatic patch cannot be corrected with SCAO because of anisoplanatism. Consequently, a significant portion of potential science targets cannot be adequately observed. This problem was solved through the invention of artificial stars, called **laser guide stars** (LGSs), created by pointing a tuned laser beam into the sky, exciting ions in the atmosphere's sodium layer, occurring between 90-100km in altitude[16]. By using an LGS, a reference star can be placed next to any science object, making it available for correction.

Almost every VLT has an SCAO system similar to the one described above, and they are extremely valuable astronomical tools. However, these technologies are only capable of correcting a single science target at a time. Anything outside the guide star's isoplanatic patch is not correctable and discarded, requiring its own observation time later. When observing with an ELT, it will not be reasonable to only correct a small portion of the field, when the entire field may be full of potentially viable science objects. Observation time is too valuable, and in such high demand, that a significant effort must be made to correct the entire field. Multi-Object AO, along with Multi-Conjugate AO[17], and Ground-Layer AO[18], are new system architectures designed to solve this problem, and assist the ELTs with reaching their full potential.

1.6 OVERVIEW OF MOAO TECHNOLOGY

MOAO is one solution to SCAO's lack of scalability. This relatively new concept can be thought of as multiple SCAO systems working in parallel, where each system is responsible for correcting the wavefront of its own science target. A schematic of a generic MOAO system is shown in Figure 1-10. Only two wavefront sensors and two science arms are displayed, but any number of each could be used.
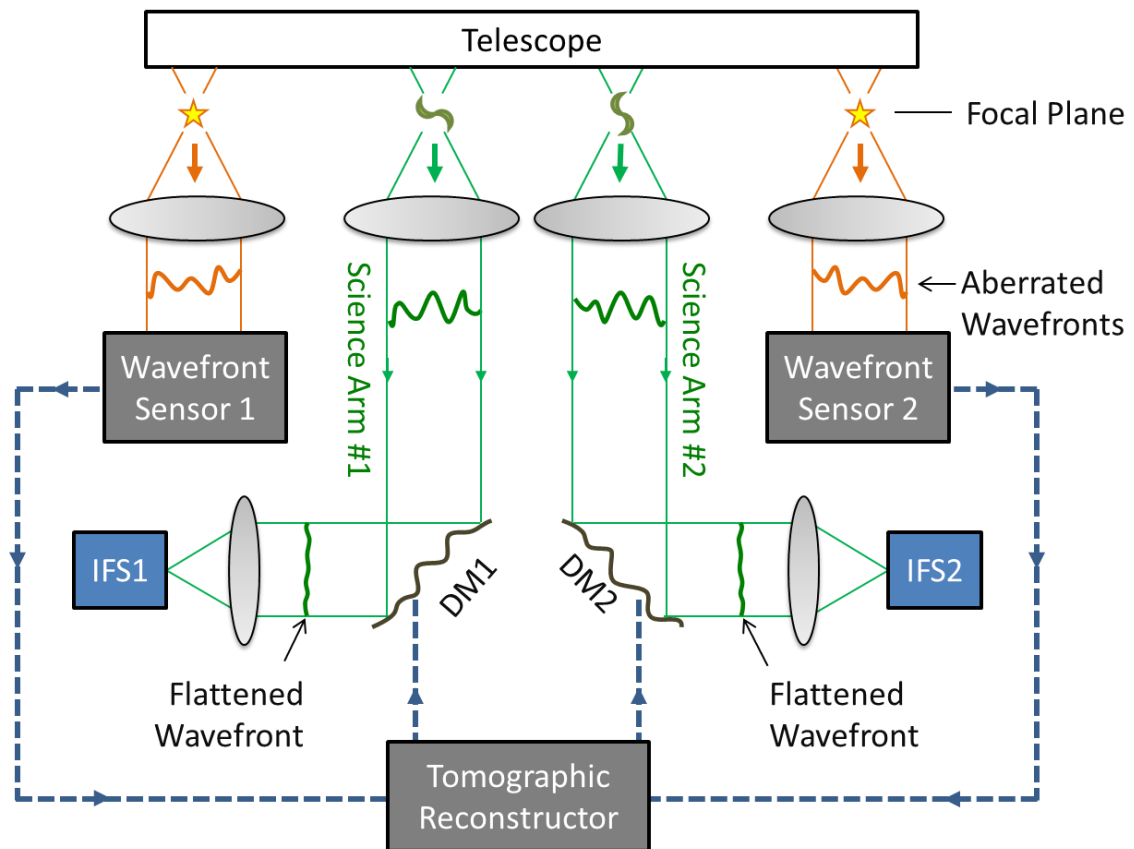
Figure 1-10: MOAO system architecture. Wavefront measurements from multiple WFSs are combined in a tomographic reconstructor to formulate the wavefronts of multiple science targets. Each science target has its own DM and IFS. Using this technique, a large number of science targets can be corrected

The main difference between MOAO and SCAO is how the science targets' wavefronts are measured. It would be unrealistic for each science target to have a nearby NGS, and impractical to provide each one with an LGS. Consequently, in MOAO, several NGSs located in arbitrary positions, and several LGSs spread throughout the field are utilized. The wavefront measurements of all these guide stars are combined in a tomographic

algorithm used to reconstruct the entire volume of turbulence above the telescope[19]. Each science target is given its own **science arm** containing a DM whose shape is determined by projecting the reconstructed volume of turbulence to its field location[20]. After reflecting off a DM, light from each science arm enters its own specialized instrument, known as an **integral field spectrograph** (IFS).

   In an MOAO system, light from multiple sources must be separated from the field, and sent to the correct optical subsystems. In SCAO, a simple dichroic beam-splitter was used, but this is no longer an option. Alternatively, MOAO systems use opto-mechanical devices called **pick-off arms** to move in the telescope's focal plane, and extract only the light needed for a specific subsystem. A pick-off arm removes its own small field of view from the telescope's overall field of view, which is now referred to as the **field of regard** (FoR). An example of pick-off arms in a telescope's FoR is shown in Figure 1-11. A pick-off arm's FoV needs to be mobile, allowing it to select any specific portion of the FoR.
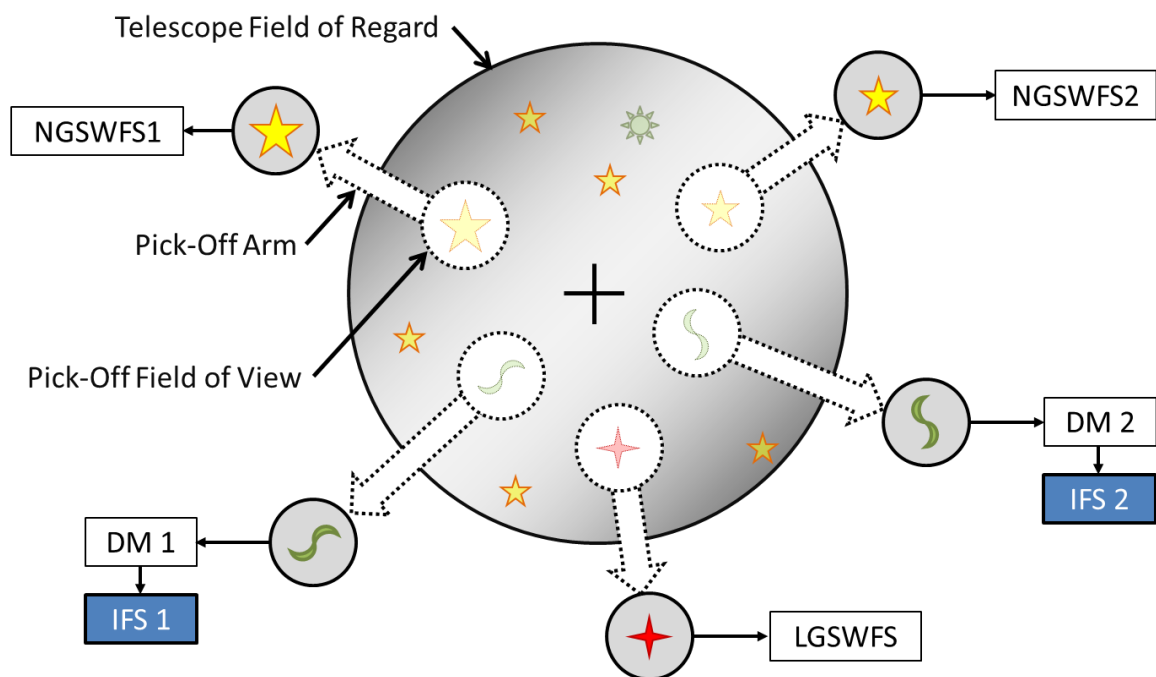
Figure 1-11: Pick-off arms are used to extract specific regions of light from the telescope's focal plane. Guide star light is sent to WFSs and science light is sent to DMs and on to IFSs. Pick-off arm's need to be placed at, or very near to, the telescope's focal plane.

Conceptual planning has already started on the MOAO instruments for the ELTs. The proposed MOAO instrument for TMT, called the IfraRed Multi-Object Spectrograph (IRMOS) is being designed for 6 NGS, 8 LGS and 20 IFUs[21]. The equivalent on the E-ELT is called EAGLE, and will have 5 NGS, 6 LGS and 10 IFUs[22]. A preliminary CAD model for EAGLE is shown in Figure 1-12.
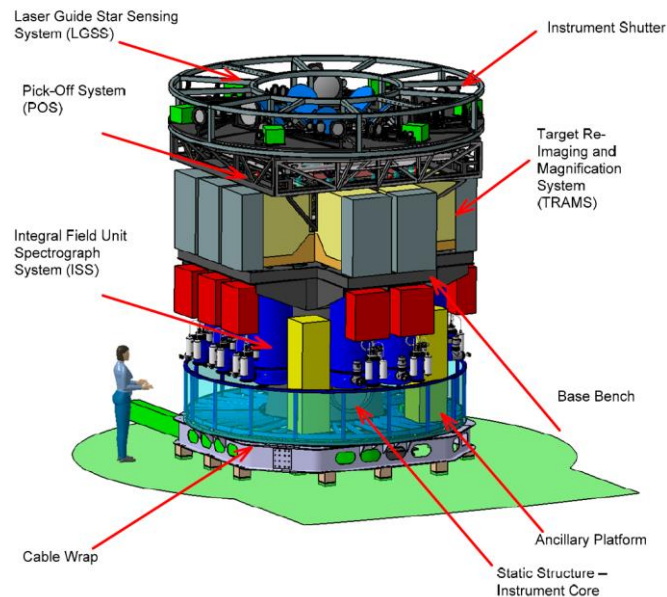
Figure 1-12: Conceptual design of EAGLE, the MOAO instrument for the E-ELT[22].

1.7 MOAO DEMONSTRATORS

MOAO does solve SCAO's lack of scalability; however it comes with its own unique set of challenges, most notably that the optical correction must be done in open-loop. As the light from the guide-stars is never reflected off a DM, no knowledge of the current DM shapes can be optically obtained. Open loop control poses substantial risks to any system and, accordingly, MOAO must be successfully demonstrated before facility instrument can be confidently designed for an ELT.

An initial study was performed in 2003, called FALCON[23], which presented the MOAO concept and paved the way for future work. The first hurdle, demonstrating open loop control was successfully demonstrated using the Victoria Open Loop Testbed (VOLT)[24] in May 2008. Additionally, the Visible Light Laser Guidestar Experiments (ViLLaGEs)[25] system carried out both NGS and LGS open loop control tests on the

Nickel 1-meter telescope at the Lick Observatory. Both VOLT and ViLLaGEs, while successful, performed relatively poorly at low temporal frequencies, indicating that misalignments and calibration errors may limit performance. Based on these results, a second generation of MOAO demonstrators was planned. Canary was the first of these systems, and is considered to be a path-finding device for EAGLE[26]. Operating on the 3.6m William Herschel Telescope, Canary's primary objectives are to perform multi guide star tomographic wavefront reconstruction, demonstrate open loop AO correction on sky, and develop more sophisticated alignment and calibration techniques. Canary has three mobile NGS pick-off arms and one correction path located on axis. Canary does not attempt scientific observations, and is used as a dedicated engineering device.

1.8 RAVEN: AN MOAO PATH FINDING INSTRUMENT

Raven will expand on the work of Canary and the other MOAO demonstrators. It will be the first MOAO instrument on an 8m class telescope, and the first to perform science. Raven's high level requirements are shown in Table 1-1.

Table 1-1: High level requirements for Raven

Parameter	Requirement
# of science channels	2
# of WFSs	3 NGSs + 1 on-axis LGS
Field of Regard	3.5' (112mm in focal plane)
Science FoV	4" per channel (2.1mm in focal plane)
Ensquared Energy	>30% in 0.140" slit
Throughput	>32% in H band

A simplified asterism for Raven is shown in Figure 1-13. Three outer NGS and one centrally located LGS are used for wavefront sensing. Two science targets, near the center, will be corrected. The guide stars are each picked-off and sent to WFSs. The science targets are picked-off, corrected by DMs, and placed side-by-side on the IRCS slit.
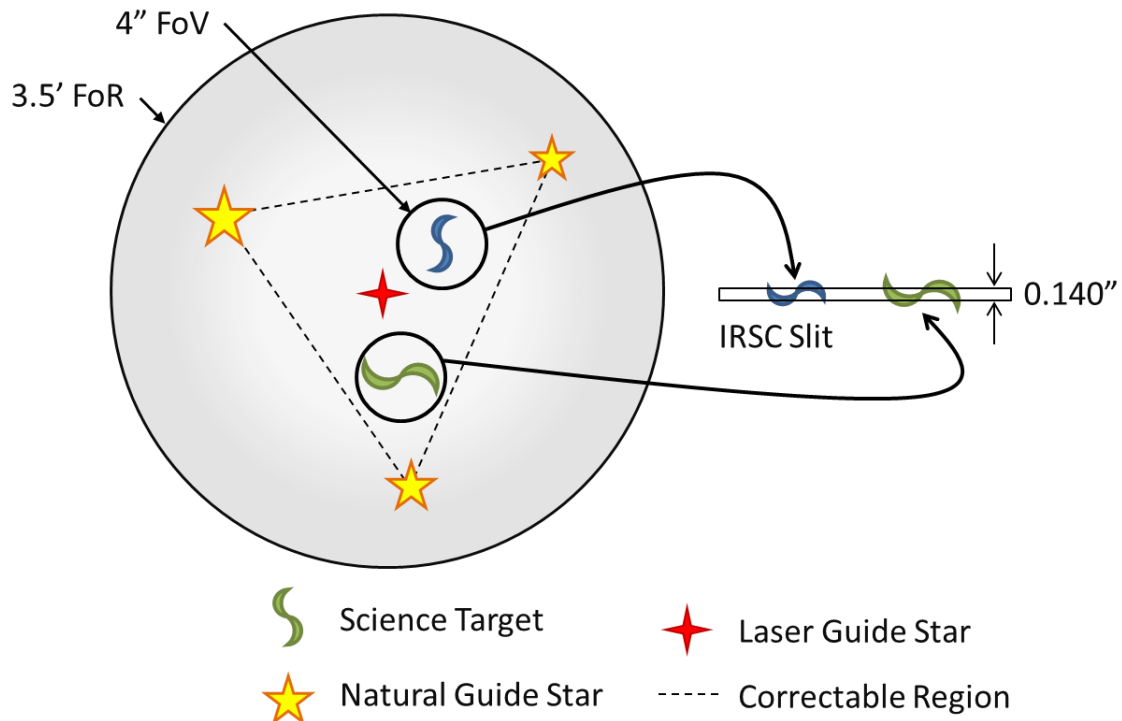
Figure 1-13: Potential Raven asterism. The 3 NGSs encircle 2 science targets. A centrally located LGS is available.

Unlike the proposed MOAO systems for the ELTs, where each science target gets its own IFS, Raven will feed both of its science targets, side-by-side, into the IRCS slit. Raven requires mobile science pick-off arms and mobile guide star pick-off arms. In subsequent sections, it will be shown that Raven's tip/tilt compensation system relies heavily on the mobility of its pick-off arms. The LGS will always be centrally located so it does not require a mobile pick-off arm. A discussion of telescopes, spectrographs, atmospheric turbulence, MOAO, and the Raven demonstrator has been presented. The central topic of this thesis, Raven's tip/tilt compensation system, can now be discussed.

1.9 TIP/TILT CORRECTION METHODS

Tip/tilt errors globally shifts the output image in the telescope's focal plane, however it does not degrade instantaneous resolution[e]. If tip/tilt is not accounted for and compensated, it will be passed through the system causing the output image to move off

---

[e] If tip/tilt errors are present during an extended exposure time the image's motion will blur the resultant long exposure point-spread-function

of the spectrograph slit. Figure 1-14 depicts a simplified MOAO science arm, where a science target is collimated using a lens, reflected off a deformable mirror, and then refocused onto the slit of an IFS. The effects of shifting the science target in the input focal plane, and techniques for compensating the shift are also illustrated.
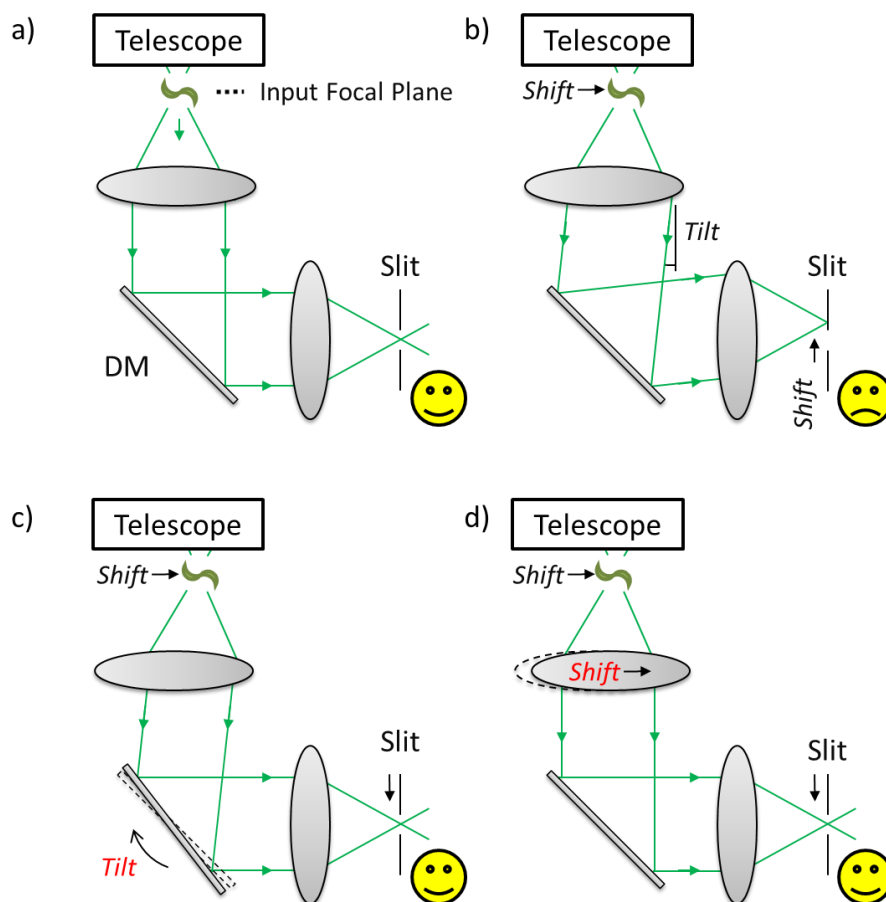
Figure 1-14: Tip/tilt compensation on a science arm: a) A science target in its nominal position, light passes through the arm and enters the slit b) Shifting the location of the science target in the focal plane results in a tilt at the DM and an equal shift at the output focus, causing the light to shift off the slit. Correcting tip/tilt can be done by either tilting the DM (c) or by shifting the field lens to match the target motion (d)

Two different methods are available for centering the focus back into the slit: the DM can be tilted (Figure 1-14c), and the initial lens can be shifted (Figure 1-14d). Usually AO systems exclusively utilize tilting to correct these errors. However, on MOAO systems, the lenses are built into the pick-offs, so they are inherently mobile and could be used for correcting tip/tilt errors.

High-frequency tip/tilt errors, referred to as **jitter**, is caused by atmospheric turbulence, windshake[f], and mechanical vibrations. Low-frequency tip/tilt errors, referred to as **drift**, is caused by field rotation, differential atmospheric refraction and telescope tracking error.

1.10 ATMOSPHERIC TIP-TILT

Atmospheric turbulence imparts a tip/tilt component to the wavefront. Determining the potential spatial range of atmospheric tip/tilt, and its frequency spectrum is the objective of this section. The results will be used to aid the optomechanical design of Raven's tip/tilt compensation system.

1.10.1 SPATIAL CHARACTERISTICS OF ATMOSPHERIC TIP/TILT

The required angular stroke of Raven's tip/tilt compensation system is the first design parameter to determine. First, the spatial characteristics of the overall wavefront phase error will be formulated, and then the tip/tilt component will be extracted from the result. Noll[27] determined the total spatial wavefront phase variance from atmospheric turbulence to be:

$$\sigma_{Total}^2 = 1.032(D/r_0)^{5/3}$$

1-9

The tip/tilt component of the overall wavefront error needs to be extracted. The total wavefront error can be decomposed into a sum of its different spatial modes, called **Zernike Modes**, similar to how complex sounds can be decomposed into individual notes. Zernike Modes represent an infinite set of circular, orthogonal shapes of increasing radial and angular orders. A summary of the first several Zernike modes is illustrated in Figure 1-15.

---

[f] Windshake is vibration induced by a telescope's interaction with the wind.
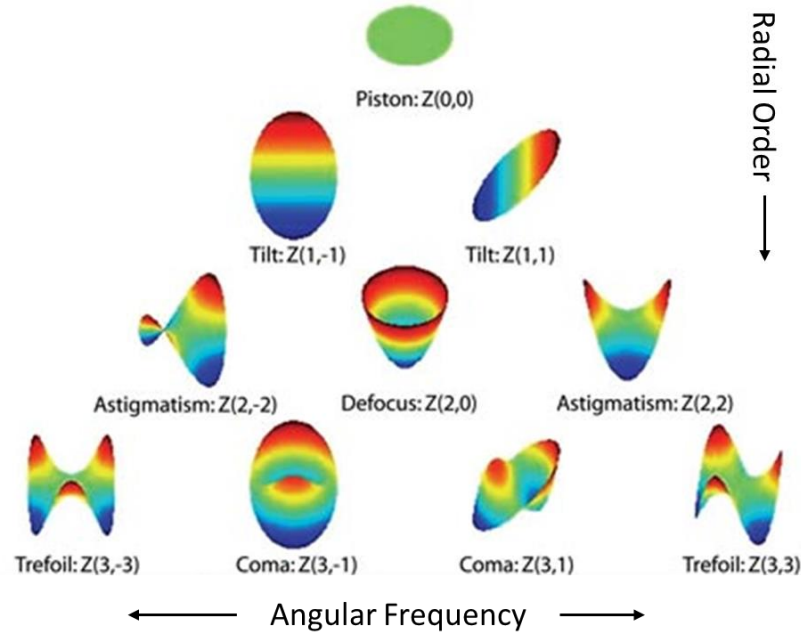
Figure 1-15: Wavefront shapes of the first several Zernike Modes. Piston has no effect from an observing perspective. Tip and tilt are next, and are simply tilted flat wavefronts. The shapes become more complex as their radial and angular orders increase.

The first few mode shapes: tip, tilt, defocus, astigmatism, and coma, are quite common in optical aberration theory. The "piston" shape is a global shift of the entire wavefront, and has no effect on the output image. The total wavefront error can be written as the sum of the variance of all its Zernike modes, extending indefinitely.

$$\sigma^2_{Total} = \sigma^2_{Tip} + \sigma^2_{Tilt} + \sigma^2_{Foc} + \sigma^2_{Astig} + \cdots \qquad \textbf{1-10}$$

The wavefront variance of tip and tilt was determined to be:

$$\sigma^2{}_{Tip} = \sigma^2{}_{Tilt} = 0.455(D/r_0)^{5/3} \qquad \textbf{1-11}$$

This result indicated the majority of wavefront error is contained in the tip/tilt modes. It can be subsequently used to determine the required stroke of a tip/tilt compensation system. For practical reasons, Eqn. 1-11 needs to first be converted from phase space to a real angle. The conversion factor from Zernike tip/tilt to the real pointing angle of the incoming beam is $(4\lambda/2\pi D)^2$, according to Noll. The $\lambda/2\pi D$ term simply converts

phase to angle, and the multiplication by 4 is to reverse a normalization term gained during the Zernike decomposition. Finally, we arrive at the equation for the RMS tilt angle, α, caused by the atmosphere:

$$\alpha_{RMS} = 0.427 \frac{\lambda}{D} \left(\frac{D}{r_0} \right)^{5/6} = 1.74 D^{-1/6} \left[\sec \phi \int C_N^2(h) dh \right]^{1/2} \qquad \textbf{1-12}$$

The alternate form Eq. 1-12 is shown to clarify that α_{RMS} is not wavelength dependent. Additionally, the $D^{-1/6}$ term implies that as telescopes continue grow in diameter the amount of rms tip/tilt error will slowly decrease. For the same atmosphere a 30m telescope would experience about 80% of the tip/tilt of an 8m telescope. Importantly, Eqn. 1-12 provides a method for specifying the required angular stroke of an atmospheric tip-tilt compensation system. To compensate ~99% of the atmospheric tip-tilt errors, a minimum stroke of 2.5 times the standard deviation is required:

$$\alpha_{T/T\ Stroke} = 1.1 \frac{\lambda}{D_{TTM}} \left(\frac{D_{Tel}}{r_0} \right)^{5/6} \qquad \textbf{1-13}$$

Where D_{TTM} is the diameter of the tip/tilt mirror used on the system. Its introduction is due to the magnification ratio between the telescope diameter and tip/tilt mirror diameter. Using a 25mm diameter tip-tilt mirror, an 8m telescope, and an r_0 of 10cm, a stroke of 0.035° is required to compensate atmospheric tip-tilt for Raven. The required tip/tilt servo-bandwidth is discussed in the following section.

1.10.2 TEMPORAL CHARACTERISTICS OF ATMOSPHERIC TIP/TILT

Tyler[28] formulated the tip-tilt correction servo bandwidth required for diffraction limited observation, independent of any other wavefront error modes. His relation is shown in Eqn. 1-14.

$$f_{T/T} = 0.368 D^{-1/6} \lambda_T^{-1} \left[\sec(\gamma) \int C_N^2(h)\, V_w^2(h) dh \right]^{1/2} \qquad \textbf{1-14}$$

Where λ_T is the tracking wavelength, typically 700nm[29] for commercial CCD sensors. A servo-bandwidth of 3Hz was calculated for an 8m telescope using the Mauna Kea data, closely agreeing with the findings of Olivier[10]. This result indicates the tip/tilt compensation control frequency needs to be ~10% of that required to compensate higher order modes. Consequently, a wider variety of mechanical actuators can be used for tip/tilt compensation.

1.11 NON-ATMOSPHERIC SOURCES OF TIP-TILT

Many potential tip/tilt error sources exist in addition to atmospheric turbulence. These include: field rotation, differential atmospheric refraction (DAR) and telescope tracking error. These alternative tip/tilt error sources are slower and more predictable than atmospheric tip/tilt, but have much larger amplitudes. Each error source will be discussed in detail over the next few subsections.

1.11.1 FIELD ROTATION

During an observation, the night sky revolves around Earth's rotation axis. Telescopes must constantly adjust their pointing angle to match this motion to keep their observed image centered. Subaru's altazimuthal mount (see Figure 1-1) is well equipped to track this kind of motion. However, as it tracks, the field rotates. The required equations for the field rotation angle (FR) are shown below[30]. It is the sum of the target's parallactic angle (q), and the elevation angle of the telescope (El). Both these terms are functions of the observed target's declination (dec), the latitude of the telescope (lat) and the time (hour angle: ha).

$$FR = q + El \qquad \textbf{1-15}$$

$$q = \tan^{-1}\left(\frac{\sin(ha)}{\tan(lat)\cos(dec) - \sin(dec)\cos(ha)}\right) \qquad \textbf{1-16}$$

$$EL = \sin^{-1}(\sin(lat)\sin(dec) + \cos(lat)\cos(dec)\cos(ha)) \qquad \textbf{1-17}$$

The zenith angle (Z) is the compliment of the largest elevation angle, occurring at 0 hour angle. At zenith, the field rotation speeds reach their maximum. Graphs of the field

rotation angle, and rotation speed, as a function of hour angle are shown in Figure 1-16 for a variety of Zenith angles.
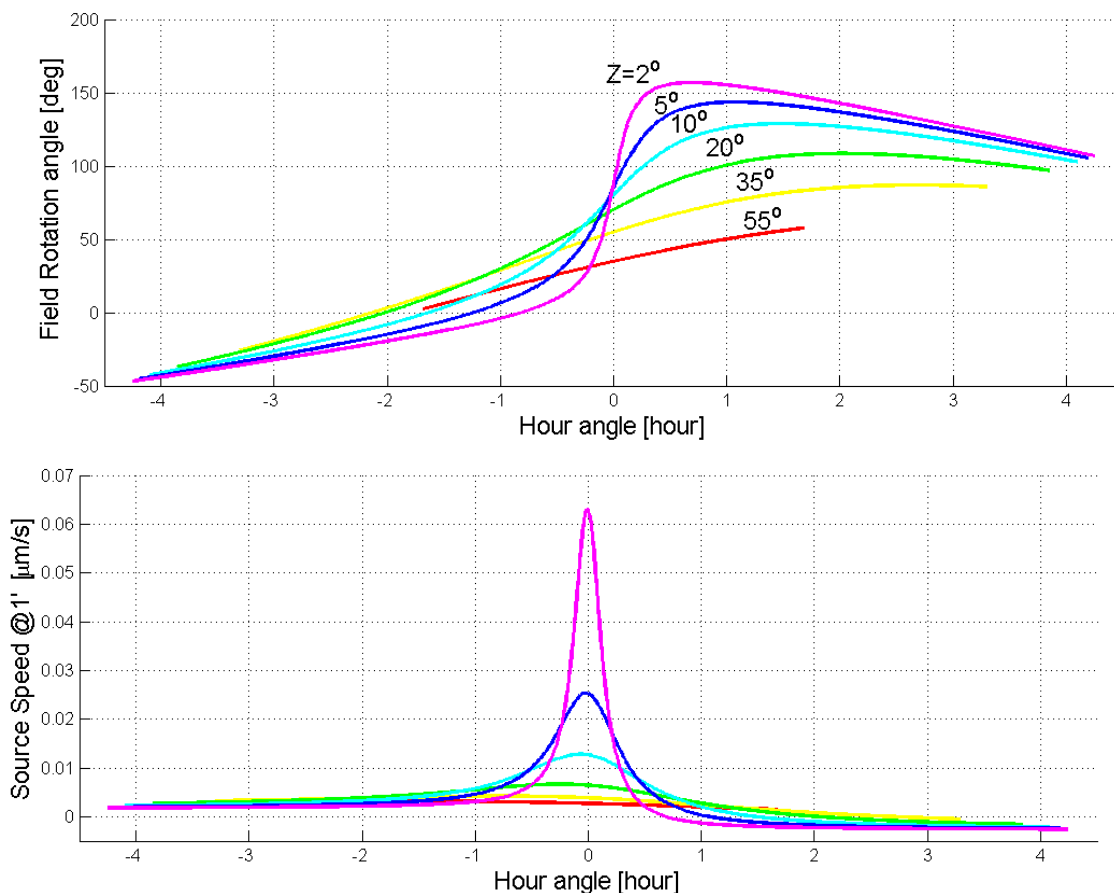
Figure 1-16: Field rotation as a function of hour angle and zenith angle. (a) field rotation angle, (b) field rotation speed, for a target 1' from the field center. A maximum source speed of 64 μm/s is measured for a target with a zenith angle of 2°.

Subaru will not observe targets with zenith angles of less than 2°. Additionally AO correction isn't as effective when observing at zenith angles larger than 60° due to the increased amount of turbulence the light has to travel through. These graphs show that during a three hour observation, a field may rotate through 180°, and a target may travel at a maximum speed of 64μm/s in the focal plane.

Subaru is outfitted with an image derotator near its output focus to compensate field rotation for its AO systems and science instruments. Unfortunately, the derotator requires a substantial amount of optical path length (393mm), moving Subaru's output focal plane

from the Nasmyth Platform to almost inside the telescope's structure, where Raven cannot access it. Consequently, Subaru's derotator will not be used, and Raven must compensate for field rotation internally[g]. Raven's pick-off arms are used to track field rotation because they already possess a large stroke, and no additional mechanical design work was required. Figure 1-17 shows an example of pick-off arms being used to track field rotation.
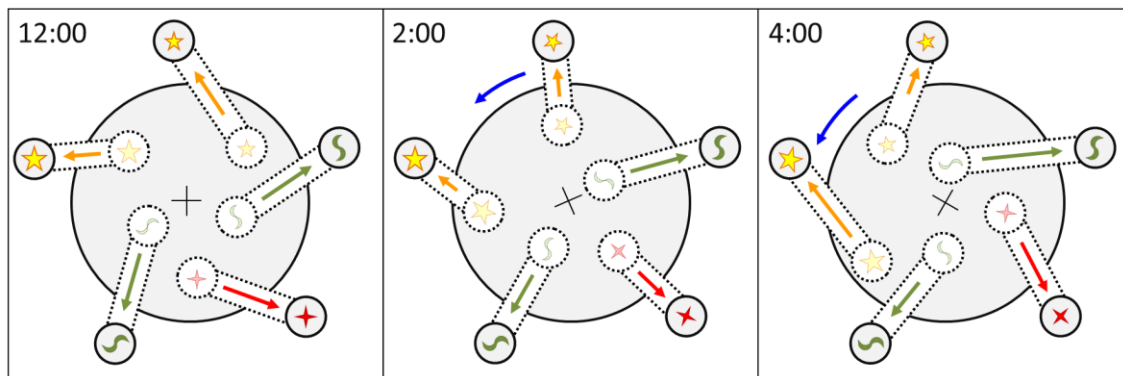
Figure 1-17: Field rotation tracking using pick-off arms. As the targets move, the pick-off arms move accordingly, and continually pick them off

Future MOAO systems like EAGLE and IRMOS may be mounted on large rotating platforms to track the field rotation. Raven's method of using pick-off arms is a unique concept, implemented out of necessity.

1.11.2 DIFFERENTIAL ATMOSPHERIC REFRACTION

The refractive index of air is not only temperature dependent but, like a prism, is also wavelength dependent[31]. Longer wavelengths entering the atmosphere will refract more substantially than shorter wavelengths. This effect, called **differential atmospheric refraction** (DAR), will blur multi-wavelength images if left uncorrected. Figure 1-18 illustrates this effect.

---

[g] AO188 also does not use the Subaru image de-rotator, and instead uses a smaller internal derotator and a set of reimaging optics to access the focal plane
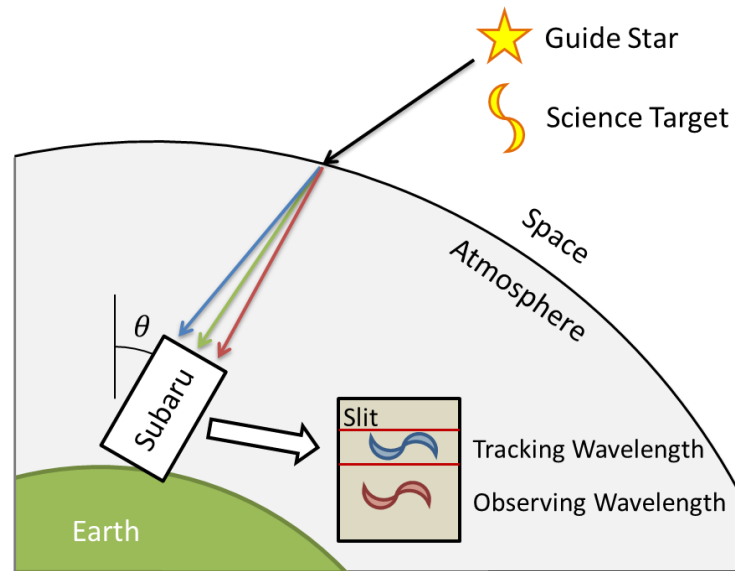
Figure 1-18: Differential atmospheric refraction. A telescope at zenith angle θ will observe a blurred image of the science object (shown in yellow). The wavelength dependence of air refractive index bends the different wavelength components of the object at different angles, creating a chromatically blurred image

DAR is relevant to a tip/tilt compensation system because of the difference between the tracking wavelength (700nm) and the science target wavelengths (1000 to 4000nm). Without compensation, an AO system will intentionally place the portion of the science light spectrum corresponding to the wavefront measurements on the slit[32]. The angular separation between the observing wavelength and tracking wavelength is a function of zenith angle, air pressure, humidity and the composition of air. The following chart shows the amount of DAR Raven can expect during an observation over a range of observing wavelengths.
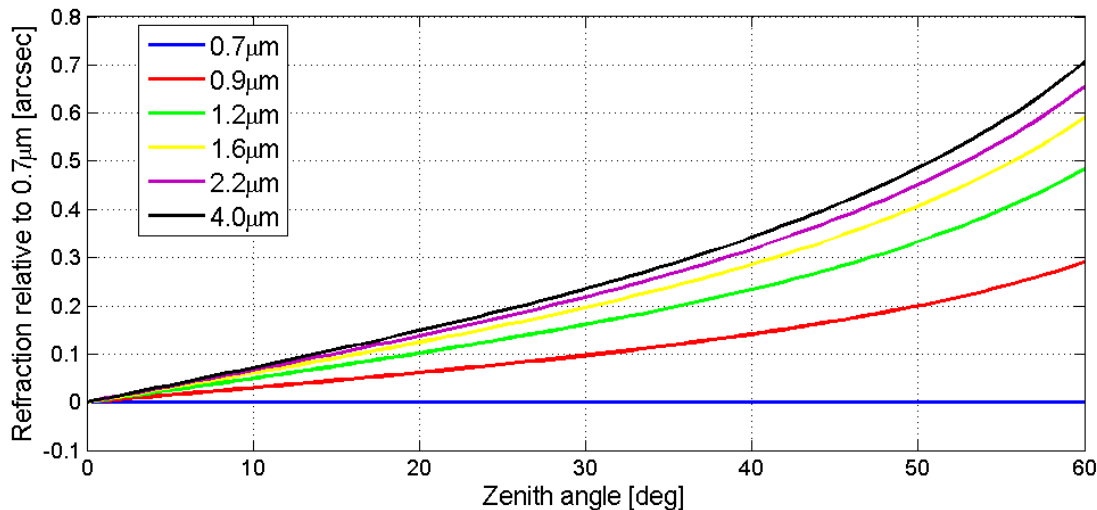
Figure 1-19: Amount of differential atmospheric refraction for different zenith angles and observing wavelengths. The data is compared to a 700nm reference wavelength. A maximum angular separation of 0.7" is expected, but 0.4" will be used as a more typical maximum

In the most extreme case, this figure shows a maximum angular separation of 0.7" on sky, which is 5 times the IRCS slit width. **Atmospheric Dispersion Correctors** (ADCs) are commonly used to reverse the effect of DAR. These devices were deemed unnecessary for Raven, where the required positional shift between the NGS pick-off arms and science pick-off arms can be readily computed and implemented during an observation.

1.11.3 TELESCOPE TRACKING ERROR

As mentioned earlier, Subaru needs to constantly adjust its pointing direction to track a target's motion caused by the Earth's rotation. Over time, a tracking error can develop, causing the image to slowly drift. The tracking error is caused by a variety of factors including inconsistencies in the altazimuthal mount rails[33]. Subaru has a dedicated device, called the **autoguider**, for improving tracking accuracy. The autoguider picks-off a guide star on the periphery of the field, and attempts to keep it stationary by adjusting the pointing direction of the telescope in closed loop. The autoguider is designed to be used with Subaru's de-rotator, so Raven will also not be able to use it. Additionally, Raven is not permitted to directly communicate with the telescope's pointing system. The

tracking error must therefore be internally handled by Raven's pick-off arms. Table 1-2 shows the expected tracking error of Subaru over different time intervals[34].

Table 1-2: Subaru tracking error after different time intervals

Blind pointing accuracy	≤ 1" rms (0.53 mm in focal plane)
Motion in 1 minute	≤ 0.1" (0.053 mm in focal plane)
Motion in 10 minutes	≤ 0.2" (0.106 mm in focal plane)
Motion in 30 minutes	≤ 0.6" (0.106 mm in focal plane)

On Subaru, AO188 compensates tip/tilt errors with a dedicated tip/tilt platform mounted under its DM. Figure 1-20 shows the platform's angular position during an observation with the autoguider enabled (blue line) and with the autoguider disabled (red line).
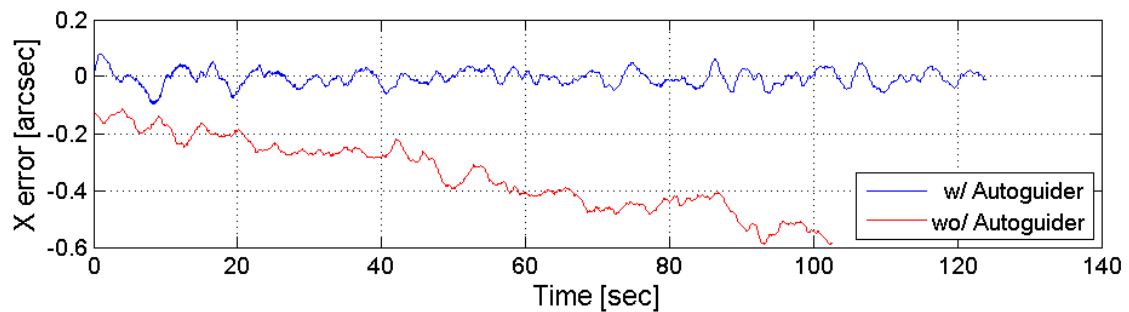
Figure 1-20: Subaru pointing error with the autoguider enabled (blue) and disabled (red).

It can be seen that when the autoguider is disabled, a ~0.4" tracking error occurs over a 2 minute period, which for unknown reasons, develops substantially faster than specified by Table 1-2.

1.12 THESIS OBJECTIVES

Raven's tip/tilt compensation system is the subject of this thesis. No previous MOAO system has been required to do science, or feed a spectrograph. Consequently, robust tip/tilt compensation is now important, and must be considered in detail. The main chapters of this thesis are arranged in the following order. Starting with Raven's optomechanical design, and finishing with performance results.

Chapter 2: Description of the Experimental Apparatus

An overview of Raven's optical and mechanical components is presented, with specific emphasis on the subsystems capable of measuring or compensating tip/tilt.

Chapter 3: Sensor and Actuator Tuning and Characterization

The tuning of Raven's primary optical sensors: the WFSs and science camera, and Raven's primary actuators: the pick-off arms, tip/tilt platforms, and deformable mirrors, is discussed. After tuning, the performance of each sensor and actuator is characterized

Chapter 4: Tip/Tilt Compensation Control System Design and Calibration

The design of Raven's control system architecture is discussed. The spatial transforms, geometric transforms, and temporal filters required for proper AO correction are explained and designed using both Raven's baseline specifications and measured calibration data. Both the fast control system (RTC) and slow control system (AOS) are discussed.

Chapter 5: Results

Results from simulated observations using Raven are presented, including its baseline AO performance, and the performance of different portions of the tip/tilt compensation system

Chapter 6: Conclusion and Future Work

The key results are re-iterated, and potential improvements to Raven's tip/tilt compensation system are discussed.

2 DESCRIPTION OF THE EXPERIMENTAL APPARATUS

This chapter gives a detailed description of Raven's optical and mechanical systems, focusing on the sensors and actuators relevant to the tip/tilt compensation system. The chapter is ordered in the same way light takes going through Raven, starting at the telescope and finishing at IRCS. The optical design was created by Lardiére[35].

2.1 SYSTEM OVERVIEW

A block diagram of Raven's main optical and mechanical components is shown in Figure 2-1. The LGS WFS system is not shown, as it is not relevant to the tip/tilt

compensation system[h]. Blue lines represent white light, green lines represent visible light, and red lines represent infrared light.
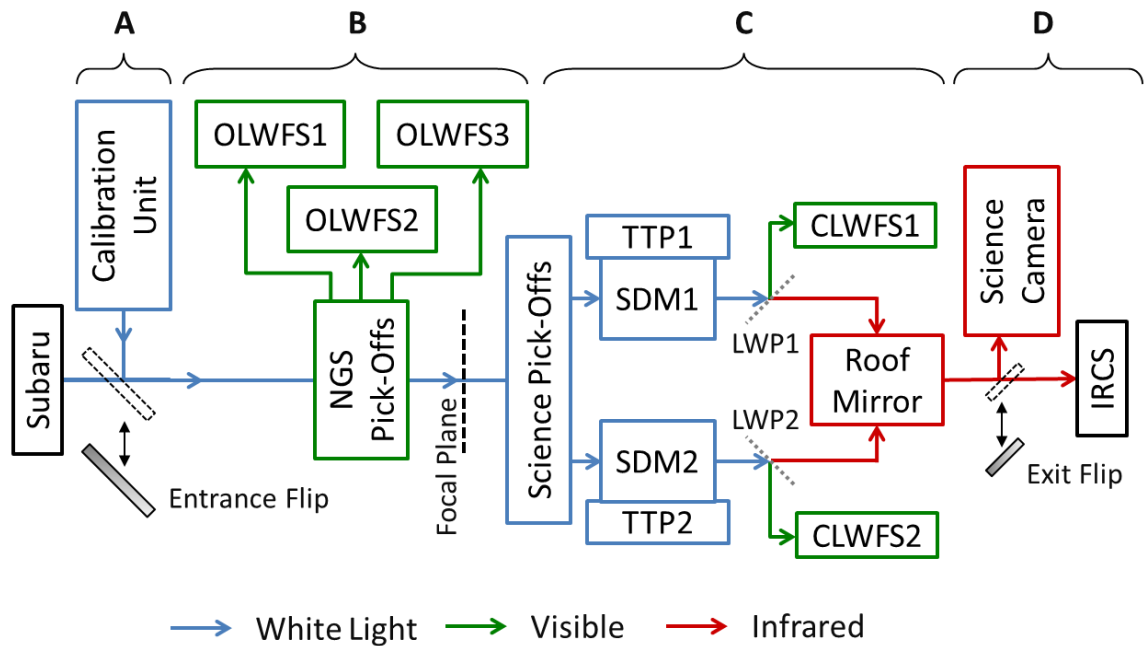
Figure 2-1: Main optical elements of Raven. White light is shown as blue, visible light as green, and infrared light as red. (A) Calibration Unit, (B) NGS pick-off arms, (C) Science path, (D) Science Camera and IRCS

A. **Calibration Unit**: A laboratory subsystem that can recreate the optical aspects of an observation, including: light sources, turbulence and Subaru's optics[36,37]. Additionally it provides calibration and alignment tools. An automated **entrance flip mirror** can be moved in and out of the beam to select whether light from Subaru or light from the CU enters Raven.

B. **Natural Guide Star (NGS) Pick-Off Arms**: Three NGSs are extracted using pick-off arms, 15mm before Subaru's focal plane. The NGS light is then directed to **open-loop wavefront sensors** (OLWFSs) for turbulence sampling. Raven's NGS pick-off arms are each mounted on a motorized x-y translation platform to provide mobility.

---

[h] Tip/tilt cannot be measured by an LGS due to its double path through the atmosphere. The amount of tip/tilt acquired on the way up when the beam is thin, is cancelled by the same amount on the way down when the beam is expanding. Tip/tilt is the only wavefront mode an LGS cannot effectively measure

C. **Science Paths**: Raven's two science paths are located 20mm behind Subaru's focal plane. Each arm includes a pick-off arm, a **science deformable mirror** (SDM) for wavefront correction, a **tip/tilt platform** (TTP), a **low-wave-pass** filter to separate visible and infrared light, and a **Closed loop wavefront sensor** (CLWFS) for performing calibration and measuring performance. A roof mirror combines the science light from both paths and sends it towards IRCS.

D. **IRCS and Science Camera**: Light from both science targets will enter IRCS's slit side-by-side and their spectra will be recorded simultaneously. During both the laboratory phase, and daytime operation, an infrared science camera is used in place of IRCS to measure Raven's performance.

2.2 CALIBRATION UNIT

The CU has two primary functions: providing the tools to calibrate Raven's different optomechanical subsystems, and accurately simulating observations. A simplified schematic diagram for the CU is shown in Figure 2-2, and its mechanical design is shown in Figure 2-3. The underlined labels explain what portion of an observation each subsystem simulates.
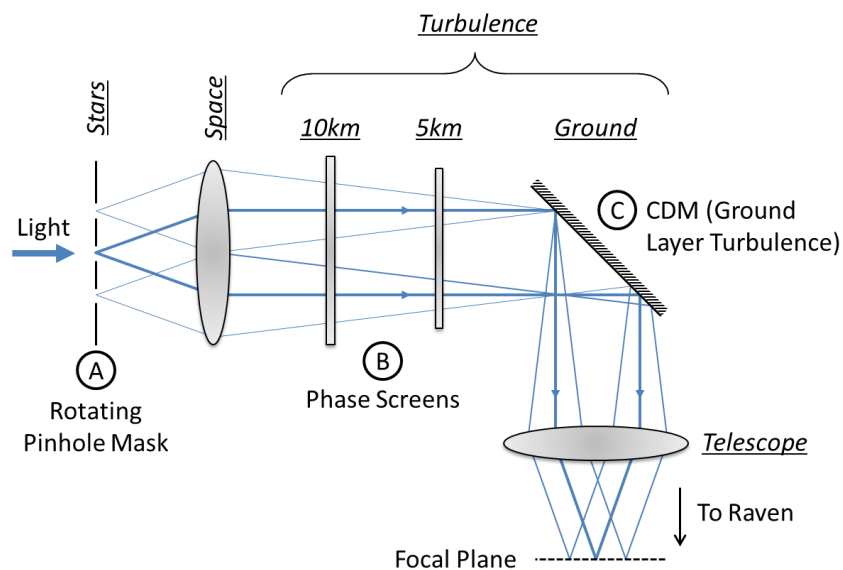
Figure 2-2: Optical Design of the Calibration Unit. An array of point sources are collimated, sent through phase screens, reflected off the CDM and refocused.
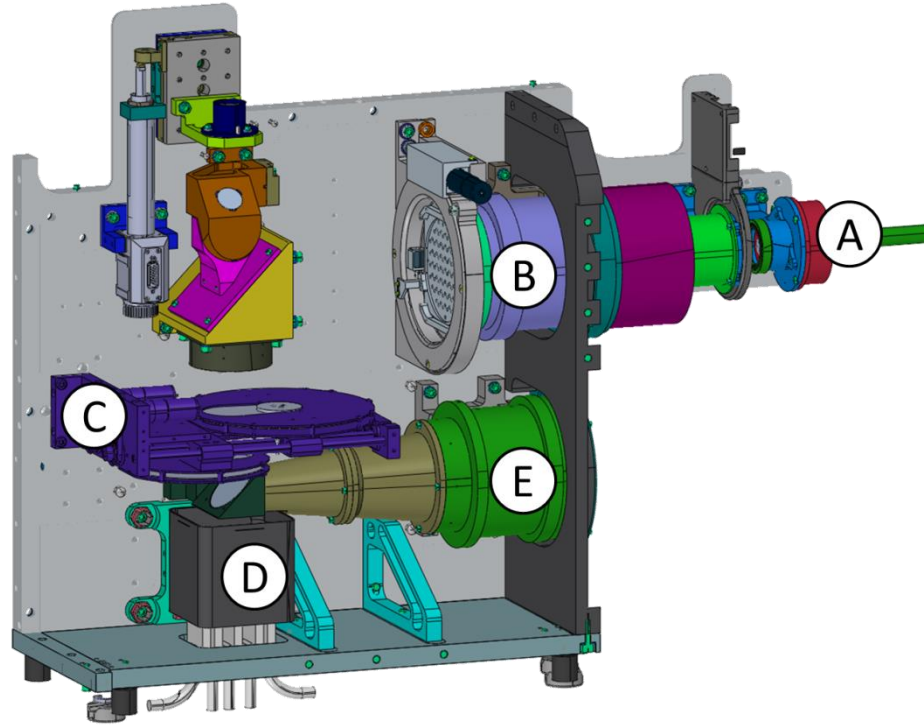
Figure 2-3: CAD model of the calibration unit. Many components have been hidden for clarity. White light from a lamp enters the CU from a fiber-bundle at (a). A pinhole mask creates an array of simulated stars at (B). This light passes though phase screens at (C) which simulate high altitude turbulence. A deformable mirror at (D) simulates ground layer turbulence. Lenses at (E) then reshape the light to have the same focal length as light coming from Subaru

Rotating pinhole mask: The "stars" of the CU are created by shining light from a halogen lamp (Oriel M66881) through a custom pinhole mask. Two sizes of pinhole are machined into the mask: an 8x8 diffraction-limited set used during simulated observations with turbulence, and a 7x7 seeing-limited set used during turbulent-free calibration. A selector plate is used to expose either the diffraction limited pinholes or the seeing limited pinholes to the lamp's light. The light's intensity can be changed using a motorized filter wheel (Thorlabs FW102C) located between the lamp and the pinhole mask. Light from a pinhole will subsequently be referred to as a "source". Field rotation is simulated by rotating the pinhole mask using a motorized rotation stage, with a travel of ±90°. The dimensions of the pinhole mask, and its numbering convention is shown in Figure 2-4. Pinhole 19 of the seeing-limited set is located at the center of the field, and will become useful during the calibration procedures described in subsequent chapters.

Pinhole Mask "Seeing Limited" "Diffraction Limited"
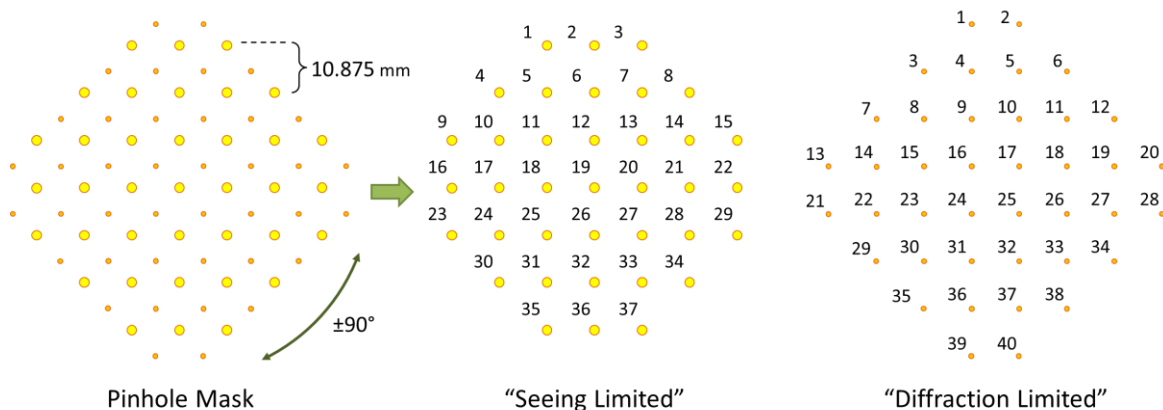
Figure 2-4: Pinhole mask features. A 7x7 grid of seeing-limited pinholes is nested inside an 8x8 grid of diffraction-limited pinholes. Both grids have a spacing of 10.875mm (0.34' on sky). A selector plate is used to expose either the diffraction limited pinholes or the seeing limited pinholes. A motorized rotation stage is used to simulate ±90° of field rotation.

Phase Screen Mechanism: Two deployable phase screens are inserted into the path to simulate atmospheric turbulence at altitudes of 5 and 10km. Each phase screen is a glass annulus with a Kolmogorov turbulence pattern etched into its surface[38]. The variation of glass thickness recreates turbulent air's refractive index distribution. Time variations of the turbulence, normally caused by the wind, are achieved by rotating the disc.
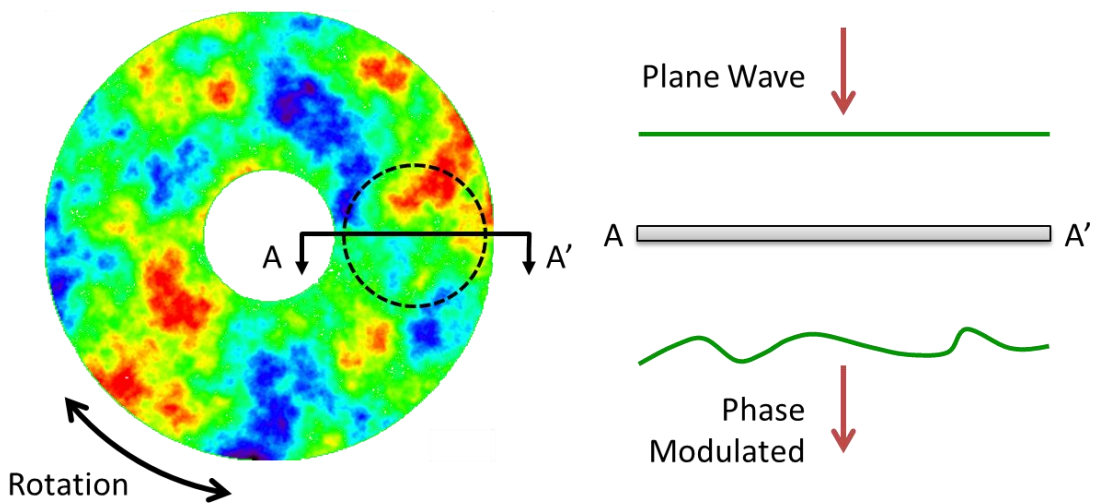
Figure 2-5: Raven's 10km phase screen. A Kolmogorov turbulence pattern is etched into its glass surface (coloured regions). Planar wavefronts traveling through the glass will be aberrated by the variable glass thickness. The black dashed line shows the region the light passes through. The screens rotate to produce time varying turbulence. The 5km screen works the same way.

The 10km screen is ~30% larger in diameter than the 5km screen to accommodate a larger beam footprint (see Figure 2-2). The specifications for the phase screen mechanism are shown in Table 2-1.

Table 2-1: Phase screen specifications

	5 km Screen	10 km Screen	Unit
Fractional C_N^2	0.224	0.180	
Effective Wind Speed	3-9	9-25	[*m/s*]
Rotation Speed	2.5-7.5	5-15	[*RPM*]
Beam Footprint	34	46	[*mm*]

CDM: The calibration deformable mirror (ALPAO277-25) is used for simulating ground layer turbulence and for calibrating Raven. It has 277 actuators in a 17x17 grid over a 30mm pupil diameter. It is the only common optical surface to all of the sources, making it an ideal calibration tool. More information about the CDM's design and how it operates can be found in section 2.4.2.

After the CDM a group of lenses representing Subaru's mirrors refocuses the light, creating a focal plane with a 2.7' FoR, at a required focal length of 17m. A flip mirror is used to select whether the light from the CU (during testing) or Subaru (during observation) enters Raven. The CU can also simulate a centrally located LGS source, which is not relevant to this work.

2.3 OPEN-LOOP WAVEFRONT SENSOR DESIGN

2.3.1 WAVEFRONT SENSOR DESIGN

Wavefront phase cannot be measured directly, so it must be somehow converted to an intensity profile, which can be recorded by conventional optical sensor like a charge coupled device (CCDs). Once the intensity profile is recorded, the wavefront can be computationally reconstructed back into phase space, thereby providing critical information on the light's path through the atmosphere. There are many different techniques capable of performing this transformation, and the selected method is

instrument specific. Raven uses **Shack-Hartmann** Wavefront Sensors (SHWFSs), which are a popular choice for AO systems. A schematic of a generic SHWFS, with and without the presence of turbulence, is shown in Figure 2-6.
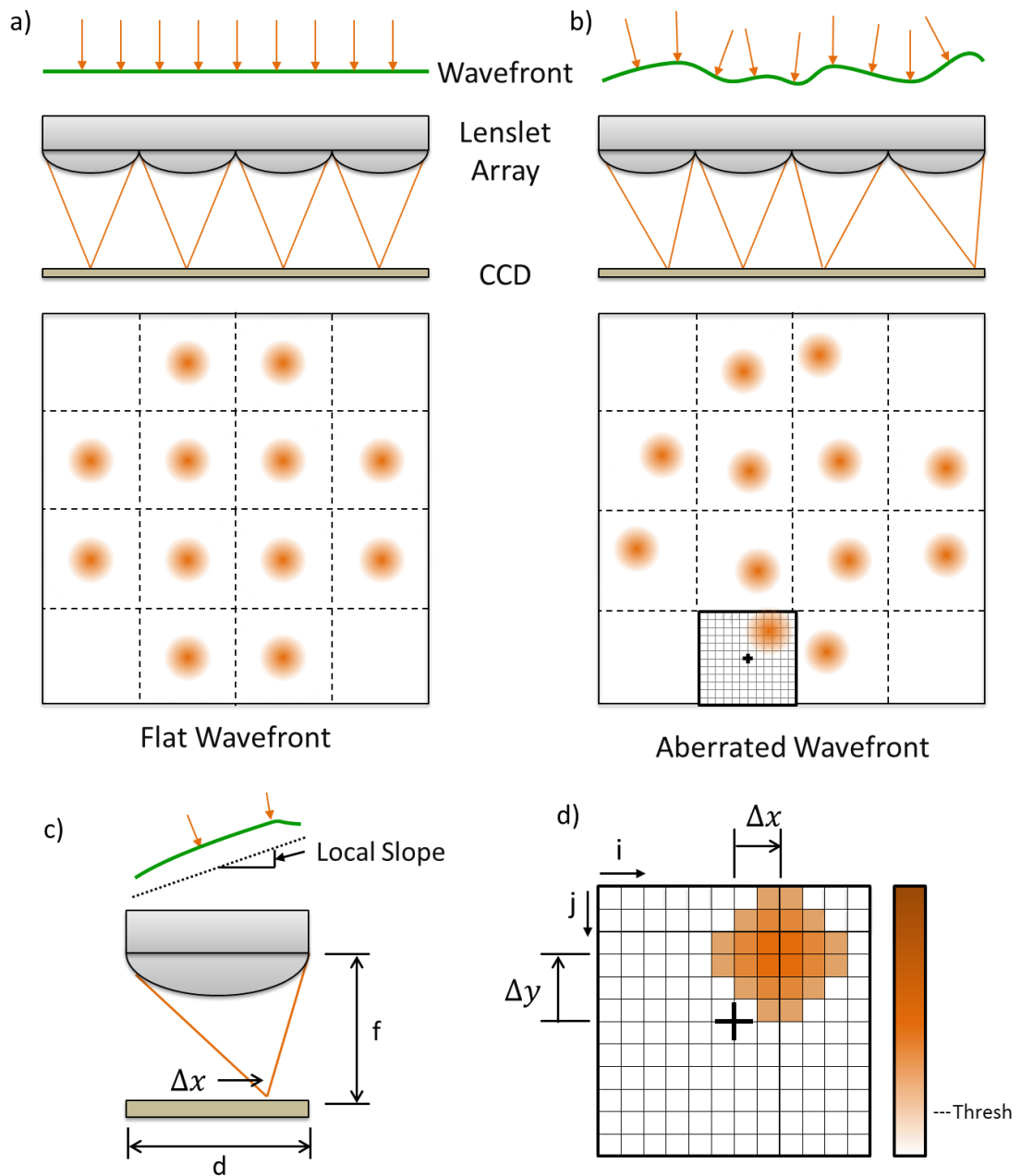
Figure 2-6: Schematic of a Shack-Hartmann WFS. a) A planar wavefront passing through a lenslet array creates an orderly array of focused light spots onto the pixels of a CCD, with each spot centered within its subaperture. b) A distorted wavefront creates spots whose positions indicate the local wavefront slope above the lenslets c) A more detailed view of a

single lenslet showing the pertinent dimensions d) Pixel measurements of one subaperture. The intensity threshold is shown on the color bar to the right

A SHWFS works by first discretizing and focusing the wavefront of an NGS, using a grid of small lenses called **a lenslet array**. This generates an array of focused **spots** that are imaged onto the pixels of a CCD. The location of each spot relative to its location when measuring a flat wavefront indicates the local **slope** of the wavefront above its lenslet. Measuring and combining all the local slopes generates the full phase information across the wavefront. Eqn. 2-1 shows the calculation for determining the local wavefront slope over a specific lenslet based on the system geometry described in Figure 2-6c.

$$local\ wavefront\ slope\ [rad] = \frac{\Delta x f}{d} \qquad \textbf{2-1}$$

Where the lenslet focal length is f and the lenslet pitch is d. The x-y spot locations are measured using a **thresholded center-of-gravity**[i] (TCoG) calculation shown in Eqn. 2-2. Pixels with intensities below a certain threshold are ignored to reduce the influence of noise from the CCD, and from stray light not related to the measurement. The threshold is sub-aperture dependent, as spots in the center are usually brighter than spots on the periphery. For simplicity, the slopes on Raven are defined as the x-y spots positions, measured in pixels. The focal length and pitch terms are left out, as their impact is taken into account during calibration.

$$slope_x\ [pixels] = \Delta x = \left(\frac{\sum x_{i,j} I_{i,j}}{\sum I_{i,j}}\right)_{I>thresh} \qquad \textbf{2-2a}$$

$$slope_y\ [pixels] = \Delta y = \left(\frac{\sum y_{i,j} I_{i,j}}{\sum I_{i,j}}\right)_{I>thresh} \qquad \textbf{2-2b}$$

The x-slopes and y-slopes are combined into a **slope vector**, which can be easily used during mathematical operations. The vector consists of all the x-slopes, followed by all of

---

[i] In addition to the TCoG calculation, Raven is also experimenting using a "correlation centroiding" method. Though this method could potentially provide better results, it was not yet implemented at the time this document was written

the y-slopes, making it twice as long as the number of WFS spots. A visual description of how the slope vector is populated is shown in Figure 2-7.

$$slope\ vector = [\Delta x_1 \cdots \Delta x_n, \Delta y_1 \cdots \Delta y_n]$$ **2-3**

$$[S] = [\Delta x_1 \quad \cdots \quad \Delta x_{10} \quad \cdots \quad \Delta x_{12} \quad \Delta y_1 \quad \cdots \quad \Delta y_{10} \quad \cdots \quad \Delta y_{12}]_{1 \times 24}$$
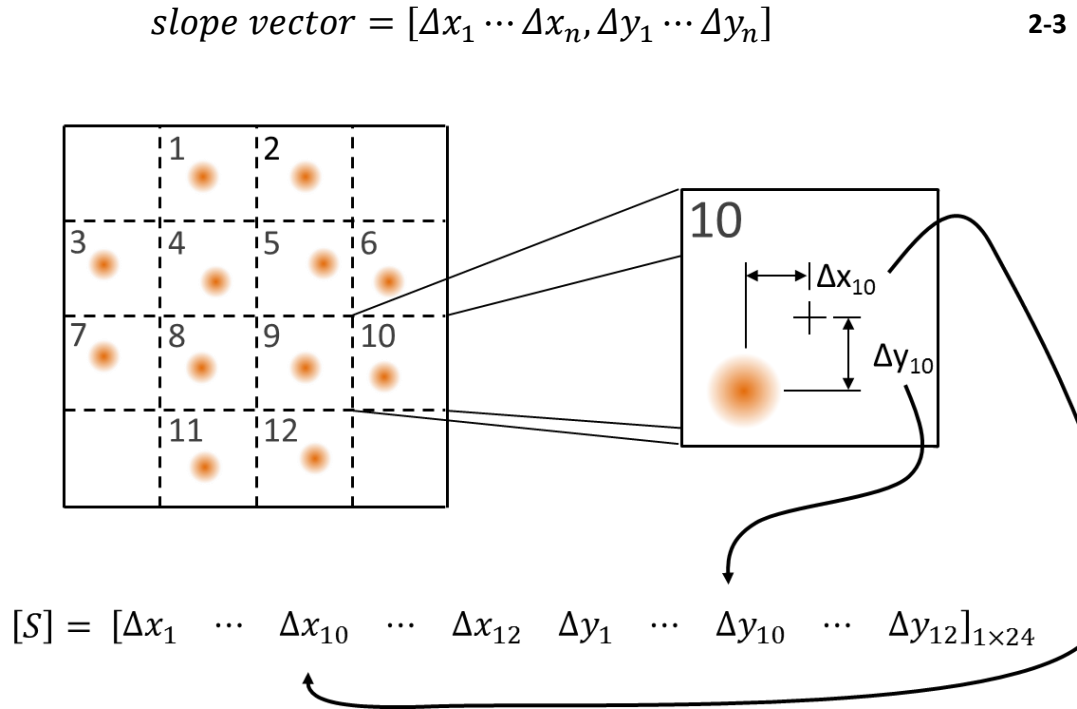
Figure 2-7: Formation of the slopes-vector. All of the local x slopes are followed by all of the y-slopes.

Optical imperfections within the WFS lead to the spots not being perfectly centered in their subapertures when a flat wavefront is measured. The slopes measured with a flat wavefront are saved as a **slopes-offset** vector, which is subtracted from all subsequent slope measurements. In closed-loop AO systems, the NGS wavefront is flattened by the DM, so the recorded spots should be close to their center at all times. Alternatively in open-loop AO, the full wavefront error is measured, and the spots wander around their subapertures.

The SHWFS is most notable for its simplicity, and the linear relationship between the local wavefront slopes and the measured spot positions. Additionally each spot can freely travel within its own subaperture, permitting a large dynamic range. The sensitivity of a SHWFS is low when compared to other WFS options, like a non-linear curvature WFS[39] or a pyramidal WFS[40]. These designs alternatively sacrifice linearity and dynamic range.

2.3.2 OLWFS Opto-Mechanical Design

The optomechanical design of an OLWFS used on Raven is shown in Figure 2-8. All of its optical components are mounted concentrically. Fundamentally this design works the same way as described by Figure 2-6.

A	Pick-Off Mirror
B	Collimating Lens
C	Sodium Filter
D	Lenslet Array
E	1:1 Relay
F	CCD Sensor
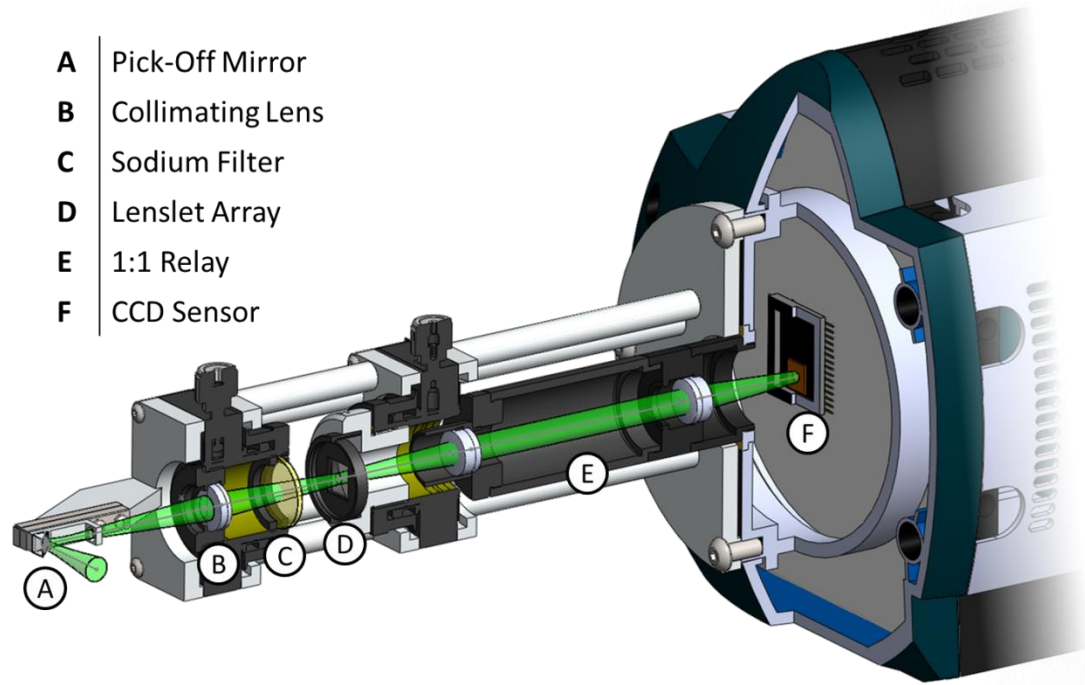
Figure 2-8: Sectioned model of the OLWFS optomechanical design for Raven. The pick-off mirror (A), extracts guide star light from the focal plane. The light is then collimated (B), and sent through a lenslet array (D). A 1:1 optical relay (E) reimages the spots onto a CCD sensor (F)

A. **Pick-Off Mirror (Thorlabs MRA05-P01):** A flat 7.1x5mm silver coated pick-off mirror, angled at 45°, extracts light from an NGS (shown in green). 20mm after the mirror a field stop limits the OLWFS's FoV to 4.8'.

B. **Field Lens:** A lens collimates the guide-star light and places it on the lenslet array at **D**. It is mounted on an x-y-z manual adjustment stage (Newport LP-05A).

C. **Sodium Notch Filter**: A 589.2 nm notch filter is inserted between the field lens and lenslet array to attenuate potential light contamination from the LGS source.

D. **Lenslet Array (SUSS 18-1393-100-109)**: The lenslet array (d: 300μm, f: 4.77mm) splits the light into a 10x10 grid of foci. It is mounted on an x-y-z-θ_z adjustment mount (Newport LP-05A).

E. **1:1 Relay (2 × Edmund NT49-325-INK):** For mechanical convenience, the NGS arms needed to be lengthened. The foci from the lenslet array are optically relayed downstream using a 1:1 lens pair (d: 12.5mm, f: 35mm).

F. **CCD (Andor EMCCD X-iON):** The focused spots are recorded using an **electron multiplying CCD** camera (EMCCD), which is a much more sensitive version of a regular CCD sensor. Due to its size and rigidity, all of the OLWFS's optical components are rigidly mounted to the camera. The 1:1 relay is screwed into the camera's threaded aperture, while the rest of the optical components are mounted to a mechanical structure fixed to the camera's face. The CCD sensor is cooled to cryogenic temperatures (-100°C), using thermoelectric coolers, to improve reduce the effects of thermally induced noise. The heat is removed using a liquid glycol heat exchanger located within the camera body. Each pixel can discretize its measured intensity signal with a sensitivity of up to 2^{14} graduations. This value, referred to as the **pixel depth**, is measured in analog-to-digital-units (ADUs)

The main specifications of the OLWFSs are summarized in Table 2-2.

Table 2-2: OLWFS specifications

Active pixels on CCD	128×128
Pixel size	24×24 μm
Pixel depth	14 bits ($2^{14} = 16384$ ADU)
# of subapertures (spots)	10×10
WFS FoV	4.8"
Pixel scale	0.38 "/pixel
Spectral range	500-900 nm
Frame rate	up to 500Hz

2.3.3 X-Y Motion Platform Design for NGS Arms

Each OLWFS arm is mounted on an x-y translation platform, consisting of two PI M-410.DG stages, which provide 100mm of travel. The stages consist of a movable sled mounted to crossed-roller bearings, and a lead screw rotated by a DC motor provides motion. A rotary encoder mounted to the motor's shaft provides positional feedback. The motion platform's design is shown in Figure 2-9. The OLWFS is not shown for clarity.

A	X-Stage
B	Y-Stage
C	OLWFS Interface
D	Constant Force Spring
E	Cable Carriers
F	Glycol Lines
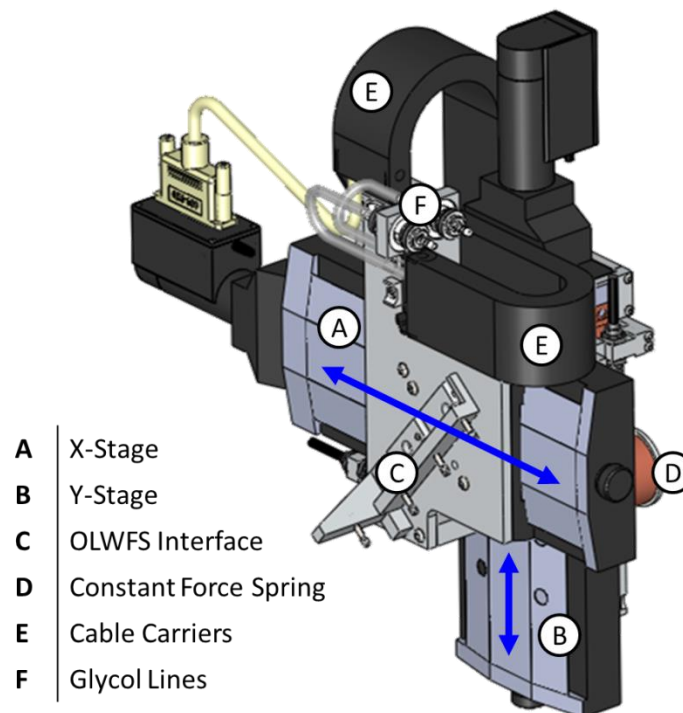
Figure 2-9: CAD design of the x-y motion platform for Raven's OLWFSs. The OLWFS is not shown for clarity. A 100mm horizontal stage (A), is mounted to a 100mm vertical stage (B). The OLWFS is mounted at (C). Two constant load springs (D) provide an upward force allowing the vertical stage to function within its specifications. Cable carriers (E), provide unobstructed travel for the associated wires and glycol lines (F)

The OLWFS is mounted directly to the horizontal x-stage, which is itself mounted to the vertical y-stage. Two 2.6kg constant force springs (Misumi CFS2.6) support some of the OLWFS's and x-stage's mass, allowing the y-stage to operate within its maximum load specifications.

2.3.4 FIELD COVERAGE OF NGS ARMS

The three NGS arms are mounted radially around the FoR at angles of 40°, 140° and 270° (with 90° being vertical). Figure 2-10 shows the NGS arm mounting configuration, what the arms look like in the CU's FoR, and an example of recorded wavefront spots.

Figure 2-10: Open loop wavefront sensors. (A) CAD design of OLWFS arms and their support gantry, (B) CU field containing the OLWFS arms, (C) sample wavefront sensor spots from one of the CU sources

The numbering convention for the OLWFSs shown by this figure will be extensively used throughout the remainder of this document. The field coverage of the NGS arms is shown in Figure 2-11. Their large travel allows them to patrol Subaru's entire FoR (3.5' or 112mm diameter).
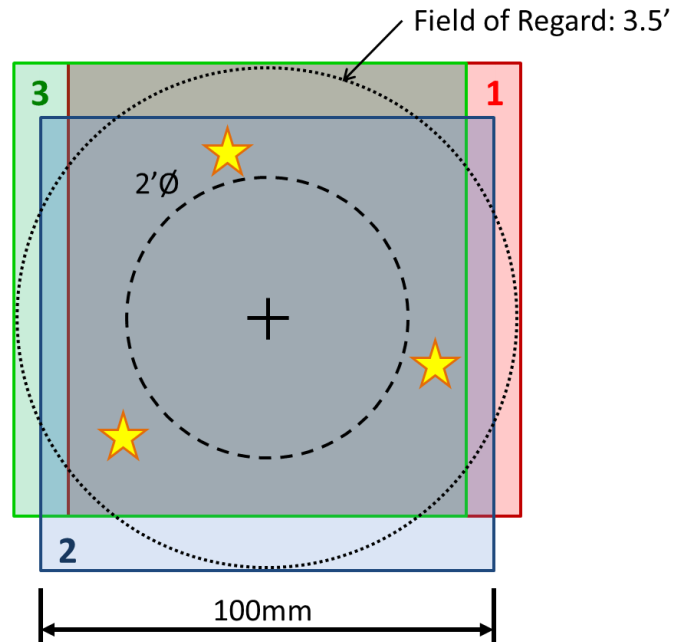
Figure 2-11: Field coverage of the three OLWFSs pick-offs. The 100mm x-y travel of each arm can accommodate almost any asterism in a 3.5'. The field coverage of OLWFS1 is shown in red, OLWFS2 in blue, and OLWFS3 in green

The overlapping regions pose a significant risk for collision. Extensive effort has been made to mitigate this risk, including collision avoidance software and emergency stop procedures. A picture of the completed NGS arms 1 and 3 is shown in Figure 2-12.
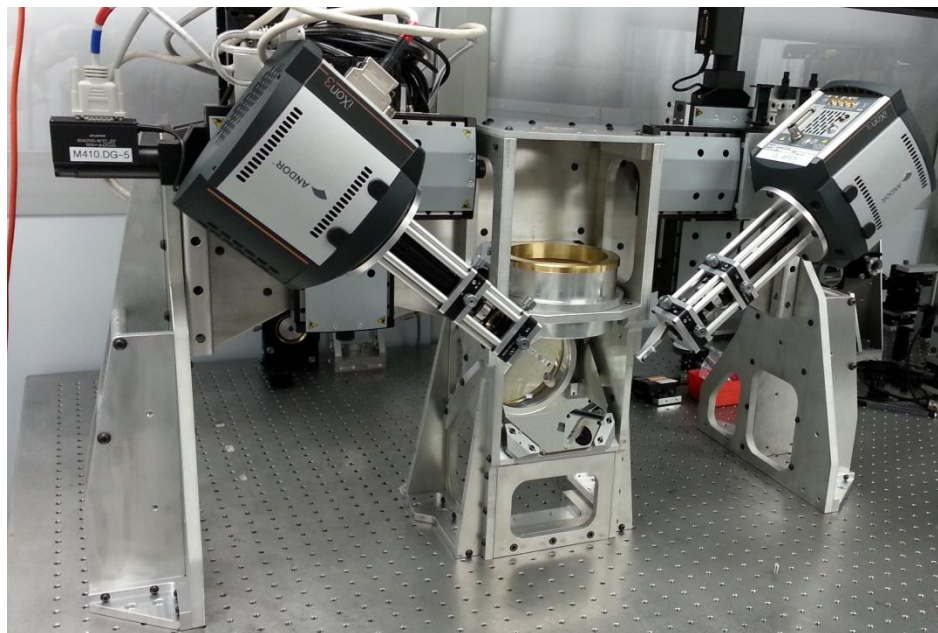
Figure 2-12: NGS pick-off arms 1 and 3, during temporary placement on a side bench

2.4 SCIENCE PATH DESIGN

The science paths are responsible for extracting science target light from the FoR, correcting its wavefront with a DM, and sending the corrected light to IRCS. A schematic overview of the main components of a science path is shown in Figure 2-13. The science pick-off arms, the science deformable mirrors (SDMs), and the tip/tilt platforms (TTPs) can all correct for tip/tilt, and will be discussed in detail. These actuators must work together to keep the two science target output images centered on the IRCS slit.
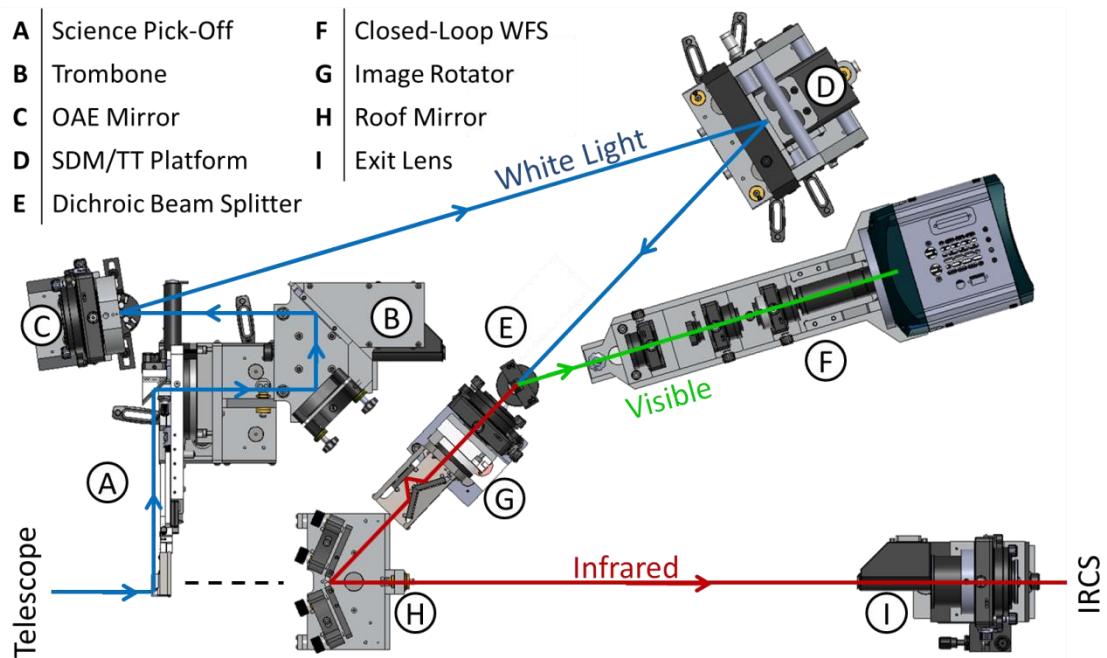
Figure 2-13: Top-view of the science path for Raven. Science light is picked off (A), and a trombone (B) compensates the optical path length. The light is reflected by an off-axis ellipsoidal mirror (C) to refocus it. A deformable mirror (D) corrects the wavefront aberrations. The visible spectrum of the light is reflected using a dichroic beam splitter (E) to the CLWFS (F). The transmitted infrared component can be optically rotated using a k-mirror (G), and combined with the light from the other science path (not shown) using a roof mirror (H). An exit lens (I) places the foci at the correct length for IRCS. Broadband light is shown as blue, visible as green and infrared as red.

2.4.1 SCIENCE PICK-OFFS

The science pick-off arms (SciPOs) are located 20mm behind the telescope's focal plane, 35mm behind the OLWFS pick-off plane. The pick-off mirror is mounted on a

motorized r-Ө mount to move within the FoR. A simplified schematic of Raven's SciPOs is detailed in Figure 2-14.
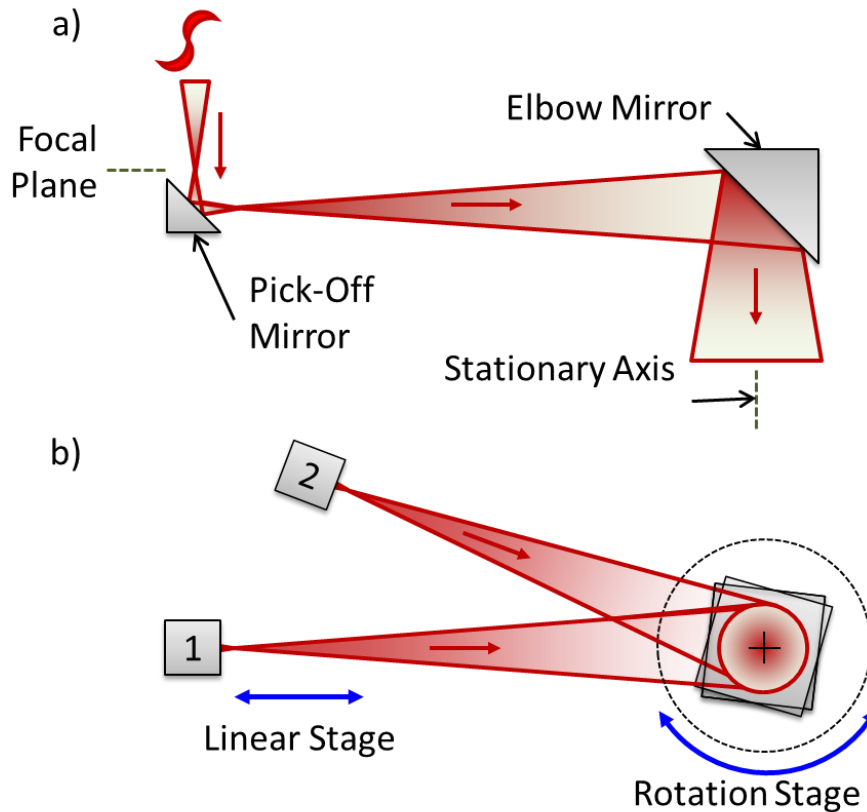
Figure 2-14: Top-view of science pick-off design (a). Two potential locations for the science pick-off mirror are shown in the elevation view (b). The linear stage mounted to a rotation stage allow the arm to have a stationary output axis

The SciPOs are designed as **telescopic rotating periscopes**, consisting of two mirrors and two motorized stages. The science light first reflects off a 6x8.5mm custom convex toroidal pick-off mirror, which acts as the science path's field lens. The pick-off mirror is mounted on a 50 mm motorized linear stage (PI M-227.50) that moves radially from the arm's motorized rotation axis (PI M-038.DG). Both of these stages utilize DC motors and rotary encoders. A fold mirror, referred to as the elbow mirror (Thorlabs MRA25-P01), mounted to the rotation stage is used to reflect the science light through the rotation axis. In this configuration, the output science light beam is always concentric to the arm's rotation stage axis, regardless of the pick-off mirror's position. The mechanical design for

Raven's science pick-off arm is shown in Figure 2-15. More detailed assembly drawings are provided in Appendix A.
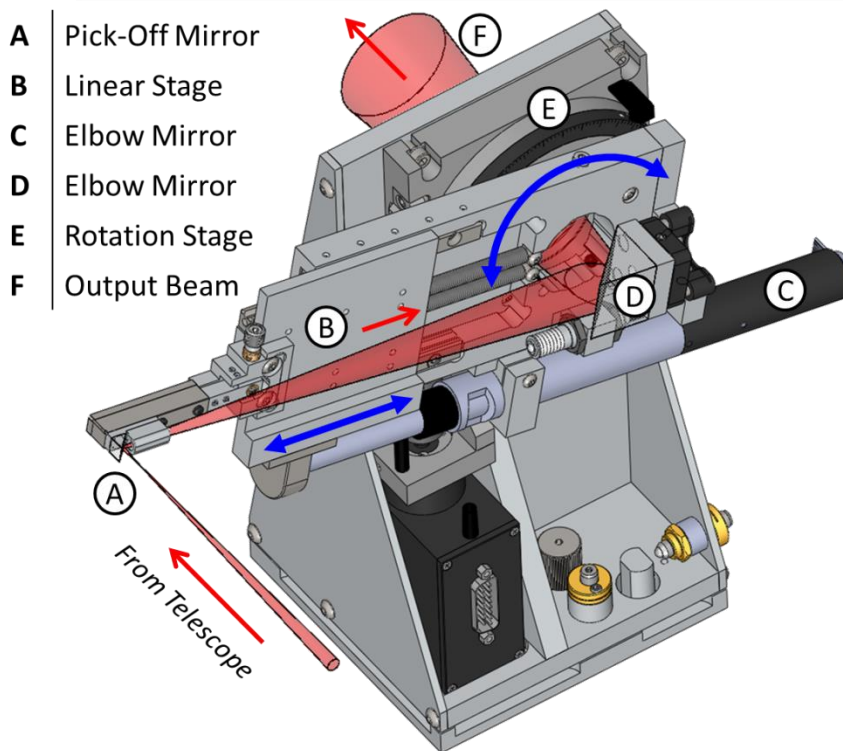
Figure 2-15: Science Pick-Off CAD Design. Science light (shown in red) is reflected by the pick-off mirror (A) and sent to the elbow mirror (D). A motorized r-θ mount (motions shown in blue) is used to move the pick-off mirror to the correct location within the FoR

The field coverage of the science pick-off arms is shown in Figure 2-16. The arms have a large overlapping region, enabling the two science targets to be on the same side of the field if necessary.
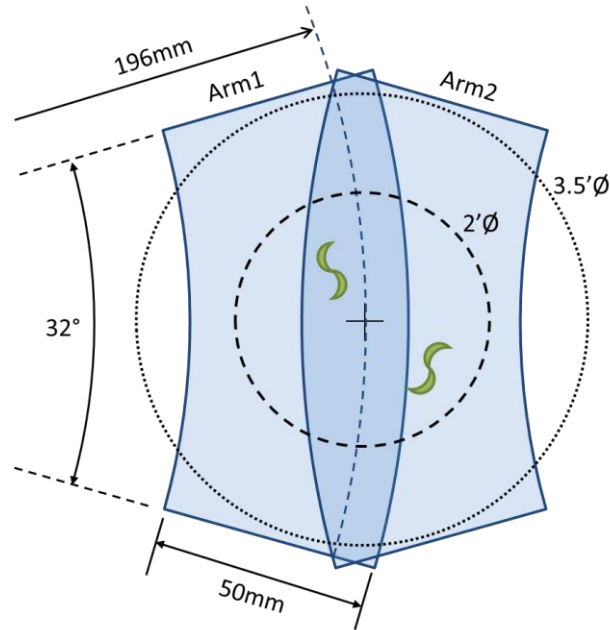
Figure 2-16: Science Pick-off field coverage. The region each pick-off can patrol is shown in blue. Both arms have an angular range of ±16° and a radial range of 50mm.

The 50mm linear stage imposes variability in the science arm's optical path length. To compensate, both SciPOs are followed by an optical device called a **trombone**, to keep the path length constant. Following the trombone the science light is refocused by an off-axis-ellipsoidal mirror (OAE), forming a pupil on the SDM.

2.4.2 SCIENCE DEFORMABLE MIRRORS

The deformable mirrors chosen for Raven utilize magnetic voice-coils to modulate the shape of the reflective surface. The mirror surface is a silver-coated silicon membrane with a grid of permanent magnets fixed to its non-reflective side. Voice coils on a substrate beneath the mirror, can push or pull at the magnets to control the shape of the mirror. The amount of magnetic force is defined by the amount of electrical current in the coil. A cross-section example of this technology is shown in Figure 2-17. Only one row of the actuator grid is displayed.
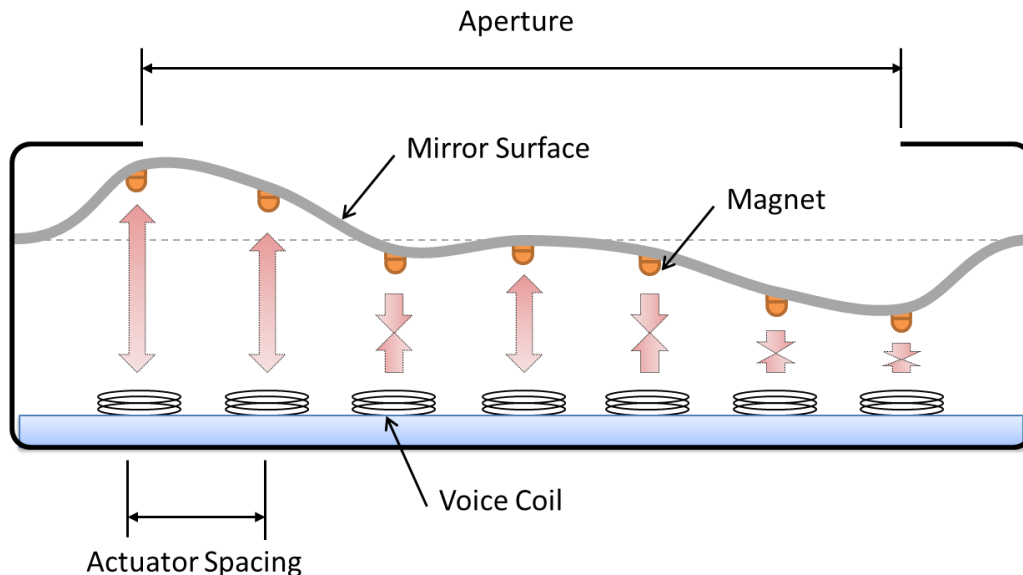
Figure 2-17: Operating principle of a magnetic voice-coil deformable mirror. Magnets fixed to the back of flexible reflective membrane are actuated by the amount of electrical current in their corresponding voice coils. Only one row of actuators is shown.

This style of DM has negligible hysteresis, high stroke, and linear relationship between supply current and stroke[41], which are essential properties for open-loop correction. The SDM's number of actuators, their spacing and their stroke was selected based on simulations[42]. A summary of the final design is shown in Table 2-3 and Figure 2-18. All of the DMs used on Raven were fabricated by ALPAO.

Table 2-3: Science DM specifications

Clear aperture	30 mm
Pupil diameter	25 mm
Actuators	145 (13x13 grid)
Pitch between actuators	2.5mm
Tip-tilt stroke	275"
Bandwidth	700 Hz
Coating	Silver Protected
Best flat	8.0 nm RMS
Settling time	1.0 ms
Optical deformation	60μm (peak to valley)
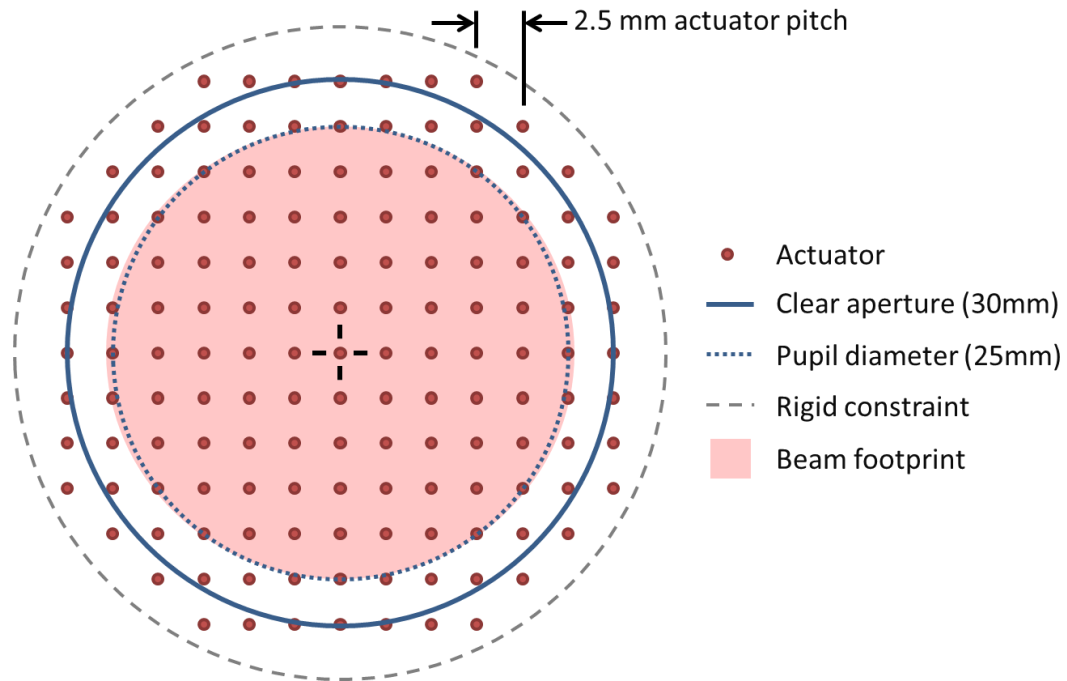
Figure 2-18: Actuator spacing and aperture size of the science deformable mirrors. The beam footprint is horizontally elongated by 3.5% due to the 15° incident angle.

It can be seen that most of the SDMs outer actuators are not within the beam footprint. This will be important later, during calibration, when the influence of each actuator needs to be measured.

The manufacturing technique used to make the SDMs requires the reflective membrane to be rigidly constrained around its perimeter. Consequently non-linear effects can occur when the outermost actuators try to create a large stroke, specifically when the SDM is attempting to make a tipped or tilted shape. To mitigate these effects, the SDMs are mounted to tip/tilt platforms, designed to globally tip and tilt the entire mirror assembly instead of relying on the mirror to produce the tilted shape. In this configuration the SDM should be able to operate more linearly, and its actuators can be more efficiently used for correcting higher order wavefront aberrations instead of tip/tilt. According to the SDMs specifications summarized in Table 2-3, a maximum tip/tilt of 0.23° is possible. This value, though comfortably higher than the 0.035° required by section 1.10.1, is not readily realizable due to the reasons just mentioned.

2.4.3 TIP/TILT PLATFORM

Each SDM is mounted on a tip/tilt platform (TTP) (PI: P-528.TCD). In this configuration the SDM is itself tipped and tilted thereby relieving it from compensating the entire wavefront tip/tilt. Each TTP consists of four piezoelectric actuators located in a square configuration, around a central square aperture. This geometry gives the platform three degrees of freedom: tip, tilt and piston (motion normal to mirror surface). By default, its controller actuates the platform about the center of its aperture. Figure 2-19 shows a coloured version of the TTPs used on Raven (in reality they are black).
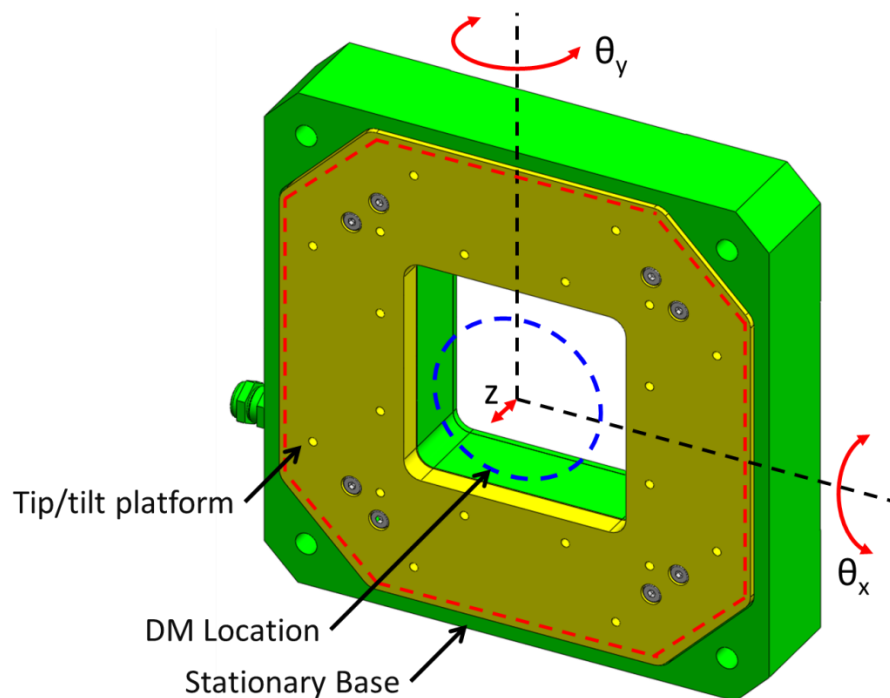
Figure 2-19: Tip/tilt platform used to tip and tilt an SDM. The green region is fixed and immobile while the yellow region is movable. The blue dashed line indicated the location of the SDM mirror

The platform has $0.114°$ of travel in tip and tilt, which is larger than the $0.035°$ requirement from section 1.10.1. Three capacitive sensors built into the TTP allow its actuators to function in a closed control loop. Figure 2-20 shows a model of the combined SDM/TTP mount used for Raven.
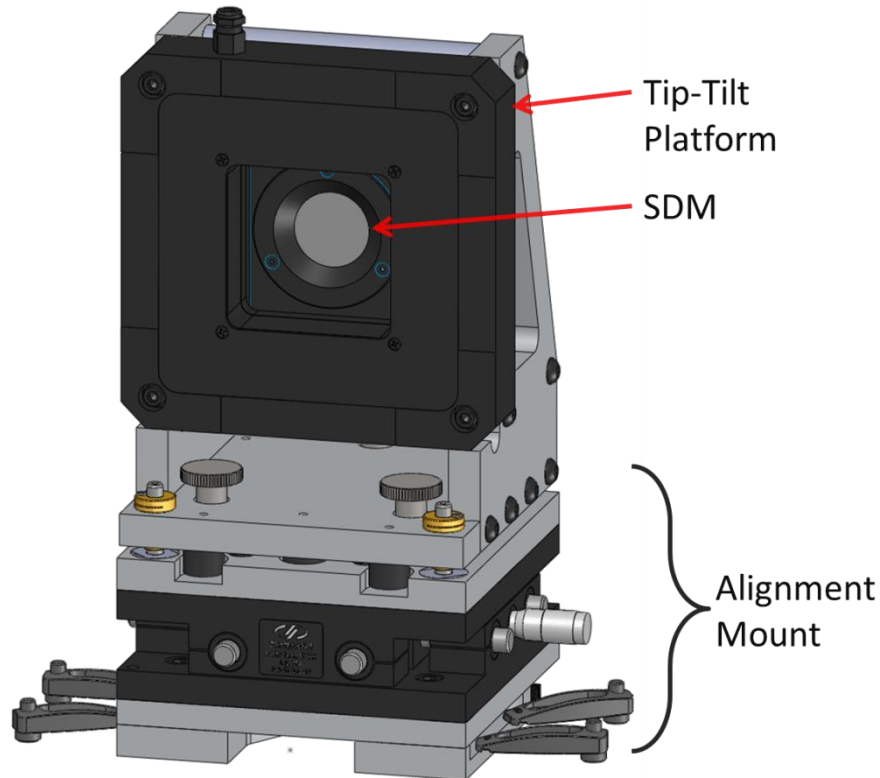
Figure 2-20: SDM Mount. The ALPAO DM is mounted on a PI tip/tilt platform. The entire SDM assembly is mounted on a 5 axis alignment mechanism

During an observation the SDMs and TTPs will be commanded in open-loop. However, during calibration and testing it is useful to calibrate and characterize their performance. Subsequently, closed-loop WFSs were integrated into each science arm.

2.4.4 CLOSED-LOOP WAVEFRONT SENSOR

After the SDM, a low wavelength-pass (LWP) dichroic beam splitter, with an 800nm transition, is used to reflect visible light to a **closed loop wavefront sensor** (CLWFS), and pass infrared light for eventual entry into the IRCS slit. The CLWFSs observe the corrected wavefront of their source, similar to an SCAO system. However information from the CLWFSs cannot be gathered in real-time during an observation because the science targets are usually too faint or not compact enough to be useful for wavefront sensing. The CLWFSs are predominantly used during calibration and testing, when bright sources can be used in place of science targets. The optical design of the CLWFSs is nearly identical to the OLWFSs, but without the pick-off mirror and x-y motion platform.

2.4.5 IMAGE ROTATORS AND ROOF MIRROR

Each science arm has an image rotator that can align elongated science targets with the IRCS slit, to maximize throughput (think hotdog in a bun). The rotators consist of three, gold coated, flat mirrors arranged in a "K" formation. The mirror assembly is mounted to a rotation stage (PI: M-037.CG) which rotates the "K" by an angle θ, rotating the output image relative to the input image by 2θ.

After the rotators, the roof-mirror is used to combine the light from science targets in preparation for their entry into IRCS. The design of the roof mirror is shown in Figure 2-21. It consists of two gold coated, slightly convex mirrors, at a shallow angle to one another.
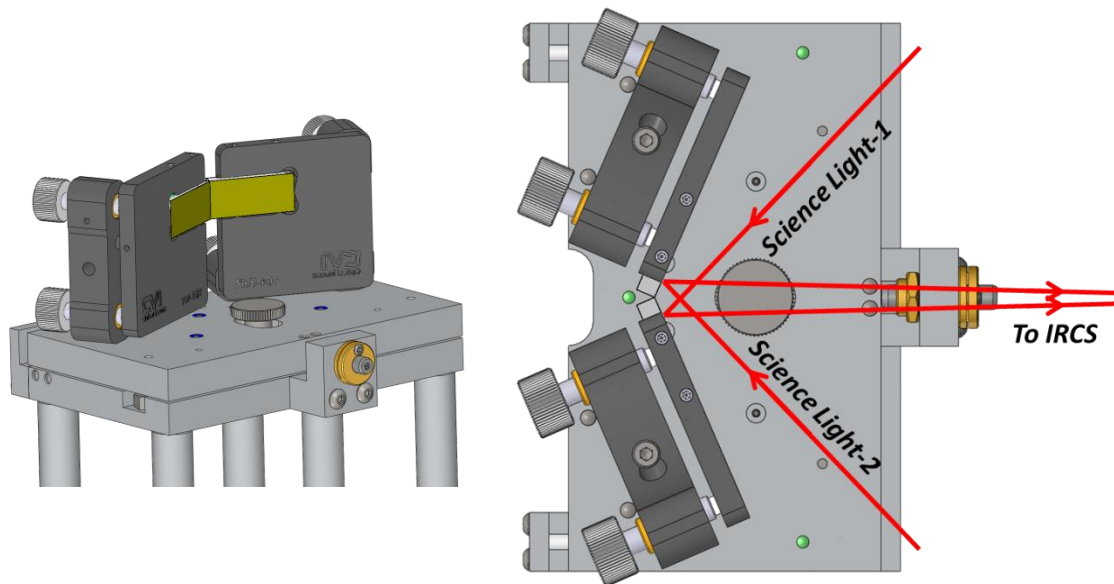
Figure 2-21: CAD design of the roof-mirror. The light from both science paths is combined here using two gold coated convex mirrors.

After the roof-mirror, both beams of science light, pass side-by-side through the exit lens. The science light can be sent to either IRCS, during an observation, or to a laboratory "science camera", during testing.

2.4.6 SUMMARY OF SCIENCE PATHS

A sophisticated alignment strategy was required for assembling the science paths. The multitude of moving parts makes alignment substantially more involved compared to a stationary system, because motion axes must be sufficiently aligned to optical axes. Raven's completed science arms are shown in Figure 2-22. The NGS pick-off arms were not mounted at the time the picture was taken.
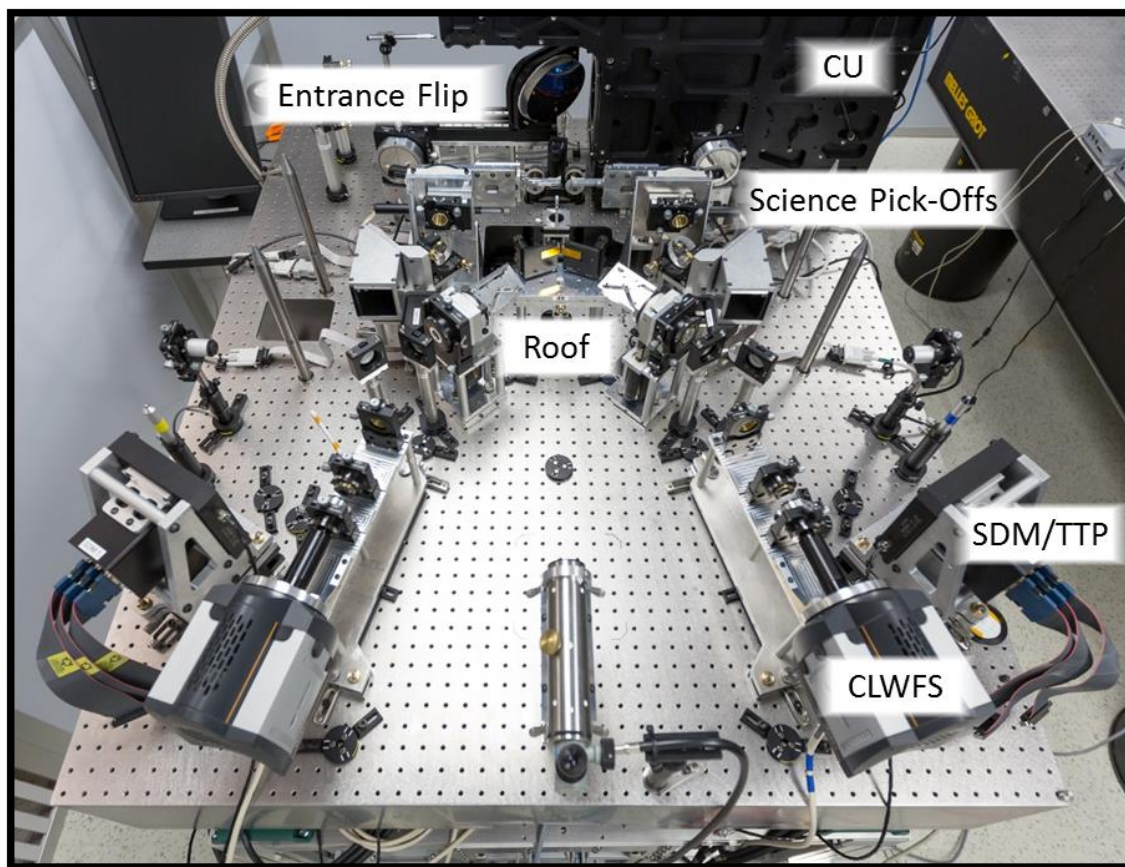
Figure 2-22: Raven's completed science paths after their alignment. Essential components are labelled. OLWFSs were not installed at the time of the photo.

2.5 IRCS AND THE SCIENCE CAMERA

During an observation, light from Raven's two science arms will enter IRCS's slit side-by-side, with each target occupying half of the slit (see Figure 3-2 of the following chapter). This is not the intended functionality for a spectrograph, as usually only one light source enters at a time. Future MOAO systems will have IFSs built into each arm.

IRCS's 0.140" slit drives many of the design decisions on Raven, and will eventually quantify the performance of Raven's the tip/tilt compensation system.

In the lab, an infrared science camera (Photonic Science AG7593) is used to simulate IRCS. It is able to image both science targets simultaneously, and it can measure their resulting ensquared energy. An exit **flip mirror** is used to direct the science light to either the science camera or to IRCS.

2.6 SUMMARY OF RAVEN'S EXPERIMENTAL APPARATUS

Raven's optomechanical design has been discussed, with emphasis on the sensors and actuators relevant to its tip-tilt compensation system. The mechanics were fully assembled in January 2013 in Victoria, and then reassembled in January 2014 in Hilo, Hawaii. Figure 2-23 shows Raven's completed science and NGS pick-off arms.
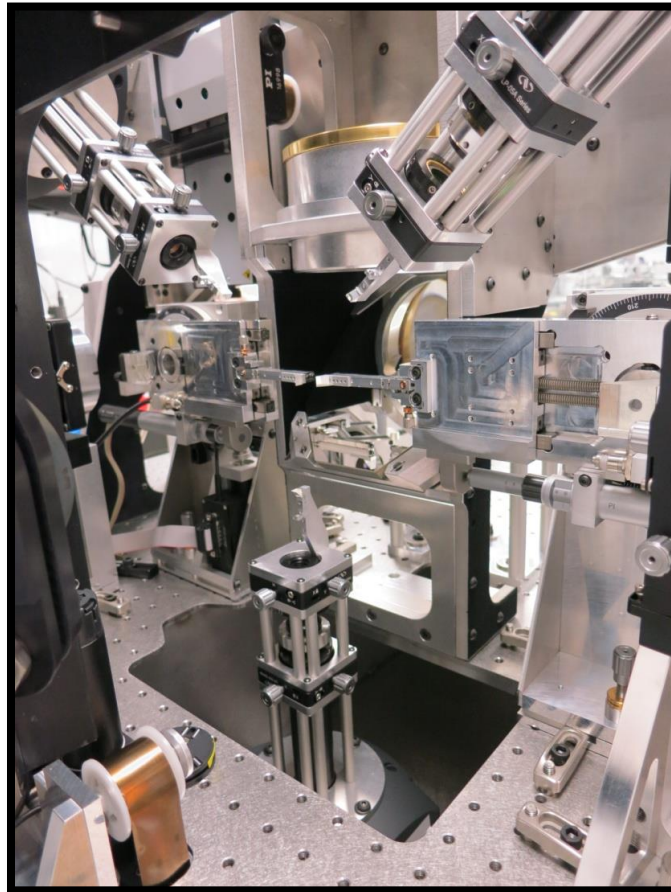
Figure 2-23: Raven's completed pick off arms. The three open-loop wavefront sensors are at 2:00, 6:00 and 10:00. The two science arms are at 3:00 and 9:00.

3 SENSOR AND ACTUATOR TUNING

Raven's optical sensors (OLWFSs, CLWFSs, and science camera) and mechanical actuators (motorized stages, tip/tilt platforms, deformable mirrors) need to be internally tuned and characterized before they can be implemented on the instrument. Each sensor and actuator has its own set of control parameters that can be altered to ensure optimal performance on Raven.

3.1 TUNING AND CHARACTERIZING RAVEN'S WFSs

As discussed in section 2.3.2, the light entering Raven's WFSs is sampled by a 10x10 lenslet array, creating a grid of focused spots recorded by the pixels of a CCD. The pixel intensity is recorded in analog-to-digital units (ADU), with a maximum value of 16,384. There are 3 parameters available for tuning within the WFSs: the **exposure time**, the **EMCCD gain**, and the **intensity threshold**. The exposure time will be set based on the properties of an observation. The EMCCD gain is achieved by photons striking a pixel

creating an "avalanche" of electrons instead of the usual one. By increasing the gain, a more intense signal can be retrieved from a faint light source, though this also increases the shot noise of the sensor. The intensity threshold is set to best reduce the impact of noise and light contamination. The WFS parameter selection follows these steps:

1. Analyze the proposed science case, and its three guide stars. The expected brightness of each guide star should be retrievable from a catalog.

2. Move an OLWFS pick-off arm to its guide star, and record the resultant light intensity with the expected exposure time and gain, based on prior calibrations.

3. If the spots are too dim (<3000 ADU), increase the gain until it reaches a maximum value of 1000. At this point reduce the gain to 1, double the exposure time and increase the gain again. This process is repeated until the spots are bright enough. Alternatively if the acquired spots are initially saturating the CCD, the gain is simply reduced until they are ~80% of the pixel depth (12,000 ADU).

4. With the exposure time and gain selected, a **dark frame** can be recorded which represents the "static noise" of the CCD. The dark frame will be removed from subsequent pixel readings by software, after each frame is recorded. To record a dark frame, the WFS camera's shutter is closed, and 10 frames are recorded using the desired exposure time and EMCCD gain. The median intensity of each pixel is used to create the dark frame.

5. The threshold value for the TCoG calculations (see Eqn. 2-2) is then set to the larger value between 10% of the maximum pixel intensity, and 200 ADU. The threshold is set individually for each subaperture because interior WFS spots are usually brighter than spots on the periphery.

Figure 3-1 shows a frame recorded using OLWFS-2 on a seeing limited CU source with a flat wavefront (no turbulence). The 5 outermost subapertures from each of the four corners are ignored to accommodate the circular shape. Therefore, the number of focused spots considered by each WFS is 80.
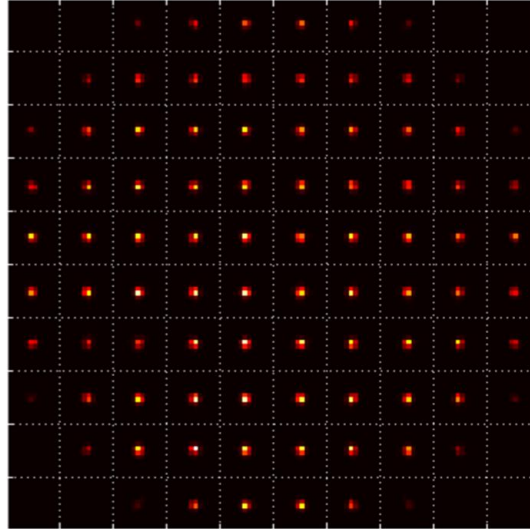
Figure 3-1: Lower OLWFS spots for a flat wavefront. All spots are centered within their subapertures. The color-map used is arbitrary, as the sensor can only record intensity.

3.2 SCIENCE CAMERA

In the lab, the IRCS slit is simulated by a group of pixels on the science camera. The ensquared energy (EE) of a simulated observation can be directly determined by measuring the amount of light entering those pixels, compared to the amount entering in the zero turbulence case. Based on Raven's design, the slit should have a width of 10 pixels on the science camera, and extend along the entire science camera's sensor. The exposure time of the science camera is set by first acquiring the desired sources with the science pick-off arms, then setting the exposure time so the measured intensity is just below saturation. At this point, the camera's shutter is closed, and a dark frame is measured. Figure 3-2 shows the output of the science camera recording the light from two diffraction limited sources, with no turbulence. This figure give a good indication of what the IRCS slit will look like during an observation with Raven.
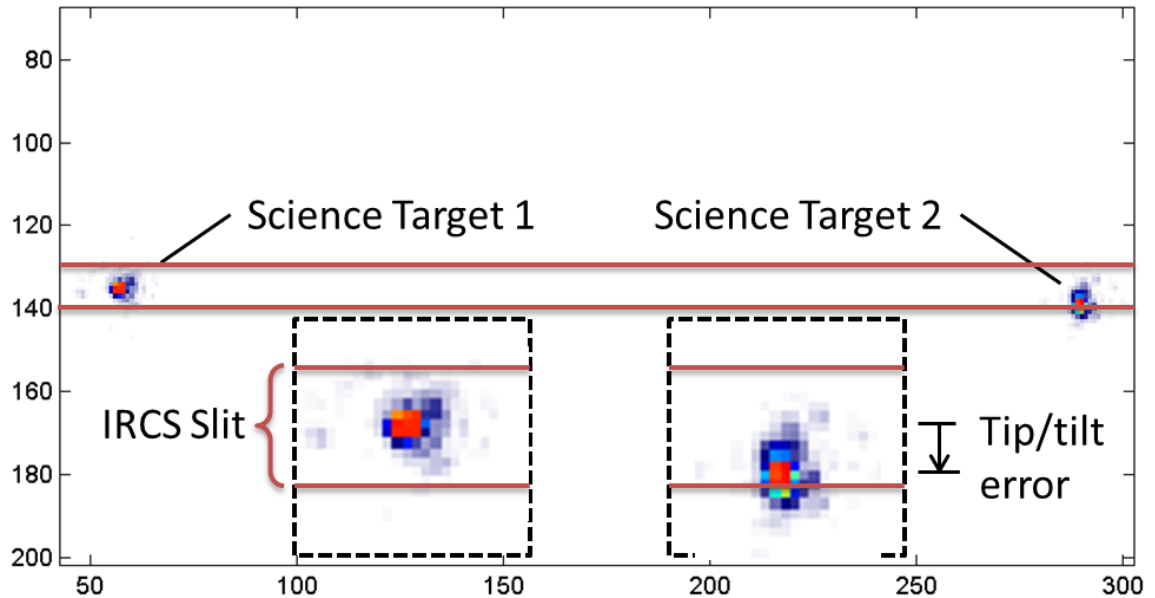
Figure 3-2: Science camera output. The light from two independent sources is recorded by the science camera. The slit can be simulated by a group of pixels, and the ensquared energy can be calculated by measuring the amount of light entering those pixels compared to the no-turbulence case.

During an "artificial observation", the goal of the tip/tilt compensation system will be to keep the sources centered within the slit-pixels. The previous figure clearly shows science target-1 well centered within the slit, while a noticeable tip/tilt error has developed on science target-2.

In the lab, the science targets will usually be bright enough for their wavefronts to be measured by the CLWFSs, giving a detailed analysis of the system's functionality. However, the science camera provides the ultimate measurement of overall performance, being able to directly measure critical optical metrics like Strehl Ratio, full-width-at-half-max, and Ensquared Energy.

3.3 PICK-OFF ARM CONTROL PARAMETER SELECTION

3.3.1 TRAJECTORY GENERATION

The controllers (PI: C-863 Mercury) used for communicating with Raven's motorized stages only support point-to-point motion, with trapezoidal velocity curves. Upon receiving a new positional command, the controller generates a trajectory consisting of three phases: constant acceleration, constant velocity, and constant deceleration. Next, it

starts a 20 kHz PID (proportional, integral, derivative) control loop between the motor voltage, and its shaft mounted rotary encoder. A simulated trajectory is shown in Figure 3-3.
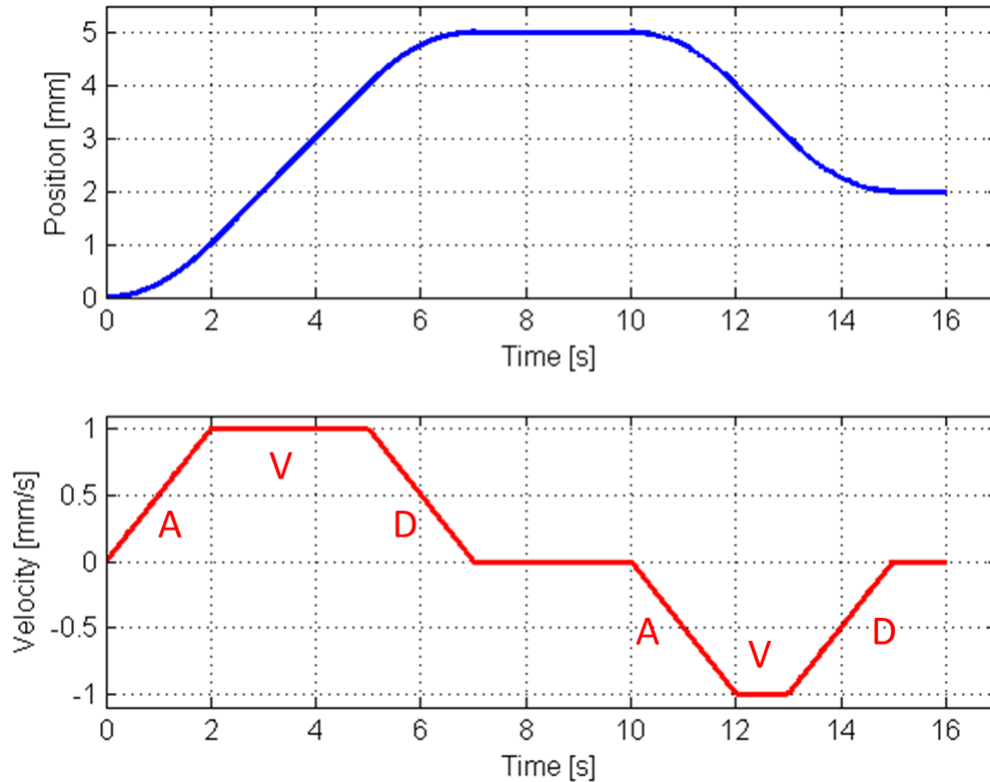
Figure 3-3: Simulated trapezoidal motion profiles. Position (blue) and velocity (red) profiles generated for a desired position of 5mm at t=0s, and 2mm at t=10s. Acceleration and deceleration are set to 0.5mm/s^2 and the maximum velocity is 1.0 mm/s

Ultimately there are seven parameters available for optimizing within a motor controller: the three trajectory parameters (ACC, DEC and v_{Max}), the three PID controller gains (Kp, Ki, Kd) and the command frequency (f_{COM}). Tuning these parameters to best utilize the stages is the subject of the following subsections.

3.3.2 TUNING TRAJECTORY PARAMETERS

The objective of a pick-off arm is to optically acquire an arbitrarily located target then accurately track its motion within the focal plane (its tip/tilt error). Increasing the trajectory parameters, while also increasing the command frequency (f_{COM}), will allow the stage to track higher frequency errors with less latency. However, large accelerations can mechanically load the arms causing misalignments, and commanding at high

frequency can excite mechanical resonances. Additionally, as the command frequency is increased, it may put unnecessary stress on Raven's computational hardware. Thus, tuning the trajectory parameters is a trade-off between using the smallest acceleration and command frequency possible, while still closely following the target's motion. A Matlab program was written to simulate the trapezoidal motion profile followed by the stages. The program was used to examine the effectiveness of different control parameters on following the tip/tilt platform data from AO188 (see section 1.11.3). Figure 3-4 examines the effect of using different accelerations and command frequencies over this data.
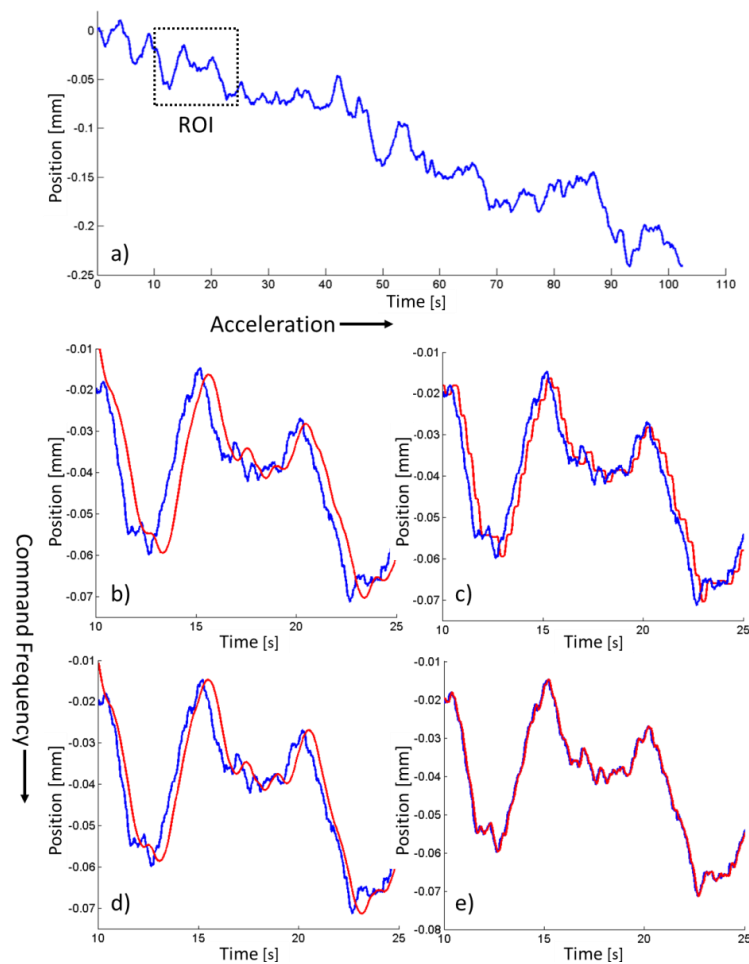
Figure 3-4: Tracking accuracy example using different acceleration and command frequency values. Subaru tip/tilt data is shown as red and the stage tracking position in red. a) Raw Subaru T/T data, region of interest (ROI) shown as dotted black box b) Low acceleration and low command frequency (0.05mm/s^2, 3Hz) c) High acceleration and low command frequency (0.5mm/s^2, 3Hz) d) Low acceleration and high command frequency (0.05mm/s^2, 50Hz) e) High acceleration and high command frequency (0.5mm/s^2, 50Hz)

As expected, high accelerations and high command frequencies result in the smallest following error (Figure 3-4e). Low acceleration and low command frequencies yield a smooth response with a notable latency (Figure 3-4b). High accelerations and low command frequencies create the "stepped" motion profile (Figure 3-4c). The steps are cause by the stage reaching its most recently commanded destination well before the next command is given. Low accelerations and high command frequencies yield a reduction in latency (Figure 3-4d). To adequately analyze these effects, a range of different command frequencies were simulated over a range of accelerations. The root-mean-square (RMS) error between the AO188 tip/tilt data and the simulated stage motion was then measured for each combination. The following figure shows the results of these simulations.
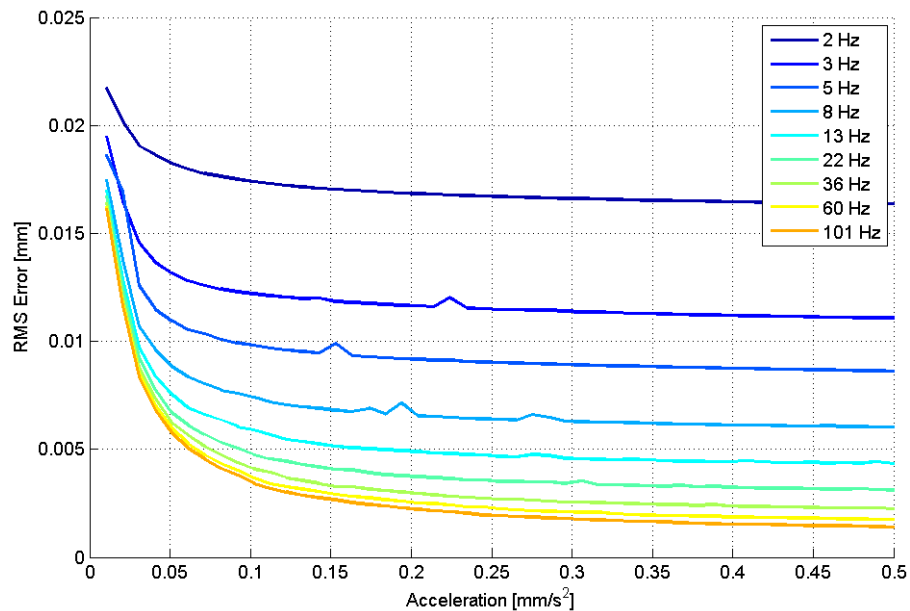
Figure 3-5: RMS motion tracking error of the AO188 tpi/tilt data, over a range of accelerations and control frequencies

These results show a leveling off in performance once the acceleration is increased past ~0.20 mm/s^2, and once the command frequency is increased past ~13 Hz; at this point the expected RMS error is 5μm (0.009" on sky). Consequently, the NGS pick-off arm stages and the translation stages of the science arms are programmed with acceleration values of 0.25 mm/s^2. The two rotation stages of the science arms are programmed with same value divided by 196mm (the nominal science arm length), to accommodate the conversion from millimeters to radians. When these values were used during simulation, the stage

velocity reached a maximum of only 0.05mm/s, indicating the stages should not reach the 1.0mm/s maximum achievable velocity typical of a PI stage.

3.3.3 TUNING CONTROLLER GAINS

The PID gain values of the C-863 controller required no additional tuning from the factory defaults recommended for each stage. The accelerations are low enough and the controller's sampling frequency is high enough that significant changes in the PID values yielded almost no difference in the stages performance. Figure 3-6 shows the commanded signal of an M-410 stage, used on an NGS pick-off arm, compared to its actual position measured using the motor's encoder.
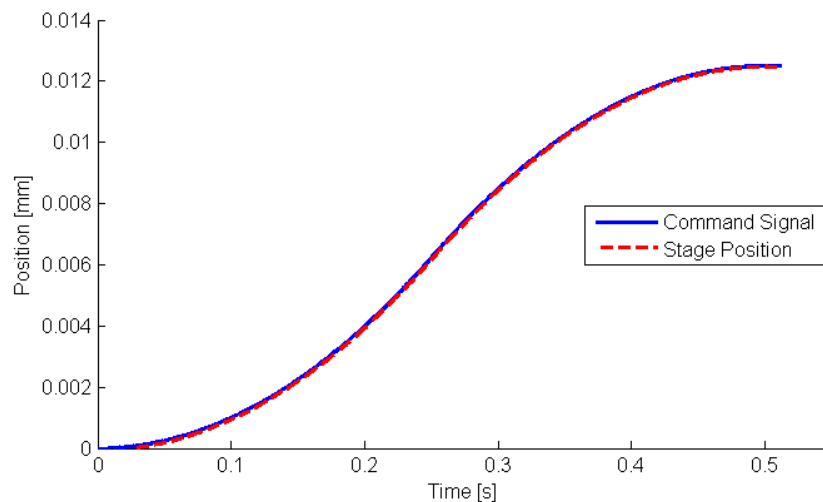
Figure 3-6: Step response of the M-410 linear stage. Acceleration values of only 0.2mm/s were used creating the gradual shape of the curve. The error between the commanded and actual position is much less than 1 micron

The data clearly shows the acceleration phase followed by the deceleration phase. The largest error between the commanded signal and measured stage position is less than a micron.

3.3.4 STAGE CONTROLLER TUNING SUMMARY

Table 3-1 summarizes the control parameters selected for the pick-off arm stages based on the results from this section.

Table 3-1: Optimized PI motor controller parameters

Parameter	Value	Units
Acceleration	0.25	mm/s^2
Deceleration	0.25	mm/s^2
Max Velocity	1.0	mm/s
Proportional Gain	800	
Integral Gain	250	
Derivative Gain	40	
Command Frequency	12.5	Hz

3.3.5 UNIDIRECTION AND BIDIRECTIONAL REPEATABILITY OF PICK-OFF ARMS

The repeatability of the pick-off arm stages needs to be measured to further understand the expected tracking error. There are two kinds of repeatability considered here: **unidirectional repeatability** is a stage's ability to repeatedly move to a commanded position when approached from the same direction, **bidirectional repeatability** is a stages ability to repeatedly move to a commanded position when approaching from either direction. The shaft mounted encoders cannot be used to measure repeatability because they do not measure the true location of the pick-off mirrors, only the motor shaft angle. Consequently the repeatability of Raven's stages was optically measured using techniques discussed in section 4.2.1. Table 3-2 shows the results.

Table 3-2: Unidirectional and bidirectional repeatability of NGS-2

Direction	Unidirectional Repeatability [μm]	Bidirectional Repeatability [μm]
+x	1.5	3.5
-x	1.0	4.0
+y	0.2	1.8
-y	1.4	1.6

The unidirectional repeatability is close to a micron. The bidirectional repeatability is expectedly larger but still less than the 5 μm error expected during tracking. The difference between the unidirectional and bidirectional repeatability is known as the **reversal value,** which is the positional error associated with changing directions. It is a combination of **backlash**, caused by small mechanical clearances within the stages

moving components, and **hysteresis**, an effect caused by the stage's motion history. The reversal value can be challenging to predict, but could be potentially be compensated if properly calibrated. The bidirectional repeatability of the y-axis is most likely better because the weight of the arm loads the mechanics of the stage, reducing backlash.

3.4 TIP-TILT PLATFORM CONTROL PARAMETER SELECTION

The TTP's objective is to offload the tip/tilt signal sent to the SDMs. Without having to compensate tip/tilt, the SDM's actuators can operate with lower stroke in a more linear region. Selecting the TTP's control parameters first requires setting notch filters to prevent resonance. Next the PI (proportional, integral) controller gain terms can be selected.

3.4.1 NOTCH FILTER SELECTION AND INTEGRAL GAIN

The TTPs internal control loop runs at 20kHz, allowing the system to react to a wide range of input signal frequencies. Some of these input frequencies will align with the mechanical resonant frequencies of the TTP and its mount, potentially causing instability. Preventing resonance requires supressing the input signal's power at the TTP's natural vibration frequencies, using a digital notch filter. Measuring these frequencies can be done by "ringing" the stage and recording the resulting signal, similar to striking a bell and listening to the tone. The platform was "struck" using its own piezo actuators and allowed to ring while its angular position was recorded with its capacitive sensors. The resulting frequency spectrum for the tilt axis of TTP-1 is shown in Figure 3-7.
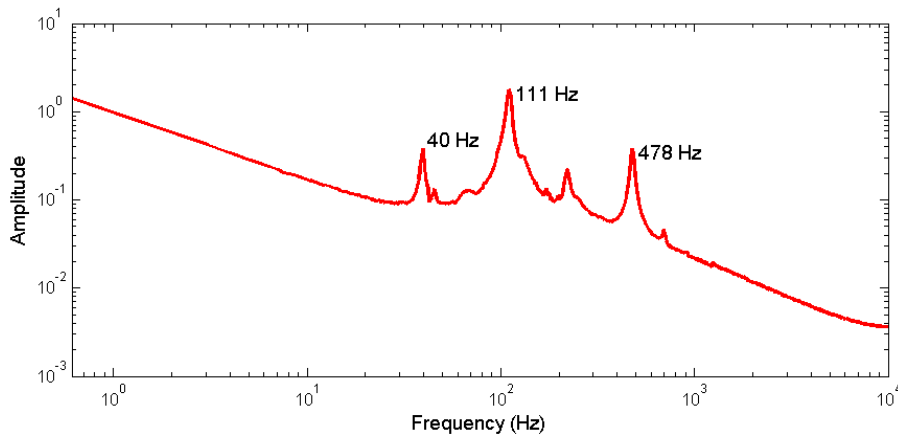
Figure 3-7: Frequency response of ringing the tilt axis of TTP-1. Resonant peaks at 40, 111 and 478Hz are clearly visible.

Three main resonant peaks are clearly visible at 40, 111 and 478 Hz. The controller used for command the TTPs (PI E-711) has two internal notch filters designed to prevent resonance, each with a 1Hz bandwidth and an attenuation of 0.05. The notch frequencies were set to the higher peaks of 111 Hz, and 478 Hz. Selecting the 40Hz signal was found to drastically reduce the TTP's overall performance.

The integral gain is automatically set by the controller upon inputting the primary notch filter. The following relation, recommended by the manufacturer[j], is used:

$$I_{TTP} = \frac{1}{4\pi(Notch\ Frequency)}$$
3-1

With the notch filters and integral gain selected, the proportional gain can be optimized.

3.4.2 PROPORTIONAL GAIN

The 150 µrad step response of each TTP axis was recorded using the platform's capacitive sensors, while using a range of proportional gain values. The results were compared, and the proportional gains were selected by attempting to reduce rise time while minimizing overshoot. Figure 3-8a shows the results for the tilt axis of TTP-1.

---

[j] It is not clear where this formula comes from. It is presented without supporting documentation in the manual for the TTP's controller. It was found that using integral gains outside this value unexpectedly lead to instability, so manual tuning was not done
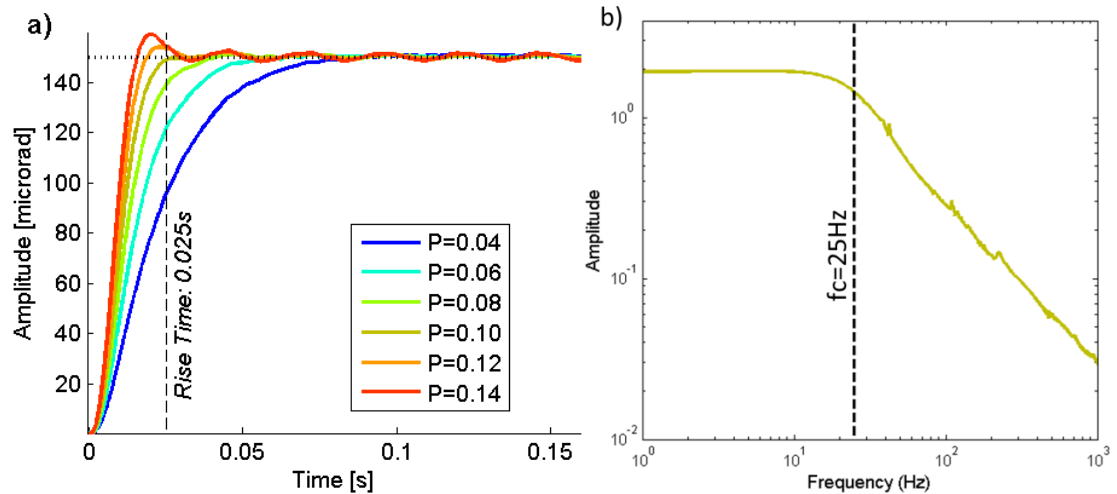
Figure 3-8: a) Step response of tilt axis of TTP-1 for proportional gain values ranging from 0.04 to 0.14. A rise time of 0.025 seconds was achieved while maintaining minimal overshoot using P=0.10. b) Fourier transform of step response for P = 0.10, showing a corner frequency of ~25Hz

A proportional gain of 0.10 (gold curve) provides the best result in terms of rise time and overshoot for this axis. Figure 3-8b shows the Fourier transform for the step response of the TTP-1 for the same axis, using all the parameters gathered in this section. It clearly shows a corner frequency of 25 Hz, indicating the servo bandwidth of the TTP. This result implies that input signals sent to the TTP of 25Hz or slower would be well tracked, while input signals 25 Hz or faster would not be well tracked. This result will be useful when a low-pass digital filter is design for the SDM/TTP offload, in Section 4.2.

3.5 SCIENCE DEFORMABLE MIRROR PARAMETER SELECTION

The science deformable mirrors operate completely in open-loop, and therefore do not require any internal parameter tuning. Essentially an unfiltered proportional controller with a unity gain is used. The calculated actuator voltages are directly applied to the actuators with no pre-processing. For safety, the DM controllers do internally "clip" the commands if they are too large or if they could collectively cause damage to the surface (e.g. two adjacent actuators set to drastically opposing voltages).

3.6 SECTION SUMMARY

The internal parameters of Raven's WFSs, science camera, motorized stages and TTPS have been selected. The SDMs require no parameter optimization as they function in both

an optical and mechanical open-loop. The parameters are selected based on the properties of an observation, previous data supplied by Subaru, and the internal working of the sensors and actuators. The next step is to combine all of these components into a common control system. Knowledge of the spatial and temporal abilities of each sensor and actuator will allow this control system to be designed much more confidently.

4 Tip/Tilt Control System Design and Calibration

Raven's control system is responsible for processing the incoming data from the WFSs, and then distributing over the SDMs, TTPs and pick-off arms. This chapter provides a detailed description of Raven's control system architecture. The design of the required digital filters and spatial transforms is also discussed. A block diagram of Raven's control system is shown in Figure 4-1.
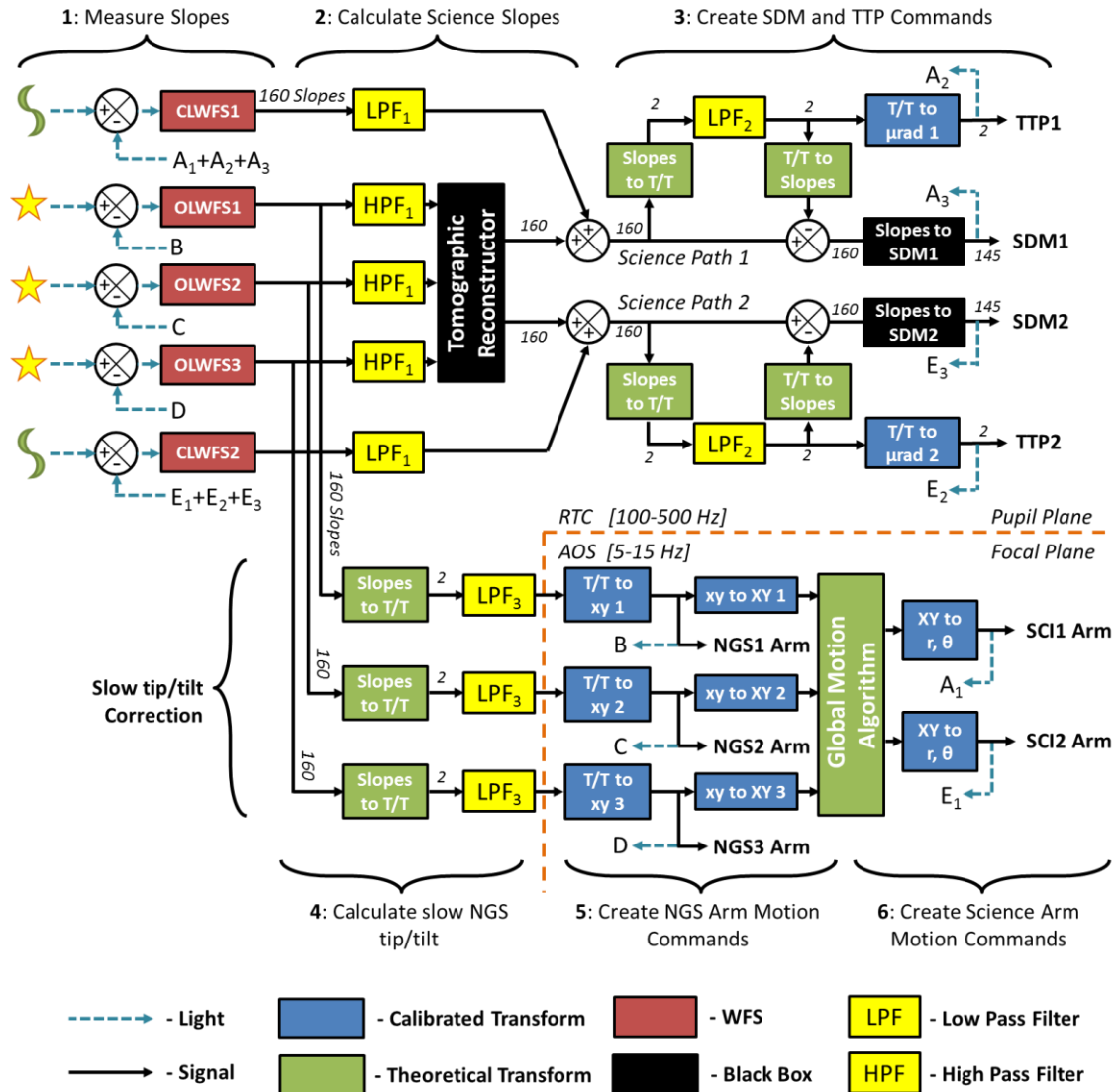
Figure 4-1: Block diagram of Raven's control system. Step 1: Open-loop and closed-loop wavefront information is gathered. Step 2: The slopes are filtered, and combined within a tomographic reconstructor to interpolate the slopes of the science targets Step 3: The tip/tilt signal is extracted, and its low frequency component is sent to the TTPs. The SDM corrects the remaining wavefront error. Step 4: The slow tip/tilt is extracted from the OLWFS slopes. Step 5: The required motion steps for the NGS arms are determined, and their absolute positions are measured. Step 6: The science arm positions are calculated and the arms are moved

With regards to the previous figure, **calibrated transforms** relate individual actuators to their corresponding sensors, **theoretical transforms** use geometric relations to extract specific information from raw data, and **digital filters** match the correct portions of the error's frequency spectrum to an actuator's servo bandwidth. For reference, a detailed description about digital filters is given in Appendix B. This chapter will describe how

each control system block is created, first theoretically based on Raven's design specifications, and then based on real data from recorded measurements.

The majority of Raven's control system is implemented in its **real-time computer** (RTC), written in the C programming language. Fundamentally, the RTC gathers the slope data from the WFSs and converts it to actuator commands for Raven's high bandwidth actuators: the SDMs and TTPs. To ensure computational efficiency, all the calculations performed within the RTC are **matrix-vector multiplications** (MVMs). Logical operations, nonlinear equations, and look-up tables, are strictly avoided within the RTC to ensure it can operate with a control frequency of up to 500Hz. The remainder of the control system is located in Raven's **adaptive optics sequencer** (AOS), written in the Matlab programming language. The AOS is designed to compensate low frequency errors (<10Hz), so the programming methods are less stringent than the RTC. The AOS creates the commands for Raven's pick-off arms using data provided by the RTC. Each step from Figure 4-1 is described in detail in the following subsections.

4.1 CALCULATING SCIENCE WAVEFRONT SLOPES (STEP 1, STEP 2)

4.1.1 THE STANDARD METHOD

The **standard method** of measuring the science target wavefronts only uses information coming from the OLWFSs. The measured slopes from the OLWFSs are combined in a tomographic reconstructor which performs the conversion. The standard method is shown in Figure 4-2. The tomographic reconstructor used in Raven is not discussed in this work[43].
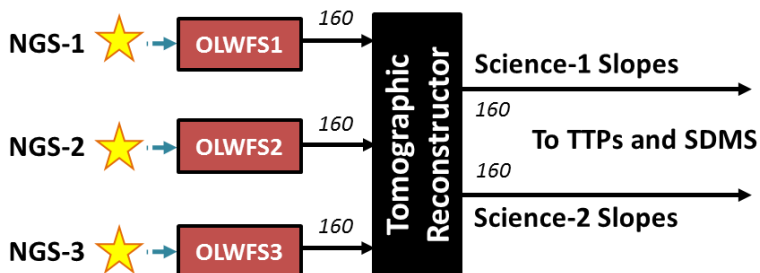
Figure 4-2: Standard method of slope acquisition, and the creation of science slopes. Each of the three OLWFS collects the 160 slopes and passes them to the tomographic reconstructor which calculates the science target slope vectors

This technique should be effective at correcting high frequency wavefront errors caused by turbulence. However, it will not be as effective in correcting slower quasi-static wavefront errors caused by insufficient calibration, or nonlinear effects like mechanical drift or thermal expansion.

4.1.2 THE HYBRID METHOD

The second slope measurement technique, the **hybrid method**, aims to eliminate quasi-static aberrations by including slope data from CLWFSs. Figure 4-3 summarizes this hybrid technique for measuring science slopes; it is a subset of Figure 4-1.
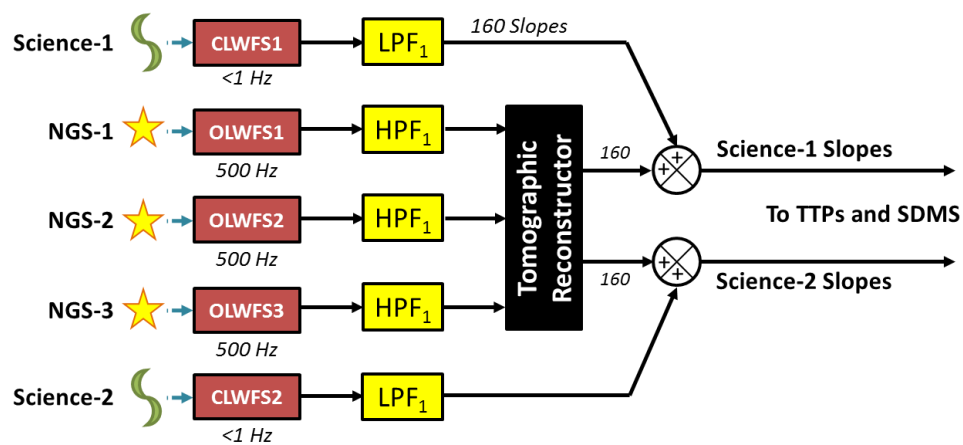
Figure 4-3: Hybrid method for slope acquisition and conversion to science slopes. The science slopes are determined by combining the high-frequency NGS slope measurements and low frequency science target slope measurements

Then hybrid method can only be used if the science targets are compact enough to produce usable spots on the CLWFS's CCD. Science targets, unlike guide stars, are typically faint, so the CLWFSs would need to run at a much slower frame rate (<1Hz) to acquire a usable signal, preventing them from being used for real-time AO correction. However, by combining the high-frequency portion of the reconstructed OLWFS slopes, with the low-frequency CLWFS slopes, a much more robust correction could be performed. By doing this, both fast aberrations from turbulence, and slow aberrations from quasi static effects, could be corrected. High-pass and low-pass filters with the same corner frequency are used to achieve the open-loop/closed-loop signal combination, commonly known as a complimentary filter. The filters would need to be designed based on the required CLWFS exposure time. This fast-open-loop/slow-closed-loop

collaboration is not a strict requirement of the MOAO architecture and will not be available during all observations. Science targets may be too dim or not compact enough to provide a reliable signal. Converting from the hybrid method to the standard fully open-loop MOAO architecture can be done by setting the corner frequency of LPF_1 to 0 (an open circuit) and setting the corner frequency of HPF_1 to the sampling frequency (a closed circuit).

If the hybrid option is available, tip/tilt compensation becomes trivial as it will be performed in closed loop. As most of the tip/tilt error sources are slow, they and would be easily measured by the CLWFSs and corrected by the TTPs or pick-off arms. However, as the hybrid method will not always be an option, and its effectiveness will not be truly known until on-sky tests are attempted, Raven's tip/tilt compensation system must be fully functional using the standard, totally open-loop, architecture discussed in the previous section.

4.2 CREATING SDM AND TTP COMMANDS (STEP 3)

The tip/tilt component of the reconstructed science wavefront needs to be **offloaded** to the TTPs, to ensure the SDMs are not required to create large tilted shapes. Figure 4-4 summarizes the offload process of one science arm; it is step 3 of Figure 4-1.
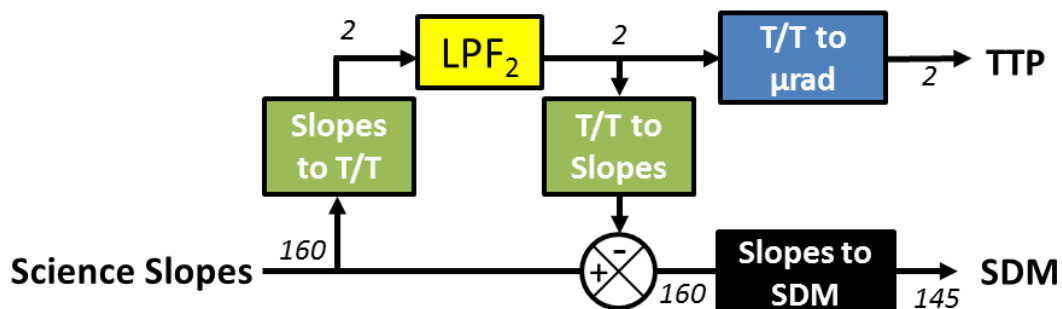
Figure 4-4: Converting science slopes to SDM and TTP commands. The tip/tilt signal is extracted from the science slopes, and the low frequencies are offloaded to the TTP. The remaining signal is sent to the SDM

The tip/tilt signal needs to be extracted from the overall slope signal using the **Slopes-to-T/T** transform. It is then low-pass filtered, using LPF_2, to attenuate the frequency components above the servo bandwidth of the TTP. The filtered signal is then sent to the

TTP, using the **T/T-to-µrad** transform. The same tip/tilt signal is then converted back to slopes, using the **T/T-to-Slopes** transform, and subtracted from the original slopes signal. The remaining wavefront slopes are multiplied by a **Slopes-to-SDM** transform, converting the slope vector to SDM voltage commands. Each of these transforms will be discussed in the following subsections.

4.2.1 EXTRACTING AND FILTERING TIP/TILT

The slopes-to-T/T transform is shown in Eqn. 4-1. Extracting a specific spatial mode from a wavefront is done by projecting the measured wavefront slopes onto the normalized theoretical slopes of the desired mode (taking the dot-product). For the RTC this has to be in the form of an MVM.

$$[\theta_x \quad \theta_y] = [S][T_{slopes \to T/T}] \qquad \textbf{4-1}$$

Where $[\theta_x \quad \theta_y]$ the amount of tip/tilt in pixels, $[S]$ is the measured slopes-vector, and $T_{slopes \to T/T}$ is the linear transform matrix responsible for the extraction. For a pure tip or tilt, the x-slopes will all be the same corresponding to the amount of tip, and the y-slopes will all be the same corresponding to the amount of tilt. Based on this information, the theoretical form of $T_{slopes \to T/T}$ is shown by Eqn. 4-2. Both column vectors are divided by the number of available slopes to normalize them.

$$[T_{slopes \to T/T}] = \begin{bmatrix} 1_1/n & 0_1 \\ \vdots & \vdots \\ 1_n/n & 0_n \\ 0_1 & 1_1/n \\ \vdots & \vdots \\ 0_n & 1_n/n \end{bmatrix}_{2n \times 2} \qquad \textbf{4-2}$$

Where n is the number of subapertures, usually 80. It can be noted that when this transform is inserted into Eqn. 4-1, the tip/tilt values are simply the average of the x-slope and y-slope measurements. This transform can be confirmed in the lab using real measurements of a tilted wavefront. Figure 4-5 shows frames from CLWFS-1 measuring a flat and purely tilted wavefront.
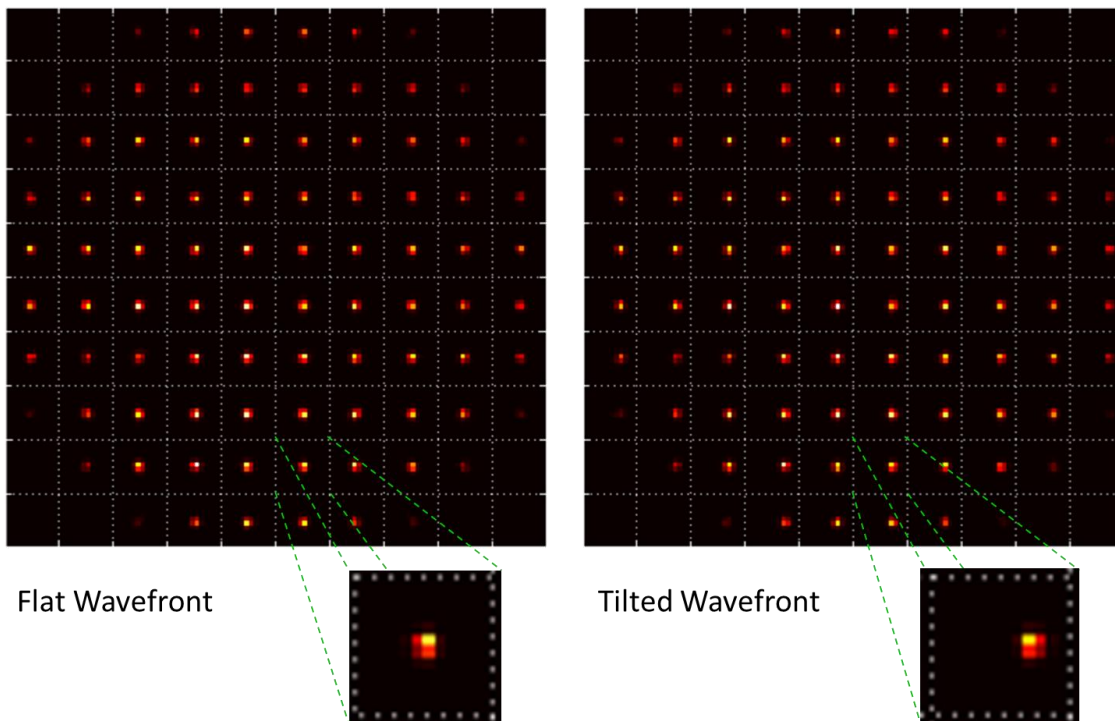
Figure 4-5: CLWFS-1 frames of a flat and purely tiled wavefront. Each spot has been shifted by an equal amount within their respective subapertures

A linearly spaced range of purely tilted wavefronts were sent into CLWFS-1, and the slopes-vectors were recorded. Figure 4-6 plots the results. The pure tilt was achieved by tilting TTP-1 with a flattened SDM.
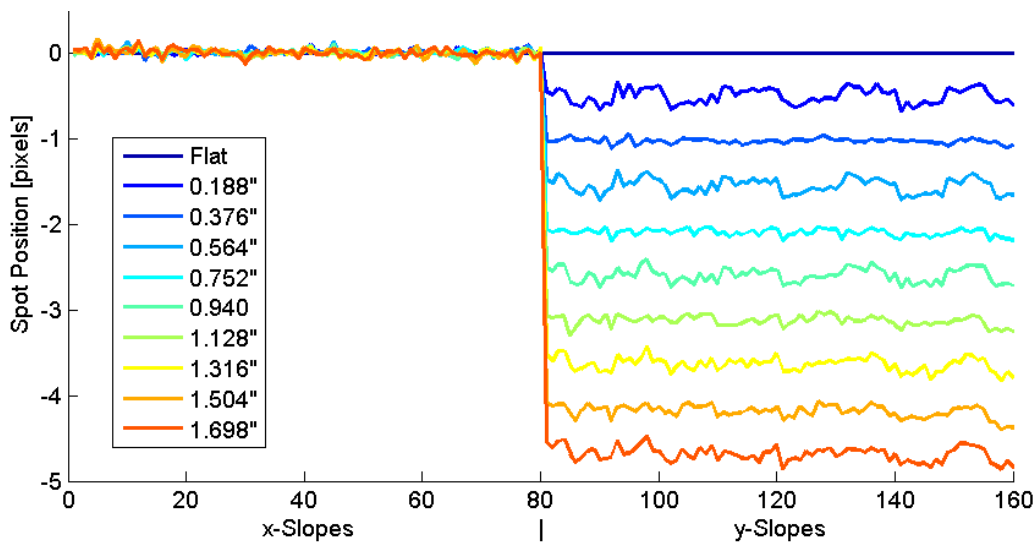
Figure 4-6: x-slope data recorded by CLWFS-1 for a range of purely titled wavefronts. The x-slopes remain relatively stationary and the y-slopes uniformly increase. The values are flattest near integer pixel values

The tilted y-slopes all have a standard deviation of less than 0.1 pixels and the pattern stays consistent up to 4.5 pixels of tilt (1.8"). Figure 4-7 shows the results of extracting the tip/tilt from the previous data, using Eqns. 4-1 and 4-2.
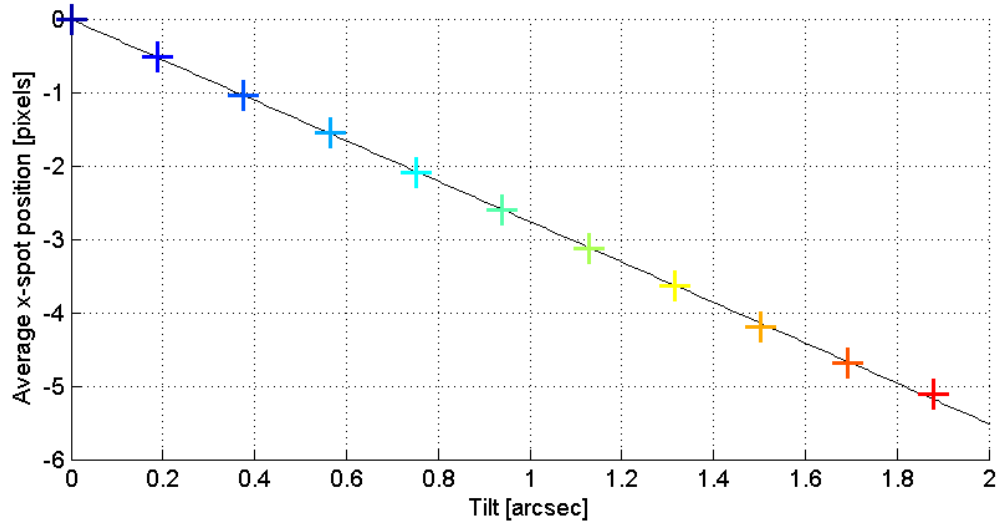
Figure 4-7: Average of y-slope positions for purely tilted wavefronts. The data closely follows a linear trend line

The high linearity of this chart, and the small standard deviation of the tilted slope readings, indicate that using a linear transform to extract tip/tilt from the wavefront slope measurements will be acceptable. Using a transform that is a function of tilt would yield more accurate measurements but would not be compatible with the RTC.

The tip/tilt error of a science target can now be measured. This signal needs to be low-pass-filtered, to attenuate the frequencies higher than the servo bandwidth of the TTP; previously measured to be 25Hz. The filter used is a second-order, low-pass Butterworth filter, with a cut-off frequency of 20Hz. The filter coefficients are created by Matlab, based on the RTC's current command frequency. If the RTC's sampling frequency changes, the filter coefficients would need to be recalculated.

4.2.2 CREATING TIP/TILT PLATFORM COMMANDS

The portion of tip/tilt to be corrected by the TTPs needs to be converted to µrads from pixels before the signal can be sent to the TTP's controller. It does this using the transform shown in Eqn. 4-3.

$$\begin{bmatrix} \phi_x \\ \phi_y \end{bmatrix}_{\mu rads} = \begin{bmatrix} T_{T/T \to \mu rad} \end{bmatrix} \begin{bmatrix} \theta_x \\ \theta_y \end{bmatrix}_{Pixels}$$

4-3

Where ϕ_x and ϕ_y are the tip/tilt commands in radians, θ_x and θ_y are the tip/tilt signals in pixels, and $T_{T/T \to \mu rad}$ is the conversion transform. The $T_{T/T \to \mu rad}$ transform can be derived using Raven's design parameters:

$$\begin{bmatrix} T_{T/T \to \mu rad} \end{bmatrix} = \left(\frac{1}{2}\right)\left(1.84\frac{\mu rad}{pixel}\right)\left(\frac{8m}{0.025m}\right)_{Mag}\begin{bmatrix} 1 & 0 \\ 0 & 1 \end{bmatrix} = \begin{bmatrix} 294.4 & 0 \\ 0 & 294.4 \end{bmatrix}\mu rad/pixel$$

The ½ term is included because the reflected ray's angle shifts by twice the amount of mirror tilt. The next term is the pixel scale of Raven's WFSs[k]. The final term accounts for the system magnification, computed as the ratio between Subaru's primary mirror diameter (8m) and the SDM pupil diameter (25mm).

The $T_{T/T \to \mu rad}$ transform can alternatively be calibrated using measurements from the instrument. Doing this requires tipping and tilting the TTP to two unique angles, (ϕ_{x1}, ϕ_{y1}) and (ϕ_{x2}, ϕ_{y2}), and recording the tip/tilt at each position using the arm's CLWFS slope measurements. By rearranging Eqn. 4-3, $T_{T/T \to \mu rad}$ can be measured directly using Eqn. 4-4

$$\begin{bmatrix} T_{T/T \to \mu rad} \end{bmatrix}_N = \begin{bmatrix} \phi_{x1} & \phi_{x2} \\ \phi_{y1} & \phi_{y2} \end{bmatrix}_N \begin{bmatrix} \theta_{x1} & \theta_{x2} \\ \theta_{y1} & \theta_{y2} \end{bmatrix}_N^{-1}$$

4-4

Where N refers to which TTP is being calibrated. This technique was used with commanded signals of (150, 0) µrads and (0, 150) µrads as the input signal. Transforms were calculated using these values, and the corresponding tip/tilt measurements extracted from the CLWFSs slope measurements. The resulting calibrated $T_{T/T \to \mu rad}$ transforms are shown in Table 4-1.

---

[k] This value is usually written in more astronomical units, as 0.38"/pixel

Table 4-1: Calibrated TTP transforms used for converting tip/tilt to µrads

	TTP-1	TTP-2
$[T_{T/T \to \mu rad}]$	$\begin{bmatrix} -1.7 & 323.7 \\ -325.1 & -4.1 \end{bmatrix}_1$	$\begin{bmatrix} 2.1 & -286.5 \\ 308.6 & -9.3 \end{bmatrix}_2$

These matrices are within 10% of those predicted theoretically. Each term's sign and location within the transform is based on the platform's internal directional conventions. The smaller terms within each transform are most likely due to slight rotational misalignment between the TTP's actuators and the CLWFS's pixel grid. The calibrated $T_{T/T \to \mu rad}$ transform will be used as it represents the actual system making it more accurate.

As there is no optical feedback, the amount of tip/tilt sent to the TTP needs to be digitally removed from the total wavefront error signal sent to the SDM. This is done by converting it back to slopes using Eqn. 4-5, and subtracting it from the original measurements, Eqn. 4-6. The transform used in Eqn. 4-5 is simply the pseudo inverse of the Slopes-to-T/T transform.

$$[S_{TTP}]_{1 \times 160} = [\phi_x \quad \phi_y] \begin{bmatrix} 1 & \cdots & 1 & 0 & \cdots & 0 \\ 0 & \cdots & 0 & 1 & \cdots & 1 \end{bmatrix}_{2 \times 160} \qquad \textbf{4-5}$$

$$S_{REM} = S_{TOT} - S_{TTP} \qquad \textbf{4-6}$$

The remaining slope signal, S_{REM}, is converted to SDM actuator commands using the slopes-to-SDM transform.

4.2.3 CREATING SDM COMMANDS

The SDM requires a column vector of 145 commands. The commands need to be calculated from the 160 slope measurements for each science target. The conversion from slopes to voltages requires the $T_{slopes \to SDM}$ transform, commonly referred to as the **command matrix**. For Raven, the command matrices are [145x160] in size, which is much larger than the transforms used during tip/tilt correction. Consequently these matrices have substantial structure, and their formation is non-trivial. A detailed

discussion of the techniques used formulate them is outside the scope of this work; however, a brief overview will be presented with emphasis on tip/tilt compensation. The simplest way to create a command matrix utilizes the following steps:

1. Light from a CU source is acquired by a science pick-off arm, creating an array of wavefront spots on its corresponding CLWFS.

2. Each actuator of the SDM is pushed and pulled, using known voltages, in a predefined sequence. The resulting wavefront slope measurements are recorded using the CLWFS after each actuation.

3. The recorded data is used to populate the **interaction matrix**, which is [160x145] in size, and represents the influence actuator voltage commands have on the corresponding wavefront slopes.

4. The interaction matrix is pseudo-inverted to create the command matrix, which represents the relationship between wavefront sensor slopes and the corresponding actuator voltage commands

Figure 4-8 shows the interaction and command matrices from a calibration of SDM1.
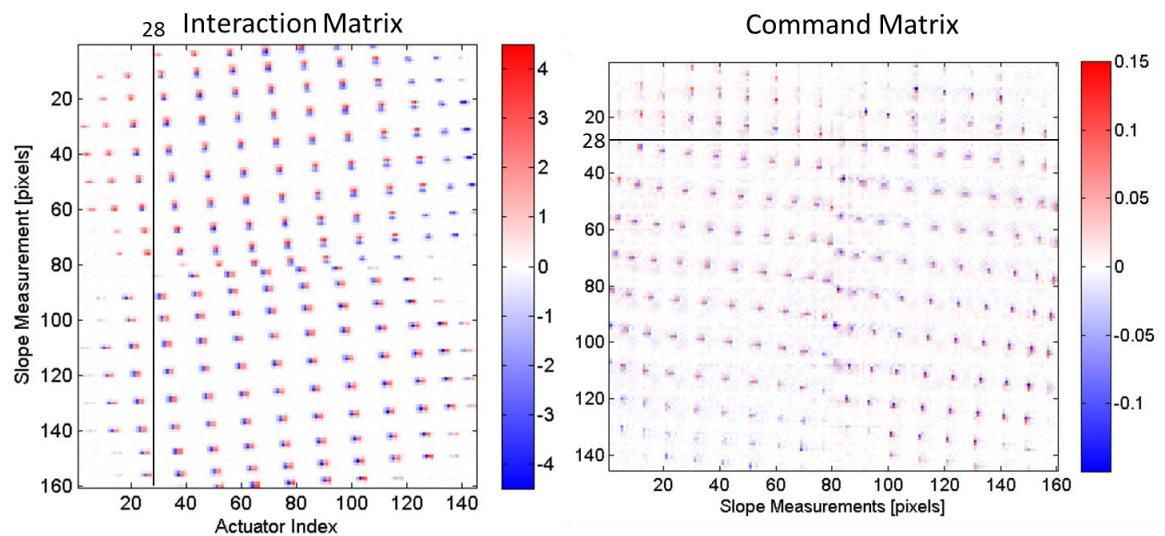
Figure 4-8: Interaction matrix and command matrix of SDM1. The slopes from actuator 28 are indicated by the black vertical line in the interaction matrix to highlight its lack of influence

When considering the SDMs' ability to compensate tip/tilt errors, the actuators around the periphery become more critical. As a tilted shape is highest and lowest on the edges, the outer actuators will be most useful for creating it. On Raven, the SDMs' outermost actuators are outside the beam footprint (see Figure 2-18). As light will not be reflected off the sections of the mirror containing these actuators, their influence will not be well measured by the CLWFS during calibration, and their potential contribution will not be represented in the interaction matrix or command matrix. Actuator 28 (an outer actuator), is shown as a vertical line on the interaction matrix of the previous figure to highlight its lack influence.

The actuator voltage maps for purely tipped or tilted shapes can be calculated by multiplying the command matrix by a tipped or tilted slopes-vector. The results of doing this are shown in Figure 4-9.
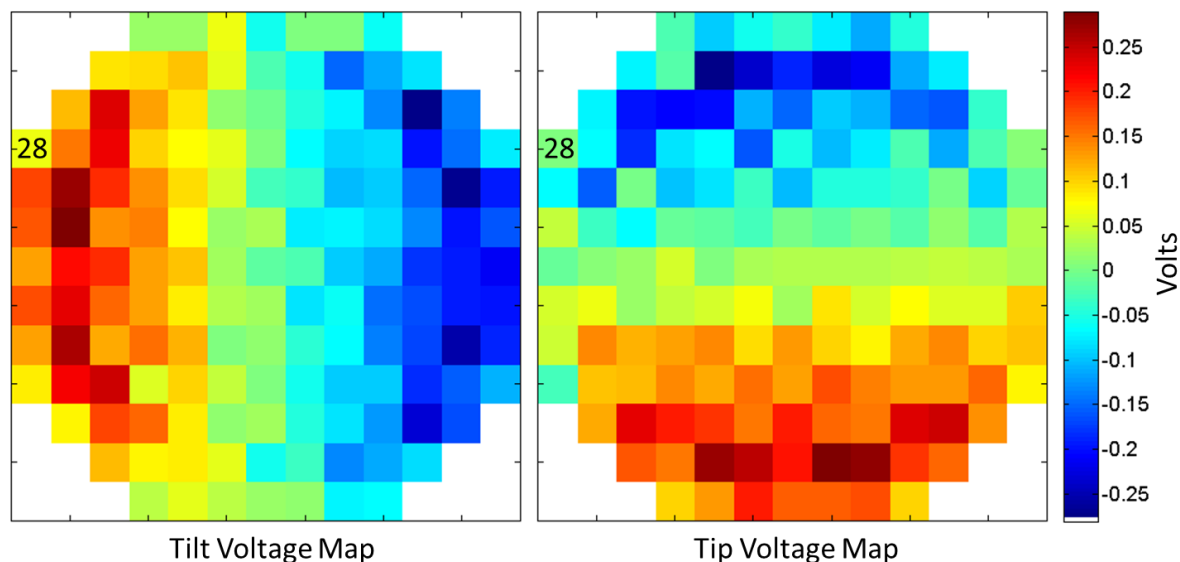
Figure 4-9: SDM1 actuator voltages to create a purely tilted wavefront using the command matrix and tilted slope vectors. The outer actuators do not follow the trend of the interior actuators because their influence was not represented in the interaction matrix

As expected, the voltage maps appear as tilted flat planes. However, it can be seen that the outer actuators do not follow the trend of the interior actuators. Actuator 28 is again labelled to show this. A more involved calibration technique is required to properly include the abilities of the outer actuators.

At this point the design of Raven's high-frequency tip/tilt compensation control system is complete. The low-frequency compensation system is discussed in the following section.

4.3 Low Frequency Tip/Tilt Compensation

In addition to fast atmospheric tip/tilt, Raven's guide stars and science targets will experience slow tip/tilt errors from field rotation, DAR, and telescope tracking error (See section 1.11). It has been shown that tip/tilt errors correspond to linear motions in the focal plane, where the pick-off arms are located. Consequently, during an observation, Raven's pick-off arms are utilized to track their respective target's slow tip/tilt. It does so using the following steps:

1. The tip/tilt error from each OLWFS is low pass filtered within the RTC and sent to the AOS.

2. The slow tip/tilt is converted to positional shifts in the focal plane, so the NGS pick-off arm stages can be moved accordingly to keep them centered.

3. The NGS pick-off arm stage commands are converted to global motions within the focal plane. The global NGS positions are then used to calculate the global science target positions using a global motion algorithm.

4. The global science target positions are converted to local stage commands and the stages of the science pick-off arms are moved accordingly.

Figure 4-10 shows steps 1 and 2 of this process, which is fundamentally the same as the process described in Figure 1-14c. For clarity, a simplified WFS is shown with a 3x3 lenslet array.
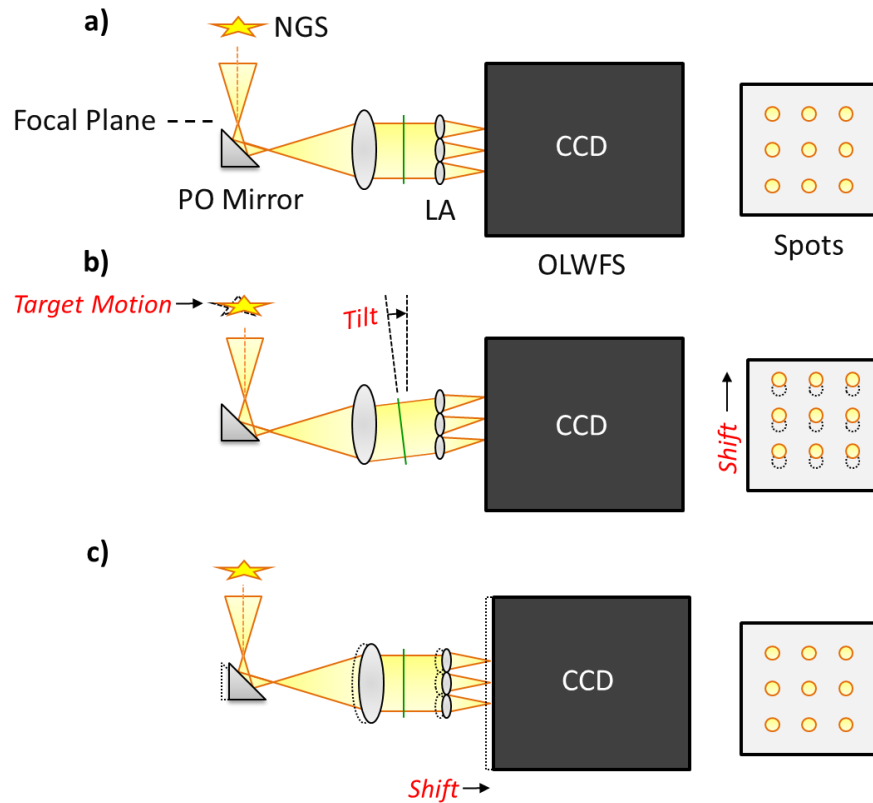
Figure 4-10: Example of OLWFS target tracking. a) The pick-off mirror and OLWFS is centered on the NGS, and the spots are centered. b) A shift in the NGS's position causes a tilted wavefront at the lenslet array, resulting in globally shifted spots on the CCD c) The entire OLWFS is moved to match the motion of the NGS and re-center the spots.

This method is applicable for both x and y NGS motions. The motion of the science targets will not be observable by CLWFSs, so their positional shifts must be inferred from the NGSs. Sections 4.4 discusses the methods used for tracking the NGS targets, and section 4.5 discusses the methods used for tracking the science targets. As the NGS pick-off arms will be moving along with the science pick-off arms, no communication is required between the slow tip/tilt compensation system and fast tip/tilt compensation system.

4.4 TRACKING SLOW NGS MOTIONS WITH PICK-OFF ARMS (STEP 4, STEP 5)

Tracking the NGS motions with the NGS pick-off arms requires first measuring the amount of source motion, in the form of tip/tilt, filtering the signal to extract its low

frequency component, and then finally converting the tip/tilt to stage commands. This process is summarized Figure 4-11, it represents steps 4 and 5 of Figure 4-1.
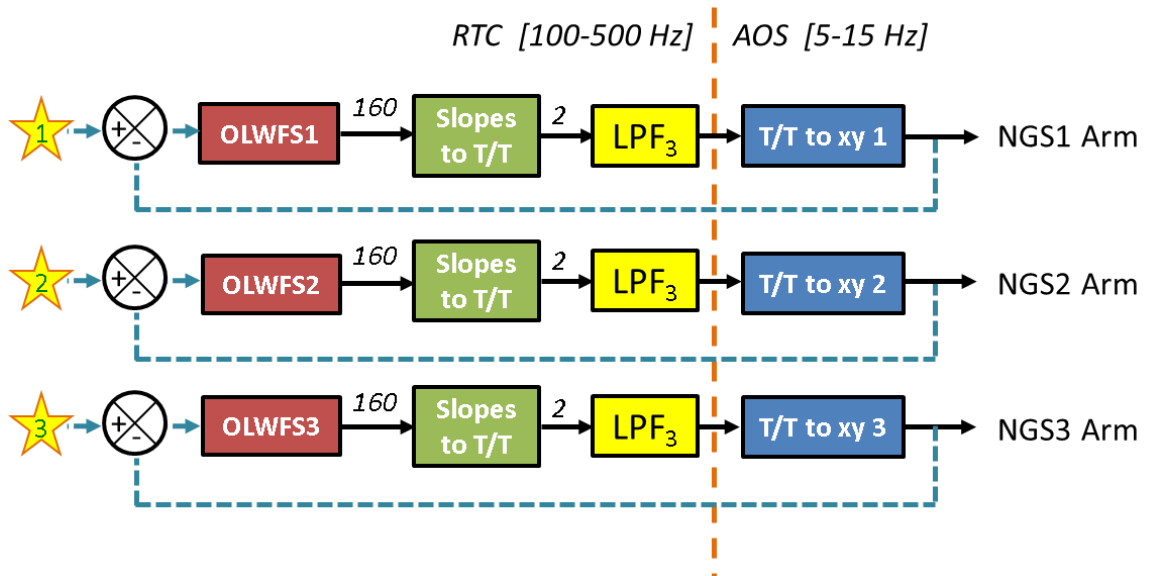
Figure 4-11: Slow NGS motion tracking control system. Slope vectors are measured from the OLWFSs and their tip/tilt component is calculated and low-pass filtered. The slow tip/tilt is then converted to NGS arm motion commands to keep their targets centered. The control loop is optically closed (light shown as a blue dashed line)

The raw slope signals from the OLWFSs are also used for the slow tip/tilt correction control system, in addition to being sent to the tomographic reconstructor. The slopes from each OLWFS are first converted to tip/tilt using the $T_{slopes \to T/T}$ transform described by Eqn. 4-1. The tip/tilt signal is then low-pass-filtered to extract low frequency errors, and reduce the effects noise. As discussed in section 3.3.4, a command frequency of 12.5 Hz will be used to control the stage positions, so a second order low-pass Butterworth filter, with a cut-off frequency of 20Hz, was implemented. The slow NGS tip/tilt error signals are then pushed to the AOS from the RTC, where they are subsequently transformed to the x-y stage commands required for the NGS pick-off arms to track their NGS's motions. This transform is described by Eqn. 4-7.

$$\begin{bmatrix} \Delta x \\ \Delta y \end{bmatrix} = \begin{bmatrix} T_{T/T \to xy} \end{bmatrix} \begin{bmatrix} \theta_x \\ \theta_y \end{bmatrix} \qquad \qquad \textbf{4-7}$$

Where Δx and Δy represent the local stage position shifts in *mm*, θ_x and θ_y are the measured tip and tilt in *pixels*, and $T_{T/T \to xy}$ is the linear transform required for the conversion. The $T_{T/T \to xy}$ transform can be determined using Raven's design parameters:

$$\left[T_{T/T \to xy}\right]_N = (0.533 \text{ mm/''})(0.38 \text{ ''/} pixel)R(\phi_{Arm})_N R(\phi_{CCD})_N \qquad \textbf{4-8}$$

$$R(\phi_{Arm}) = \begin{bmatrix} \cos\phi_{Arm} & -\sin\phi_{Arm} \\ \sin\phi_{Arm} & \cos\phi_{Arm} \end{bmatrix}, R(\phi_{CCD}) = \begin{bmatrix} \cos\phi_{CCD} & -\sin\phi_{CCD} \\ \sin\phi_{CCD} & \cos\phi_{CCD} \end{bmatrix}$$

The initial term is the plate scale of the Subaru telescope, followed by the pixel scale of the WFSs. The two rotation matrices are defined by: ϕ_{Arm} which represents the angle between the WFS arm and horizontal plane (see Figure 2-10), and ϕ_{CCD} which represents the rotation of camera's CCD about its optical axis (usually a multiple of 90°). Using Eqn. 4-8, the calculated transforms are:

Table 4-2: Calculated transforms to convert measured NGS tip/tilt to stage commands

Arm	Rotation Angle	$\left[T_{T/T \to xy}\right]_{N,Calc}$
OLWFS-1	$\phi_{Arm1} = 140°, \phi_{CCD1} = 270°$	$\begin{bmatrix} 0.130 & -0.155 \\ 0.155 & 0.130 \end{bmatrix}_1$
OLWFS-2	$\phi_{Arm2} = 270°, \phi_{CCD2} = 270°$	$\begin{bmatrix} -0.202 & 0 \\ 0 & -0.202 \end{bmatrix}_2$
OLWFS-3	$\phi_{Arm3} = 40°, \phi_{CCD3} = 90°$	$\begin{bmatrix} -0.130 & -0.155 \\ 0.155 & -0.130 \end{bmatrix}_3$

To reduce potential confusion, it would be ideal for all of the $T_{T/T \to xy}$ matrices to be equivalent. This could be done by rotating the CCDs to counteract the rotation imparted by the arm angle. This was not done on Raven, primarily because of the additional complexity required to mount the OLWFS cameras in a rotated configuration.

The second method to formulate $T_{/TT \to xy}$ is through system calibration, using system measurements. The same technique for calibrating $T_{T/T \to \mu rad}$ from section 4.2.2 can be implemented for this. By shifting an arm's x-y position by two known amounts, and

recording the subsequent changes in tip/tilt, the $T_{T/T \to xy}$ transform can be directly measured by rearranging Eqn. 4-8, into Eqn. 4-9.

$$\left[T_{TT \to xy}\right]_N = \begin{bmatrix} \Delta x_1 & \Delta x_2 \\ \Delta y_1 & \Delta y_2 \end{bmatrix}_N \begin{bmatrix} \theta_{x1} & \theta_{x2} \\ \theta_{y1} & \theta_{y2} \end{bmatrix}_N^{-1} \qquad \textbf{4-9}$$

Where N is the index of an NGS arm, and the subscripts 1 and 2 represent which motion step was being measured. Using the relative position shifts of positions: ($x_1 = 0.2, y_1 = 0$) and ($x_2 = 0, y_2 = 0.2$), the following results were obtained for NGS arms. The calculated transforms from Table 4-2 are shown for comparison.

Table 4-3: Calibrated transforms to convert measured NGS tip/tilt to stage commands

Arm	$\left[T_{T/T \to xy}\right]_{N,Measured}$	$\left[T_{T/T \to xy}\right]_{N,Calculated}$
NGS-1	$\begin{bmatrix} 0.134 & -0.155 \\ 0.149 & 0.129 \end{bmatrix}_1$	$\begin{bmatrix} 0.130 & -0.155 \\ 0.155 & 0.130 \end{bmatrix}_1$
NGS-2	$\begin{bmatrix} -0.202 & -0.001 \\ 0.001 & -0.203 \end{bmatrix}_2$	$\begin{bmatrix} -0.202 & 0 \\ 0 & -0.202 \end{bmatrix}_2$
NGS-3	$\begin{bmatrix} -0.125 & -0.160 \\ 0.163 & -0.126 \end{bmatrix}_3$	$\begin{bmatrix} -0.130 & -0.155 \\ 0.155 & -0.130 \end{bmatrix}_3$

The small differences between the calculated and measured values for $T_{T/T \to xy}$ are most easily explained by optical misalignments within the OLWFSs, and mechanical misalignments of the x-y stages. The measured matrices inherently include these misalignments, and subsequently provide a more accurate relationship between measured tip/tilt error and relative stage motion. With these transforms created, all of the blocks from Figure 4-11 have been determined, and the NGS pick-off arms can now track the motions of their NGS. The NGS tracking system is the only part of Raven that will always operate in an optically closed loop.

4.5 CREATING SCIENCE ARM MOTION COMMANDS (STEP 6)

Assuming there is no optical feedback from the CLWFSs, the science target's slow tip/tilt will need to be tracked in open loop using the science arms. This requires inferring

the science pick-off arm stage commands from the NGS pick-off arm stage commands. Figure 4-12 illustrates this process; it is step 6 from Figure 4-1.
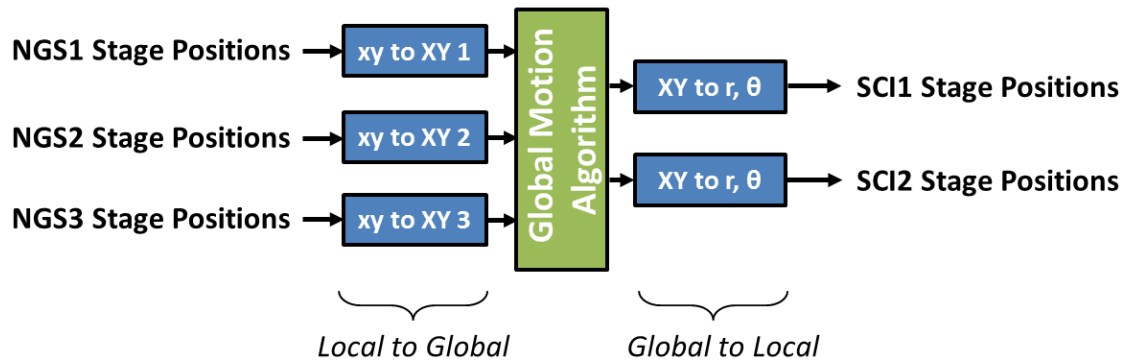
Figure 4-12: Creating science arm stage commands from NGS arm positions. The (x, y) NGS arm positions are converted to a global reference frame. The global co-ordinates are converted to science global positions using a global motion algorithm. Finally the global science positions are converted to (r, θ) stage commands

First, the global locations of the three NGS need to be extracted from the NGS pick-off arm stage positions, using the $T_{xy \to XY}$ transform. These locations are then used to determine the global science target locations using a **global motion algorithm**. Finally the global science target locations are transformed to local stage commands for the science arms using additional transforms.

4.5.1 DEFINITION OF THE FOCAL PLANE GLOBAL CO-ORDINATE SYSTEM

The CU source grid was chosen to define Raven's focal plane global co-ordinate system. It can be readily accessed by all the pick-off arms, and is part of the baseline system design. A 2-dimensional Cartesian co-ordinate system requires three known points to be fully constrained: an origin point, and two exterior points to define the direction and scale of the axes. The location of central seeing limited CU source (19) is used as the origin, while sources 6 and 17, which respectively lie on the vertical and horizontal axes of the source grid, are used as the other two reference points. Positive *Y* is defined as opposing gravity. Positive *X* is defined as to the right when looking towards the telescope from Raven's perspective.
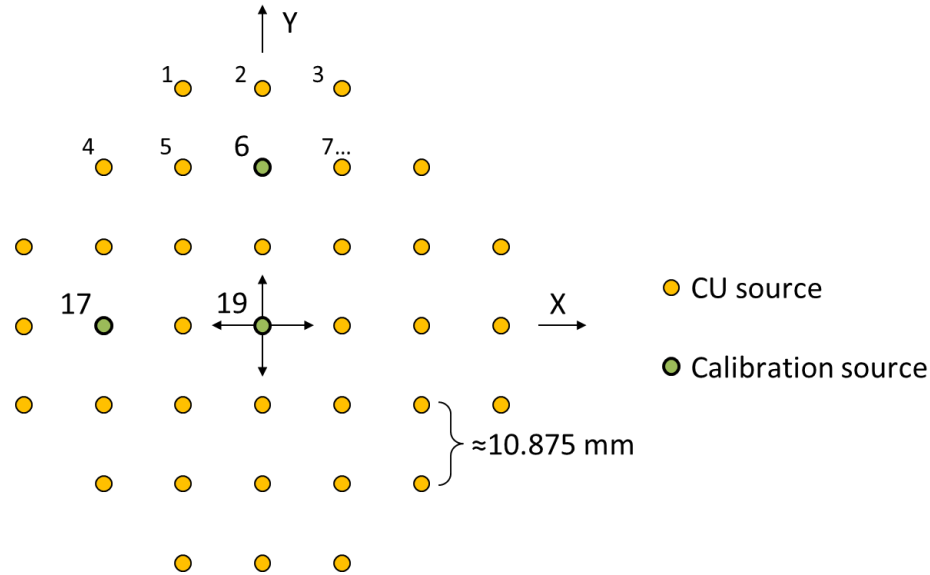
Figure 4-13: Definition of the focal-plane global co-ordinate system used on Raven, referenced to the source grid created by the CU. Source 19 defines the origin. The global *X* direction is along the vector between sources 19 and 17, and the global *Y* direction is along the vector between sources 19 and 6.

The absolute global positions of sources 6, 17 and 19 are defined as their designed positions[1]:

Table 4-4: Global Co-ordinate Definition Sources

Source #	6	17	19
$[X \quad Y]$ mm	$[0 \quad 21.75]$	$[-21.75 \quad 0]$	$[0 \quad 0]$

At this point a "master" NGS pick-off arm can be moved to these points, and an initial $T_{xy \to XY}$ transform can be created between the local stage coordinates and the global coordinate system.

4.5.2 MASTER NGS ARM CALIBRATION AND SOURCE MEASUREMENT

The linear transform used for converting an NGS pick-off arm's stage commands to global locations is shown in Eqn. 4-10. For clarity, an arm's individual stage positions are denoted by lower-case letters: (x, y) or (r, θ), while a targets location within the global co-ordinate frame is denoted by upper-case letters: X, Y.

---

[1] These values are not expected to be physically exact, as the actual position of the sources will be shifted by lens distortion within the CU. This is not relevant because the values will still establish a co-ordinate system

$$\begin{bmatrix} X \\ Y \end{bmatrix}_n = [T_{xy \to XY}]_n \begin{bmatrix} x - x_0 \\ y - y_0 \end{bmatrix}_n$$

4-10

Where x and y represent the stage positions of NGS pick-off arm-n , and X and Y represent the global position of the NGS. The x_0 and y_0 terms represent the offset between the local and global coordinate systems, and $T_{xy \to XY}$ is a linear geometric transform that account for any scaling or rotation. If everything was manufactured and assembled perfectly, the $T_{xy \to XY}$ transform should be an identity matrix.

NGS arm-1 was selected as the master arm, and was subsequently used to create the global co-ordinate system[m]. The calibration procedure requires moving it to the three reference sources (6, 17 and 19), centering it to compensate any tip/tilt error, then recording the arm's stage positions. Figure 4-14 illustrates this process.

| Measure Source 17 | Measure Source 6 | Measure Source 19 |
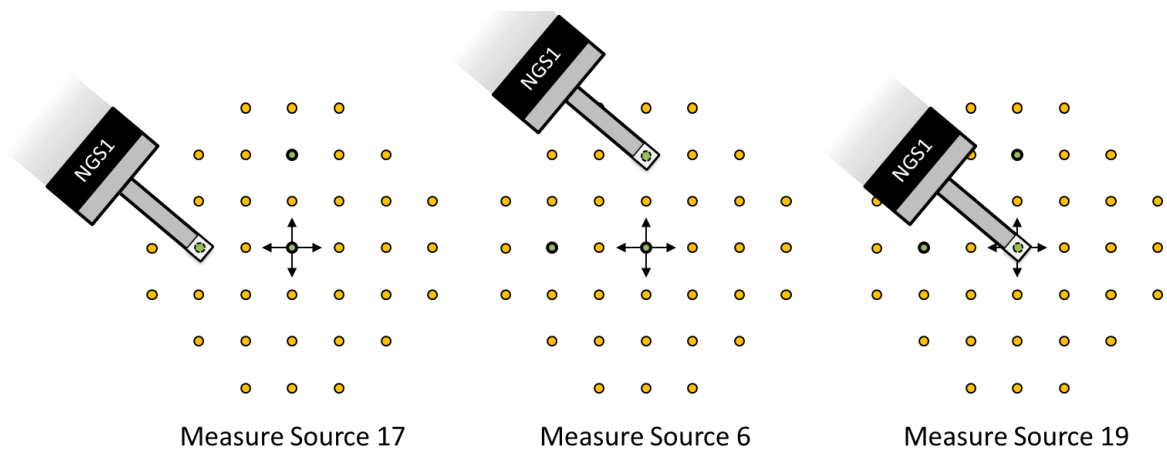
Figure 4-14: Master arm calibration. OLWFS1 moves to sources 17, 6 and 19. At each point the arm centers itself on the source and records its local xy stage positions.

Combining the measured xy stage positions with the previously defined XY source locations into Eqn. 4-10, leads to the following three relations:

$$\begin{bmatrix} X_{17} \\ Y_{17} \end{bmatrix}_1 = [T_{xy \to XY}]_1 \begin{bmatrix} x_{17} - x_0 \\ y_{17} - y_0 \end{bmatrix}_1$$

4-11a

---

[m] NGS arm-2 could not access the top 3 sources and NGS arm-1 behaves better than NGS arm-3

$$\begin{bmatrix} X_6 \\ Y_6 \end{bmatrix}_1 = [T_{xy \to XY}]_1 \begin{bmatrix} x_6 - x_0 \\ y_6 - y_0 \end{bmatrix}_1 \qquad \textbf{4-11b}$$

$$\begin{bmatrix} X_{19} \\ Y_{19} \end{bmatrix}_1 = [T_{xy \to XY}]_1 \begin{bmatrix} x_{19} - x_0 \\ y_{19} - y_0 \end{bmatrix}_1 \qquad \textbf{4-11c}$$

From these three relations the offset terms and $T_{xy \to XY}$ can be calculated. Doing this first requires cancelling the offset terms by subtracting Eqn. 4-11c from 4-11a and 4-11b, yeilding the following equations:

$$\begin{bmatrix} X_6 - X_{19} \\ Y_6 - Y_{19} \end{bmatrix}_1 = [T_{xy \to XY}]_1 \begin{bmatrix} x_6 - x_{19} \\ y_6 - y_{19} \end{bmatrix}_1 \qquad \textbf{4-12a}$$

$$\begin{bmatrix} X_{17} - X_{19} \\ Y_{17} - Y_{19} \end{bmatrix}_1 = [T_{xy \to XY}]_1 \begin{bmatrix} x_{17} - x_{19} \\ y_{17} - y_{19} \end{bmatrix}_1 \qquad \textbf{4-12b}$$

These equations are then combined into Eqn. 4-13a, and then rearranged to determine the linear transform in Eqn. 4-13b.

$$\begin{bmatrix} X_6 - X_{19} & X_{17} - X_{19} \\ Y_6 - Y_{19} & Y_{17} - Y_{19} \end{bmatrix} = [T_{xy \to XY}]_1 \begin{bmatrix} x_6 - x_{19} & x_{17} - x_{19} \\ y_6 - y_{19} & y_{17} - y_{19} \end{bmatrix} \qquad \textbf{4-13a}$$

$$[T_{xy-XY}]_1 = \begin{bmatrix} X_6 - X_{19} & X_{17} - X_{19} \\ Y_6 - Y_{19} & Y_{17} - Y_{19} \end{bmatrix} \begin{bmatrix} x_6 - x_{19} & x_{17} - x_{19} \\ y_6 - y_{19} & y_{17} - y_{19} \end{bmatrix}^{-1} \qquad \textbf{4-13b}$$

With T_{xy-XY} now known, any of the variants of Eqn. 4-11 can be rearranged to determine the offset terms which were cancelled earlier:

$$\begin{bmatrix} x_0 \\ y_0 \end{bmatrix} = \begin{bmatrix} x_6 \\ y_6 \end{bmatrix} - [T_{xy \to XY}]_1^{-1} \begin{bmatrix} X_6 \\ Y_6 \end{bmatrix} \qquad \textbf{4-14}$$

The transform matrix and offset for NGS arm-1 were measured using this technique, and the results are shown below in Table 4-5.

Table 4-5: Master Arm Calibration Values

Master Transform	Master Offset [mm]
$[T_{xy \to XY}]_1 = \begin{bmatrix} -1.0039 & -0.0011 \\ 0.0033 & 1.0042 \end{bmatrix}$	$\begin{bmatrix} x_0 \\ y_0 \end{bmatrix}_1 = \begin{bmatrix} 42.4591 \\ 44.8111 \end{bmatrix}$

As expected, the linear transform looks similar to an identity matrix, with some subtle variations, and sign changes. To give context to the values within the transform, it can be compared to the generic geometric transform shown in Eqn. 4-15.

$$[T_{xy \to XY}] = \begin{bmatrix} 1 & 0 \\ 0 & 1 \end{bmatrix} \times \begin{bmatrix} s_x & 0 \\ 0 & s_y \end{bmatrix}_{Scale} \times \begin{bmatrix} 1 & \beta \\ \alpha & 1 \end{bmatrix}_{Shear} \cong \begin{bmatrix} s_x & \beta \\ \alpha & s_y \end{bmatrix} \qquad \textbf{4-15}$$

In this formula, s_x and s_y are scaling terms for each axis, which should be close to unity as both the local and global systems are defined in millimetres. The α and β terms represent shear, equivalent to an angular misalignment between the local stage axes and global axes. The shear terms should be small as the axes were designed to be along the same directions. Comparing the result from Table 4-5 with Eqn. 4-15, it can be seen that the linear transform for the master arm has a ~0.4% scaling on each axis, implying the source grid has been slightly optically distorted by the CU. The negative sign of the first term of $T_{xy \to XY}$ implies the stage x-axis and global x-axis are in opposing direction. Finally, the shear terms imply the x and y stage axes are angularly misaligned by 0.0033 and -0.0011 radians (0.18° and 0.07°). The offset term is simply the difference between the stage positions at source 19 and their respective internal reference switches.

With NGS arm-1 now properly calibrated as the master arm, it was used to measure the global positions of the remaining 34 seeing limited CU sources. Figure 4-15 shows the resulting locations of these sources compared to their designed positions. The difference has been enlarged by a factor of 10 for clarity.
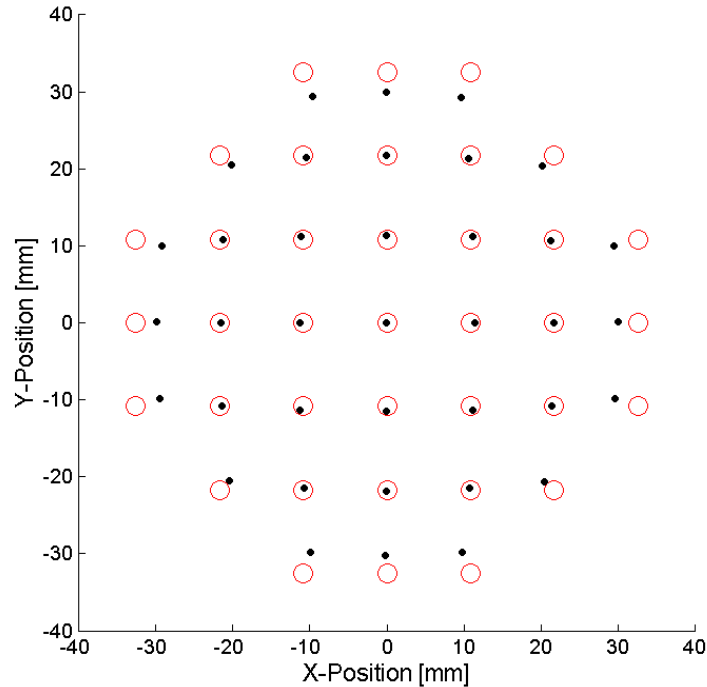
Figure 4-15: Measured global positions of all the seeing limited CU sources (black dots), compared to their designed positions (red circles). The difference between the measured and designed positions is magnified 10 times for clarity

This figure clearly shows the effects of optical distortion within the CU. The interior sources are shifted outward, while the exterior sources are shifted inward. Knowing the measured location of each source within the global coordinate system will be critical for calibrating the remaining NGS pick-off arms (2 and 3). As the global co-ordinates of all three NGSs could be potentially useful for determining the positions of the science targets, the remaining NGS-arms also be calibrated to the global reference frame to ensure their tracking information is accurate. The next sections detail two potential methods for calibrating the remaining NGS-arms: **absolute** and **zonal**.

4.5.3 CALIBRATION OF REMAINING NGS-ARMS

4.5.3.1 ABSOLUTE CALIBRATION OF REMAINING NGS-ARMS

The absolute method for calibrating the remaining NGS arms uses a similar approach to the calibration procedure used for the master arm (NGS-1). Again, three sources from the field are selected and used to create a linear transform and offset. For the remaining arms, any three sources can be used as calibration points, as the global positions of all the seeing limited sources have been measured by the master arm. The calibration sources

chosen for NGS arm-2 and for NGS arm-3 are shown in Figure 4-16 as green circles. They were selected to best represent the areas patrolled by each arm (see Figure 2-10). The yellow circles represent the sources used for quantifying the success of the calibration. The white sources are not expected to be within the regions not patrolled by that specific arm.
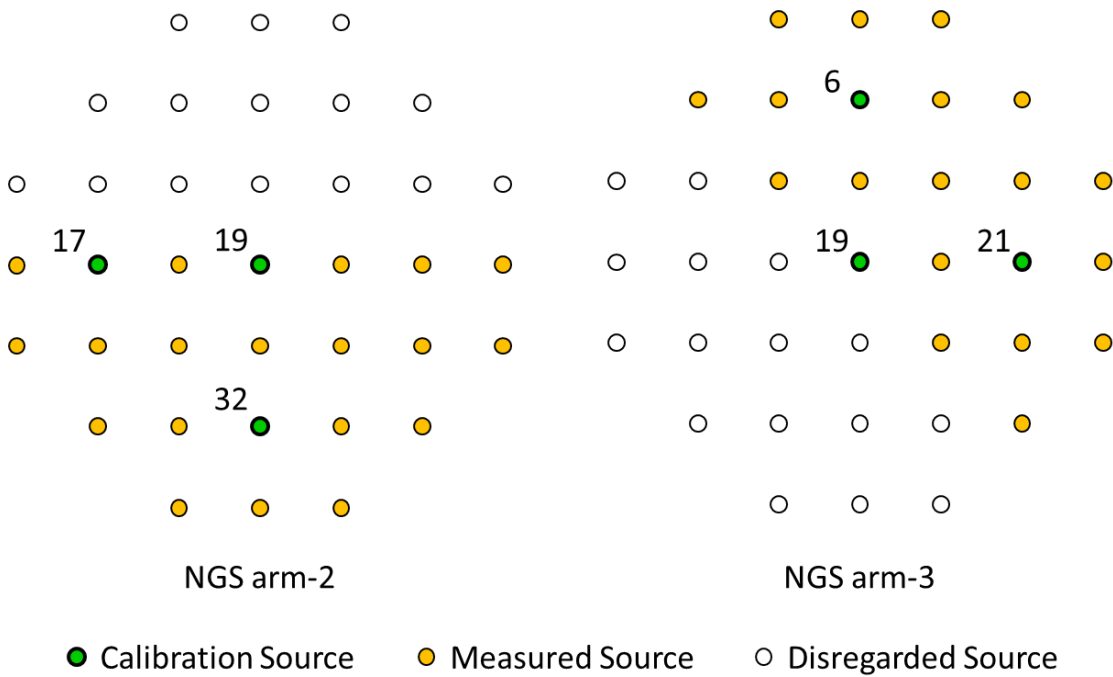
Figure 4-16: Absolute calibration sources used for NGS arm-2 and NGS arm-3. The green sources were used for calibration. The yellow sources are used to quantify the quality of the calibration. The white sources were not used as they are outside the expected motion region of the specific arm

NGS arm-2 and NGS arm-3 were each moved to their calibration sources, and their linear transforms and offsets were calculated using Eqns. 4-13 and 4-14. The results are summarized in Table 4-6.

Table 4-6: Absolute arm calibration values for NGS arm-2 and NGS arm-3

Arm	Linear Transform	Offset [mm]
NGS-2	$[T_{xy \to XY}]_2 = \begin{bmatrix} -1.0042 & 0.0079 \\ -0.0008 & 1.0049 \end{bmatrix}$	$\begin{bmatrix} x_0 \\ y_0 \end{bmatrix}_2 = \begin{bmatrix} 48.016 \\ 68.958 \end{bmatrix}$
NGS-3	$[T_{xy \to XY}]_3 = \begin{bmatrix} 1.0038 & 0.0075 \\ -0.0108 & 1.0038 \end{bmatrix}$	$\begin{bmatrix} x_0 \\ y_0 \end{bmatrix}_3 = \begin{bmatrix} 44.181 \\ 41.768 \end{bmatrix}$

The resulting transforms are similar to the mast arm transform. The ~0.4% scaling seen in the master arm calibration is again shown by both arms, indicating the scale is global. The shear terms again reveal the small angular misalignments between the arm's motion directions and the global axes.

4.5.3.2 ZONAL CALIBRATION OF REMAINING NGS-ARMS

The zonal method utilizes more calibration sources to potentially increase the accuracy of the overall measurements. This method assumes the $T_{xy \rightarrow XY}$ transform and offset terms will have a slight positional dependency. When using this method, the current global NGS position is based on the transform variables created using the three calibration sources surrounding the arm's current location, instead of three absolute sources. Sampling more points for calibration should improve accuracy, but will also increase the time required to perform the arm calibration procedure. With this in mind, Figure 4-17 shows the calibration sources, and the resulting zones, selected for NGS arm-2 and NGS arm-3. The coloring convention for the sources is the same as Figure 4-16.
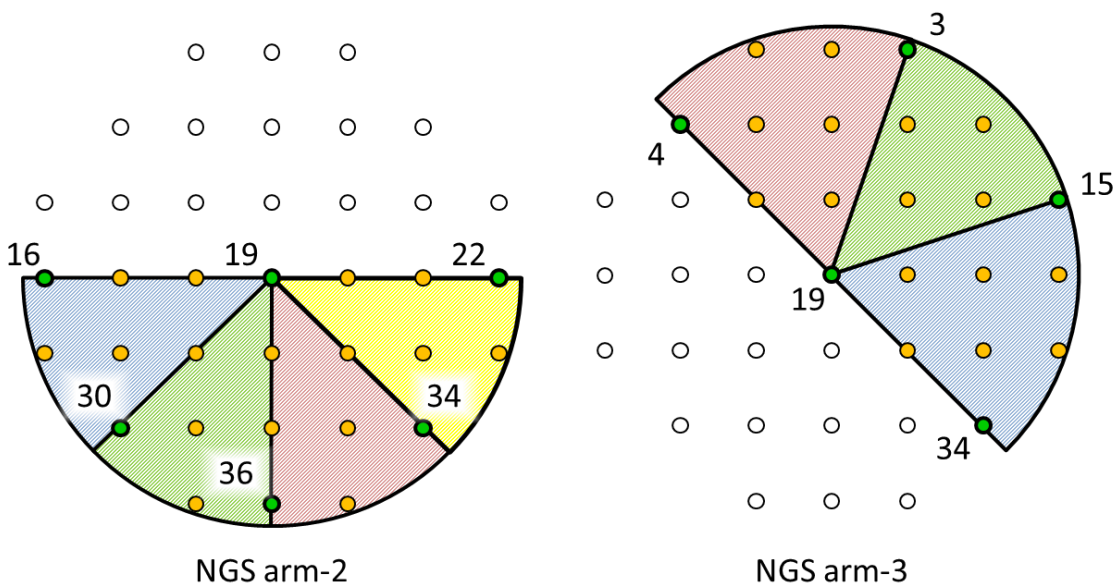
Figure 4-17: Zones (hatched regions) and calibration sources (green circles) used for the zonal calibrating of NGS arm-2 and NGS arm-3. The linear transform used by an arm is based on the three calibration points that define its current zone.

As an example, if NGS arm-2 was positioned in the red zone, its global location would be calculated using the linear transform and offset calculated using sources 19, 34 and 36.

The regions not covered by a zone in the figure are not expected to be patrolled by that particular NGS pick-off arm, as it would be both impractical and a high risk for collision.

4.5.3.3 COMPARING ABSOLUTE AND ZONAL CALIBRATION METHODS

Quantifying the accuracy of both the absolute and zonal methods was done by measuring the local positions of all the relevant seeing limited sources (shown in yellow in Figure 4-16 and Figure 4-17), and converting their positions to a global location based on the specified method. These locations were then compared to their accepted global locations measured by the master am. The results of these tests are shown in Figure 4-18.
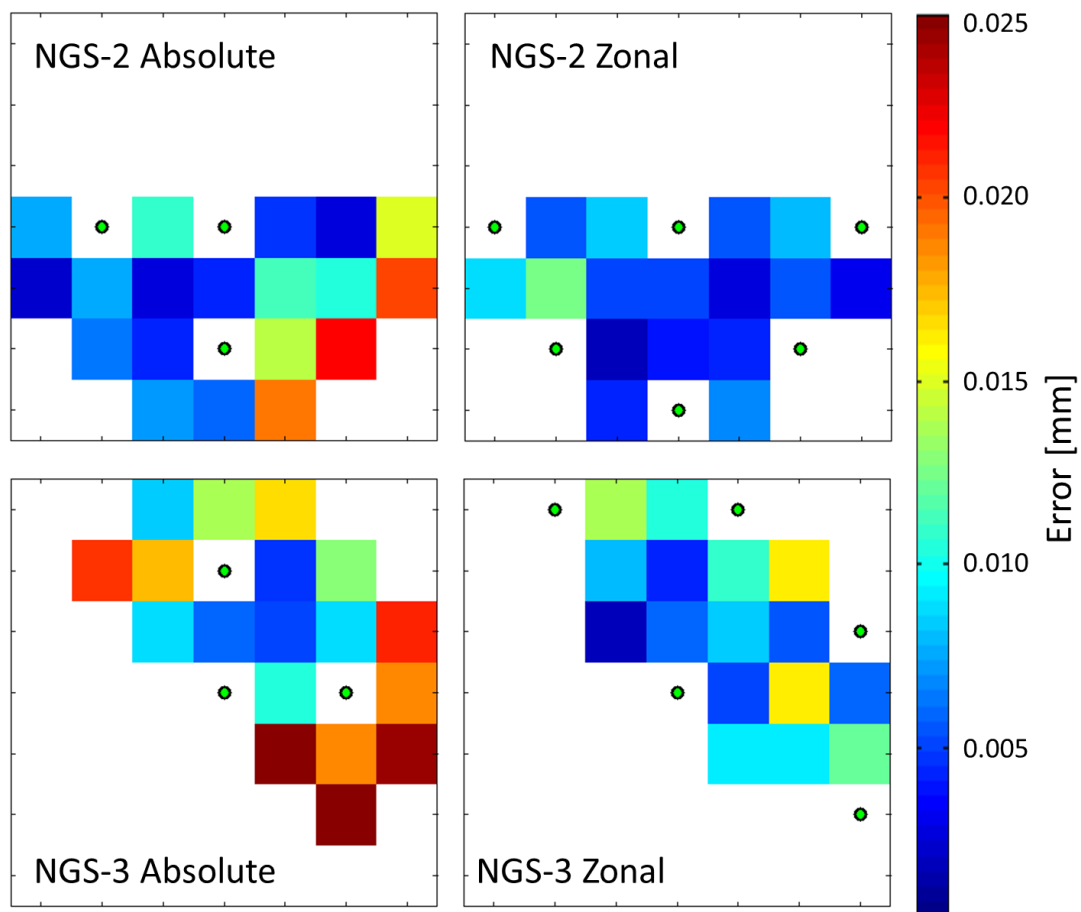
Figure 4-18: Error maps of the absolute and zonal calibration methods for NGS arm-2 and NGS arm-3. The error measurements using the absolute method are quite accurate in the regions within the calibration sources, but are not as accurate toward the outside. The zonal calibration show a lower error over the entire field of interest

It can be seen that the absolute method provides good accuracy (<10 µm) in the regions within the calibration sources, but substantially higher error towards the outside. The

zonal method shows consistently lower error over the entire measurement field. For final comparison, the RMS error and maximum error of these tests is shown in Table 4-7.

Table 4-7: Absolute and zonal calibration accuracy of the NGS pick-off arms

	RMS Error		Maximum Error	
	Absolute	Zonal	Absolute	Zonal
NGS-2	11 μm	6 μm	22 μm	13 μm
NGS-3	18 μm	10 μm	39 μm	16 μm

From these results it is clear that the zonal calibration method should be used for measuring the global location of Raven's remaining NGSs. When using the zonal method, both the RMS error and maximum error are about half of the values measured when using the absolute technique. The exact reason why the transforms differ slightly from zone to zone is unknown, but it is likely due to position-dependent loading conditions on the arms, or subtle variations in the pitch of the lead screws used to move the stages. At this point, the global location of each NGS can be confidently measured using the stage positions of its NGS pick-off arm. Now this information must be used for determining the global locations of the science target.

4.5.4 CALCULATING SCIENCE TARGET LOCATIONS FROM THE NGS LOCATIONS

Three different methods will be discussed for determining the global locations of the science targets from the NGS locations. Each method requires a different number of guide stars to function, and can each be used as the global motion algorithm block shown previously in Figure 4-12. Not surprisingly, linear transforms are employed to solve for the science target locations. Linear transforms were chosen over other methods, such as averaging or interpolating, because the amount of field rotation and telescope tracking error will be readily compensated without additional effort. The transform is shown in Eqn. 4-16.

$$\begin{bmatrix} X \\ Y \end{bmatrix}_i = [T_{Motion}]_i \begin{bmatrix} X \\ Y \end{bmatrix}_0 + \begin{bmatrix} X_{Motion} \\ Y_{Motion} \end{bmatrix}_i \qquad \textbf{4-16}$$

Where $[X \quad Y]_i$ is the global location of a target at time step i, and $[X \quad Y]_0$ is its initial global location at the start of the observation. The $[X_{Motion} \quad Y_{Motion}]_i$ term is the current positional shift of the target, most likely caused by tracking error. The $[T_{Motion}]_i$ term is the transform matrix that will include the effects of field rotation. Within the astronomy community, the values comprising T_{Motion} are commonly referred to as **plate scale modes**[44]. Solving for the motion terms will be the objective of the methods discussed in the following sections. Each method will solve for the motion variables using the measured locations of the NGSs. The current location of the science targets will then be calculated using these terms and their initial locations.

4.5.4.1 THREE NGS METHOD

The first method considered for the global motion algorithm requires the positional information of all three NGSs. Calculating T_{Motion} and the XY_{Motion} terms can then be done using Eqns. 4-17 and 4-18. They were derived in the same way as Eqn. 4-13.

$$[T_{Motion}]_i = \begin{bmatrix} X_1 - X_2 & X_1 - X_3 \\ Y_1 - Y_2 & Y_1 - Y_3 \end{bmatrix}_i \begin{bmatrix} X_1 - X_2 & X_1 - X_3 \\ Y_1 - Y_2 & Y_1 - Y_3 \end{bmatrix}_0^{-1} \qquad \textbf{4-17}$$

$$\begin{bmatrix} X_{Motion} \\ Y_{Motion} \end{bmatrix}_i = \begin{bmatrix} X_1 \\ Y_1 \end{bmatrix}_i - [T_{Motion}] \begin{bmatrix} X_1 \\ Y_1 \end{bmatrix}_0 \qquad \textbf{4-18}$$

Where the numbers (1, 2, 3) represent the index of an NGS arm. With the motion terms now measured, Eqn. 4-16 can be filled in and used to determine the current positions of the science targets, based on their initial positions.

4.5.4.2 TWO NGS METHOD

The linear transform method described in the previous section will not be available if only two NGS arms are in use, with the LGS used as the third source for AO correction. A similar technique can be used assuming the T_{Motion} transform consists only rotation and scaling terms, as shown in Eqn. 4-19.

$$\begin{bmatrix} X \\ Y \end{bmatrix}_i = \begin{bmatrix} \cos\theta & -\sin\theta \\ \sin\theta & \cos\theta \end{bmatrix}_i \begin{bmatrix} S & 0 \\ 0 & S \end{bmatrix}_i \begin{bmatrix} X \\ Y \end{bmatrix}_0 + \begin{bmatrix} X_{Motion} \\ Y_{Motion} \end{bmatrix}_i \qquad \textbf{4-19}$$

The θ, S, and XY motion terms are given by Eqn. 4-20. They based on the current (i) and initial (0) positions of the two available NGS. Their derivations are shown in more detail in Appendix C.

$$\cos\theta = \frac{\Delta X_i \Delta X_0 + \Delta Y_i \Delta Y_0}{\Delta X_i{}^2 \Delta X_0{}^2 + \Delta Y_i{}^2 \Delta Y_0{}^2} \quad \sin\theta = \frac{\Delta Y_i \Delta X_0 - \Delta X_i \Delta Y_0}{\Delta X_i{}^2 \Delta X_0{}^2 + \Delta Y_i{}^2 \Delta Y_0{}^2} \tag{4-20a}$$

$$S = \sqrt{\frac{\Delta X_i{}^2 + \Delta Y_i{}^2}{\Delta X_0{}^2 + \Delta Y_0{}^2}} \tag{4-20b}$$

$$\begin{bmatrix} X_{Motion} \\ Y_{Motion} \end{bmatrix}_i = \begin{bmatrix} X_i \\ Y_i \end{bmatrix} - \begin{bmatrix} \cos\theta & -\sin\theta \\ \sin\theta & \cos\theta \end{bmatrix}_i \begin{bmatrix} S_i & 0 \\ 0 & S_i \end{bmatrix} \begin{bmatrix} X_0 \\ Y_0 \end{bmatrix} \tag{4-20c}$$

$$\text{where:} \quad \begin{matrix} \Delta X_0 = [X_1 - X_2]_0 & \Delta Y_0 = [Y_1 - Y_2]_0 \\ \Delta X_i = [X_1 - X_2]_i & \Delta Y_i = [Y_1 - Y_2]_i \end{matrix}$$

Where the index terms, shown as 1 and 2 in the equations, represent the indices of the NGS arms used to calculate the motion variables. Any combination of two NGS arm could be used for the calculation. The two NGS method should yield similar results compared to the three NGS linear transform method because most of the slow tip/tilt error will be from field rotation and tracking error. The scaling term was selected as the remaining correction mode for this method mostly for lack of a better option. Using it may assist with thermal expansion, as that will potentially globally shrink or expand the instrument, but it will most likely stay very close to unity.

4.5.4.3 ONE NGS METHOD

Using only one NGS to determine the science target locations can be done only if the linear transform matrix is assumed to be entirely created from field rotation, which would need to be pre-computed using Eqn. 1-15, using the specifications of the observation. The motion terms can then be determined using Eqn. 4-21, using the initial and final global positions of the selected NGS arm.

$$\begin{bmatrix} X_{Motion} \\ Y_{Motion} \end{bmatrix}_i = \begin{bmatrix} X_N \\ Y_N \end{bmatrix} - \begin{bmatrix} \cos\theta & -\sin\theta \\ \sin\theta & \cos\theta \end{bmatrix}_i \begin{bmatrix} X_N \\ Y_N \end{bmatrix}_0 \qquad\qquad \textbf{4-21}$$

Where N is the index of the chosen NGS arm.

4.5.5 GENERATING SCIENCE ARM STAGE COMMANDS

With the global locations of the science targets now known, a transform to convert them to local stage commands for the science arms is the final element required before the science arms can be moved. Figure 4-19 shows the geometry of the science arms, specifically noting the variables available for creating the transform. The stage command values, r and θ, are shown in bold. Refer to section 2.4.1 for a description of the science arm's optical and mechanical design.
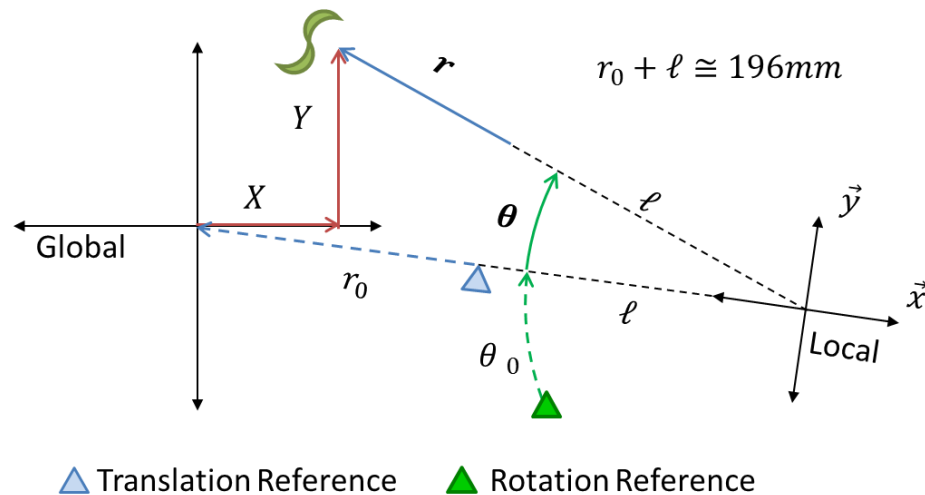
Figure 4-19: Science arm geometry. The local co-ordinate system origin is defined as the axis of the rotation stage. The stage positions when the arm is moved to the central source represent r_0 and θ_0. The distance between the local and global origins is designed to be 196mm.

Each science arm's local origin is defined as the center of its rotation stage axis, and the local x-axis direction as the vector between the local origin and global origin (located at seeing limited source 19). The stage positions when the science-arm is on the central source establish the offset values, r_0 and θ_0, measured relative to their internal references. The distance between the origins is designed to be 196mm, but its accuracy is not guaranteed due to its low priority in Raven's alignment procedure. Consequently, this distance is redefined as the combination of a length term, ℓ, and the radial offset term, r_0.

As the stage positions are in polar co-ordinates, and the global co-ordinates are in Cartesian, a transform between the two is first required:

$$\begin{bmatrix} x \\ y \end{bmatrix}_{local} = \begin{bmatrix} \cos\theta & -\sin\theta \\ \sin\theta & \cos\theta \end{bmatrix} \begin{bmatrix} \ell + r \\ 0 \end{bmatrix} \qquad \textbf{4-22}$$

With the local science arm stage positions now in Cartesian co-ordinates, they can be converted to global coordinates using a linear transform and adding the offset in the same manner as an the NGS arms:

$$\begin{bmatrix} X \\ Y \end{bmatrix}_n = \left[T_{xy \to XY} \right]_n \begin{bmatrix} X \\ y \end{bmatrix}_n = \left[T_{xy \to XY} \right]_n \left(\begin{bmatrix} c\theta & -s\theta \\ s\theta & c\theta \end{bmatrix} \begin{bmatrix} \ell + r \\ 0 \end{bmatrix} + \begin{bmatrix} \ell + r_0 \\ 0 \end{bmatrix} \right) \qquad \textbf{4-23}$$

The offset terms r_0 and θ_0 are measured by moving the arm to source 19 and recording the stage measurements. To increase accuracy a zonal calibration was also performed for the science arms to determine their $T_{xy \to XY}$ transforms. The selected zones and resulting error map for science arm-2 are shown in Figure 4-20.

Sci-2 Calibration Sources

Sci-2 Error Map
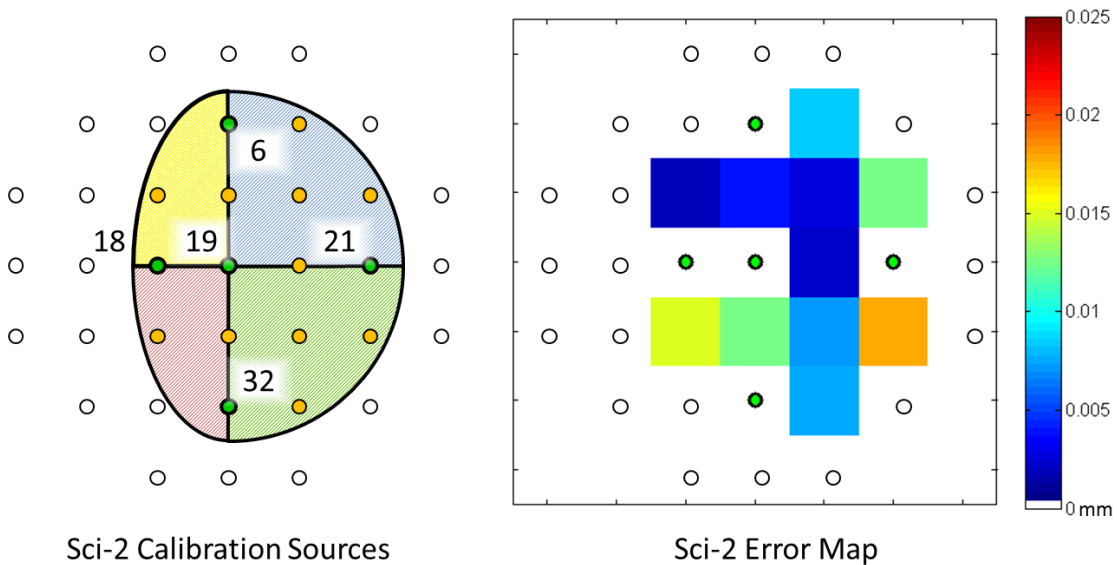
Figure 4-20: Calibration sources and error map for the zonal calibration of science arm-2 using a x_{offset} value of 195.5mm. The calibration sources used for science arm-1 are the left-right flip of the sources used for science arm-2

The calibration sources used for science arm-1 are the left-right flip of the displayed sources used for science arm-2 (6, 17, 19, 20 and 32). The data was initially processed

using an x_{offset} value of 196mm, the designed value, then processed again over a range of values between 192 to 197mm with 0.1mm resolution. For both arms, a minimum RMS error, compared to the known source locations measured by the master arm, occurred when $\ell + r_0$ was set to 195.5mm. The RMS and maximum error of the science arm calibrations are shown in Table 4-8, for both absolute and zonal calibrations.

Table 4-8: Zonal calibration accuracy of the science pick-off arms

	RMS Error [μm]	Max Error [μm]
Science arm-1	13	21
Science arm-2	9	18

These results represent the expected error associated with converting the global science target positions to local science pick-off arm stage commands. They are comparable to the errors associated with the local-to-global conversion of presented in Table 4-7. At this point all of the required calibrations have been performed to convert the NGS pick-off arm stage positions to science pick-off arm stage positions, during an observation.

4.6 CHAPTER SUMMARY

Raven's tip/tilt compensation control system extracts the tip/tilt signals from the OLWFS slope measurements, and then distributed it over the SDMs, TTPs and pick-off arms. Each sub-system requires its own set of temporal filters, spatial transforms, and calibrated linear transforms, which have been discussed in detail. Once Raven is installed and integrated with the Subaru telescope, these systems need to work together to ultimately keep the science targets centered on the IRCS slit. Results of testing these algorithms, using aspects of simulated observations, are discussed in the next chapter.

5 RESULTS

The objective of this chapter is to quantify the expected quality of the Raven instrument's tip/tilt compensation system, while using the methods described throughout this thesis. The results are laid out in the following order:

1. Raven's baseline performance is examined. During these tests, the tip/tilt errors are not simulated, and tip/tilt compensation is turned off. Only simulated turbulence from the CU corrected by the SDMs is analyzed.

2. Using the results from (1), the relationship between tip/tilt errors and overall system performance is established.

3. The TTP-SDM offload is discussed, and its performance is quantified using the standards established in step (2).

4. The accuracy of the pick-off arm target tracking algorithm is discussed, and its performance is also quantified using the standards established in (2).

5. The overall expected performance of Raven's tip/tilt compensation system is discussed.

All of the results in this chapter were taken from tests performed in a laboratory setting, using the CU light sources to create a simulated observation.

5.1 BASELINE ADAPTIVE OPTICS TESTING ON RAVEN

Raven's performance for correcting optical aberrations solely created by atmospheric turbulence needs to be established to serve as a reference for the tip/tilt compensation system's success. Tests were performed using the CU's phase screens to simulate upper atmospheric turbulence, and its CDM to simulate ground layer turbulence. Field rotation and telescope tracking error were not simulated. Additionally, no off-load was sent to the TTPs, and the pick-off arms remained stationary. Figure 5-1 shows images of a diffraction limited CU source, recorded by Raven's science camera, using different AO modes. The images are the average of multiple frames exposed over a 60 second interval. The light from only one source is shown (for reference, a sample science camera image containing both sources is shown in Figure 3-2).
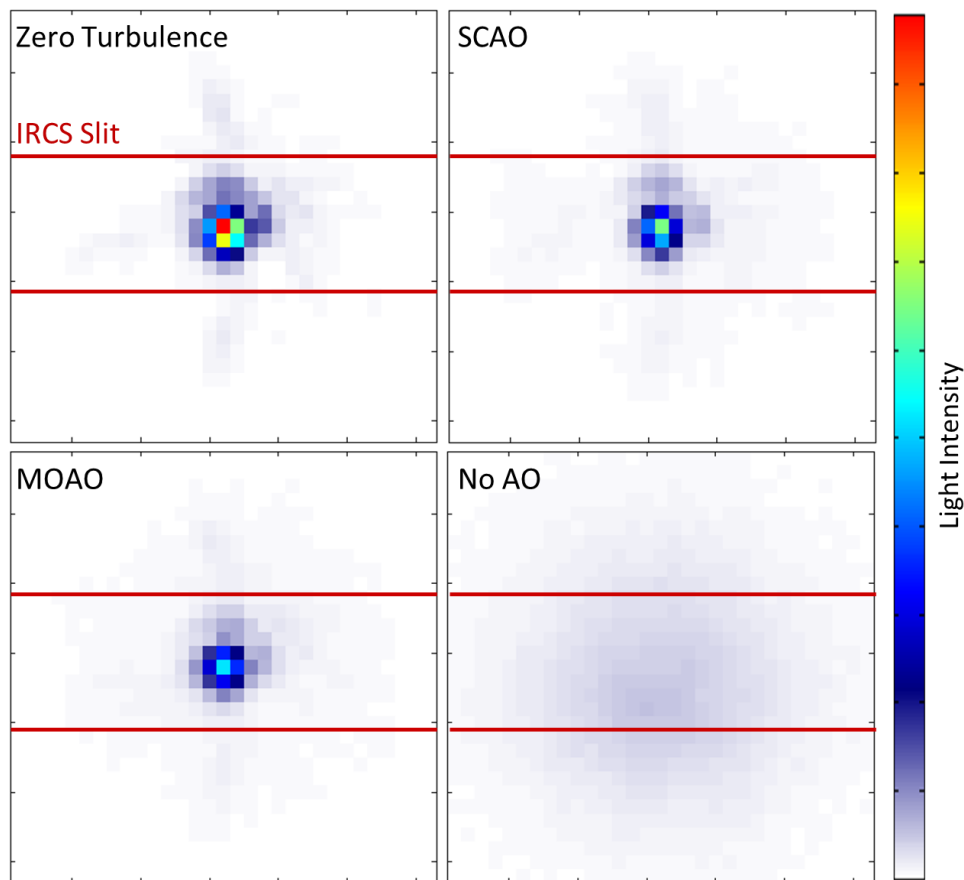
Figure 5-1: Science camera images of a diffraction-limited CU source, for different AO modes. The size of the IRCS slit is shown using the two red lines. The zero turbulence case defines Raven's upper performance limit. The SCAO and MOAO modes show a drop in overall signal intensity compared to the zero turbulence case, but remain sharp. As expected, the signal without Raven's AO correction systems running is very broad and faint.

This data showcases Raven's functionality. In the zero-turbulence case, the image of the source is sharp and bright. The SCAO and MOAO images have slightly less intensity, but remain sharp. Finally the "no AO" image shows that if the target is left uncorrected, the atmospheric turbulence will broadly spread it over the slit[n].

These results are not specifically related to Raven's tip/tilt compensation system, but they do provide a method for establishing a relationship between tip/tilt errors and overall system performance. A tip/tilt error can be simulated by shifting the science camera pixels that represent the IRCS slit. The resulting ensquared energy (EE – see section 1.3)

---

[n] The results for the SCAO and MOAO correction modes are slightly optimistic, as the phase screens used to simulate upper atmospheric turbulence were discovered to be less powerful then required

for various amounts of tip/tilt are shown in Figure 5-2, using the MOAO test results from Figure 5-1. For clarity, the EE calculations used for this figure are normalized relative to the baseline MOAO results, not the zero-turbulence results.
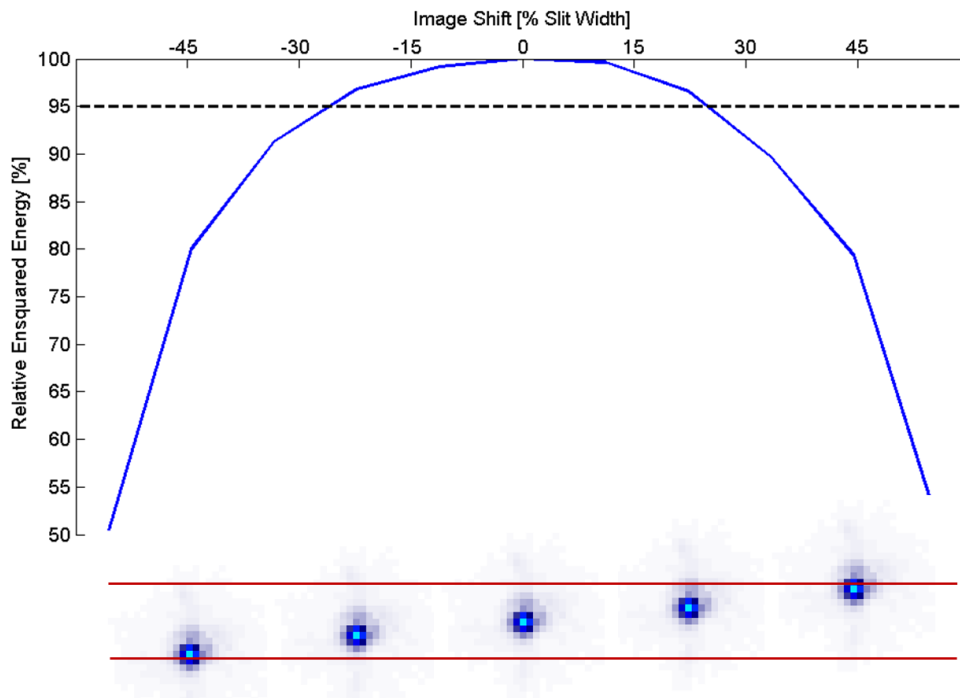
Figure 5-2: Relative ensquared energy measurements for various amounts of image shift using the MOAO mode. To ensure the amount of light passing through the slit is above 95%, image shifts of less than ±25% of the slit width are required, corresponding to an allowable error of 0.042" on sky, or 22 *μm* in the focal plane

This figure shows that if the residual tip/tilt error is less than ±25% of the slit width, 95% of the available corrected science light will pass through the slit, compared to the no tip/tilt case. This result corresponds to 0.042" of tilt on sky, equating to 22 *μm* in the focal plane. The latter value forms a benchmark for the allowable maximum error of Raven's science pick-off arms.

Tip/tilt errors along the direction of the slit does not technically reduce the system's EE, but this effect is not explicitly considered during these tests. As Raven's science path image-rotators could be at any angle, the positional error of the pick-off arms could correspond to any direction on the IRCS slit. Consequently the maximum tip/tilt error is always considered, regardless of direction.

5.2 TTP OFFLOAD RESULTS

The TTP offload system described in section 4.2 was tested using the CU diffraction limited sources. To eliminate potential errors not associated with the offload, testing was performed with zero turbulence, and stationary pick-off arms. A global tip/tilt error was generated by moving the CU's entrance-flip mirror, which is a simple method to equally shift all of the CU's light sources. After each motion step, the system was allowed to settle and data was recorded. Figure 5-3 illustrates the non-offloaded SDM commands, the offloaded SDM commands, and science camera images, for a variety of tip/tilt errors created by shifting the entrance flip mirror. These results are all recorded using Raven's science path-2.
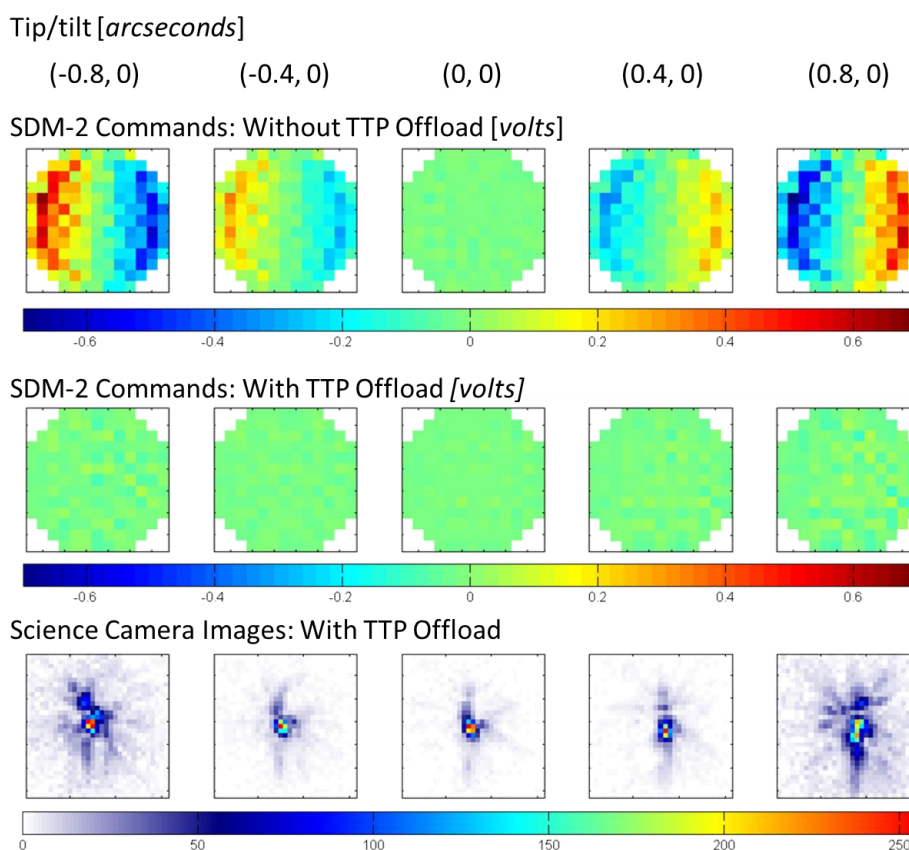
Figure 5-3: Tip/tilt offload testing. A global tip/tilt was generated by shifting the CU entrance flip. The resulting non-offloaded SDM commands, offloaded SDM commands, and offloaded science camera images are shown

These results confirm that the TTP offload algorithm effectively reduces the SDMs' role in tip/tilt correction. This is important because, with the offload running, the SDMs

will be able to more effectively use their actuators to correct high-order optical aberrations. However, when the input tilt is larger than 0.4", it can be seen that the offloaded SDM actuator voltages noticeably increase, and the science camera images show a drop in performance. The pick-off arms must, therefore, track their targets fast enough to prevent a tip/tilt error larger than 0.1" from forming, corresponding to 0.2 mm of error at the focal plane. According to results from section 3.3.2, an RMS tracking error of less than 0.01mm should be readily achievable using the pick-off arms. Consequently it can be expected that the TTP offload system should not negatively impact Raven's overall performance.

The offloaded data additionally shows that for a 0.1" tilt, the science image shifts by ~10% of the IRCS slit width. According to Figure 5-2, this amount of shift will only reduce EE by 1%. This error is most likely due to subtle calibration issues or nonlinearities.

5.3 SCIENCE PICK-OFF ARM TRACKING ACCURACY RESULTS

The tracking accuracy of the science pick-off arms was quantified using the CU's seeing limited light sources, and pinhole mask rotator. The primary objective of these tests was to determine the expected positional error associated with using the NGS arm stage positions to determine the science arm stage positions. The test procedure involved the following steps:

1. The three NGS arms, and two science arms, were each moved to their own seeing limited CU source within the field.
2. Each arm's position was adjusted to remove any tip/tilt, centering them on their sources. The positions the arms' stages were then recorded. As the CU sources are bright, the CLWFSs could be used for centering the science arms on their sources
3. The CU pinhole mask was quickly rotated by 45°, while the arms remained stationary.
4. The arms were moved to the same sources, now in the rotated position, and centered again. The final stage positions were recorded.

Figure 5-4 shows images taken using Raven's acquisition camera of the arms centered on their sources, for both the initial and final positions of the pinhole mask. The sources used for this test were selected to accurately represent a typical observation, with the science targets near the center, surrounded by the NGSs.

0° Field Rotation   45° Field Rotation
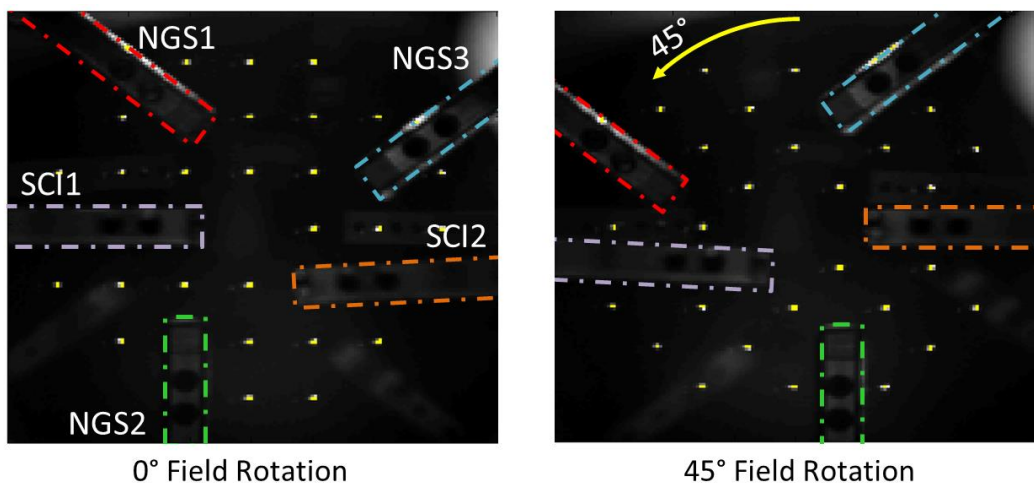
Figure 5-4: Acquisition camera images of the arm accuracy testing procedure. Left: The three NGS arms and two science arms are centered on light sources from the CU, with the pinhole mask in the 0° position. Right: The pinhole mask has rotated to an angle of 45°, and the arms have moved accordingly.

The final measured locations of the science target sources were compared to the locations predicted using the global motion algorithms discussed in section 4.5.4. The results from the three-NGS, two-NGS, and single NGS methods are shown in Table 5-1.

Table 5-1: Pick-off arm global motion algorithm accuracy

Method	NGS-1	NGS-2	NGS-3	SCI-1 Error [μm]	SCI-2 Error [μm]	Offset (x, y) [μm]
Three-NGS	X	X	X	1.2	12.6	(33, 37)
Two-NGS	X	X	-	1.1	11.1	(32, 42)
	X	-	X	11.3	29.1	(25, 33)
	-	X	X	6.9	17.6	(36, 34)
Single-NGS	X	-	-	2.3	11.4	(33, 40)
	-	X	-	3.8	7.8	(34, 45)
	-	-	X	17.7	25.7	(18, 26)

This table shows that similar errors are measured using any method that does not utilize information from NGS arm-3, indicating an issue with its positional accuracy. Overall, these results are acceptable to the project. Assuming NGS-3 is not used, the expected positional accuracy of Raven's blind science target tracking is between 1 and 12 *μm*, for a field rotation of 45°. These values are well below the 22 *μm* maximum tracking error measured in section 5.1. For a 12 *μm* error (0.22" or 16% slit width), only a 3% reduction of light travelling through the slit is expected based on the results from Figure 5-2.

This test isolates the arm tracking to almost a pure field rotation, with a slight measurable shift due to an offset between the pinhole mask's rotation axis and its central pinhole. The mask rotation was done quickly to reduce the potential effects of temperature variations on the bench. Live tracking tests have been performed with similar results to these. The source of NGS arm-3's positional error is unknown, and should be explored further. If NGS arm-3 was repaired, and its positional information was deemed usable, the resulting positional accuracy of the global algorithms using it would be expected to increase. NGS arm-3 was initially selected as the master arm in early 2013, but was subsequently replaced by NGS arm-1 due to its lack of repeatability.

5.4 SECTION SUMMARY

Raven's TTP offload system and pick-off tracking system have been tuned, calibrated and tested. All of the results from this section have shown that their implementation has been successful, and that they should keep the output science image within 25% of the IRCS slit width, and provide 95% EE compared to the no-tip/tilt case. All testing was performed in the laboratory using the CU. The first "engineering night" for Raven to observe on Subaru is scheduled for May 21st, 2014. The objective of this observation is to confirm Raven's laboratory results match the on-sky results; no scientific measurements will be attempted. During this observation, the tip/tilt compensation system's on-sky performance will be recorded and compared to the results found here. Raven's first "science nights" will be in 2015, and the results from these observations will hopefully showcase the viability of MOAO to the astronomy community.

6 CONCLUSIONS AND FUTURE WORK

Raven's tip/tilt compensation system was designed, assembled, calibrated, characterized, and tested. Its performance exceeds the requirements, and it positively contributes to Raven's overall success. Ultimately, the drop in optical throughput to IRCSs slit due to the tip/tilt errors on Raven should be less than 5%. Significant challenges were met, including: field rotation tracking with pick-off arms, SDM/TTP tip/tilt offload, and designing open-loop control architectures. Several aspects of Raven's tip/tilt compensation system could potentially be implemented on future AO systems. Offloading SDM tip/tilt in open-loop, and accurately determining the positional shifts of science targets, are both inherent challenges within the MOAO system architecture which have been adequately solved and demonstrated on Raven.

Moving forward, Raven will start to do scientific observations on Subaru by the middle of 2014, where its main tasks will be to record viable data. This will hopefully excite the astronomy community about MOAO. With luck, Raven's unique tip/tilt

compensation system will add to the debate about the best methods for designing and controlling future MOAO systems.

Though Raven has been successful, there are several areas that still need work. With respect to Raven's tip/tilt compensation system, the following tasks could improve the overall system performance:

1. Implement the hybrid wavefront sensing mode. By using the CLWFS data to remove quasi-static errors, Raven's performance could be improved dramatically. The availability of the hybrid mode on sky will be ultimately dependent on the optical properties of the observed science target and, therefore, will not always be available regardless of its implementation.

2. The source of NGS pick-off arm-3's unpredictable positional errors should be discovered and rectified. The arm should be taken apart and rebuilt to eliminate potential flaws in its construction from being the source of the error. If the error persists, the two PI M-410.DG stages used for moving it could be replaced. Fortunately, as seen in section 5.3, Raven can comfortably work without NGS arm-3's positional information.

3. A robust implementation of the SDM's outer actuators should be attempted. This could be done through accurately modelling the SDM's to create a theoretical interaction matrix, or by a more complicated bench calibration method. The involvement of the SDM's outer actuators would allow them to create larger tip/tilt shapes.

It is the great hope of the Raven team that this project showcases the viability of the MOAO system architecture, and that some of the methods we developed find their way onto future systems used on Extremely Large Telescopes. The tip/tilt compensation system is just one of many critical systems on Raven that needed to be designed, built, and tested in order for the instrument to be a success.

BIBLIOGRAPHY

1. Gilmozzi, Roberto, and Jason Spyromilio. "The 42m European ELT: status." In *SPIE Astronomical Telescopes and Instrumentation*, pp. 701219-701219. International Society for Optics and Photonics, 2008.

2. Nelson, Jerry, and Gary H. Sanders. "TMT status report." In *Astronomical Telescopes and Instrumentation*, pp. 626728-626728. International Society for Optics and Photonics, 2006.

3. Johns, Matt, J. Roger P. Angel, Stephen Shectman, Rebecca Bernstein, Daniel G. Fabricant, Patrick McCarthy, and Mark Phillips. "Status of the giant magellan telescope (GMT) project." In *Astronomical Telescopes and Instrumentation*, pp. 441-453. International Society for Optics and Photonics, 2004.

4. Conan, Rodolphe, Colin Bradley, Olivier Lardière, Celia Blain, Kim Venn, David Andersen, Luc Simard et al. "Raven: a harbinger of multi-object adaptive optics-based instruments at the Subaru Telescope." In *SPIE Astronomical Telescopes and Instrumentation*, pp. 77360T-77360T. International Society for Optics and Photonics, 2010.

5. Kaifu, Norio. "Subaru telescope." In *Astronomical Telescopes & Instrumentation*, pp. 14-22. International Society for Optics and Photonics, 1998.

6. Ciddor, Philip E. "Refractive index of air: new equations for the visible and near infrared." *Applied optics* 35, no. 9 (1996): 1566-1573.

7. Kolmogorov, Andrei N. "The local Structure of turbulence in incompressible viscous fluid for very large Reynolds numbers [In Russian]." In *Dokl. Akad. Nauk SSSR*, vol. 30, pp. 299-303. 1941.

8. Hufnagel, R. E. "Variations of atmospheric turbulence." In *Digest of Technical Papers, Topical Meeting on Optical Propagation through Turbulence*. 1974.

9. Valley, George C. "Isoplanatic degradation of tilt correction and short-term imaging systems." *Applied Optics* 19, no. 4 (1980): 574-577.

10. Olivier, Scot S., and Donald T. Gavel. "Tip-tilt compensation for astronomical imaging." *Journal of the Optical Society of America* 11, no. 1 (1994): 368-378.

11. Roddier, Francois J., Lennox L. Cowie, J. Elon Graves, A. Songaila, Daniel L. McKenna, Jean Vernin, Max Azouit et al. "Seeing at Mauna Kea: a joint UH-UN-NOAO-CFHT study." In *Astronomy'90, Tucson AZ, 11-16 Feb 90*, pp. 485-491. International Society for Optics and Photonics, 1990.

12. Fried, David L. "Statistics of a geometric representation of wavefront distortion." *Journal of the Optical Society of America* 55, no. 11 (1965): 1427-1431.
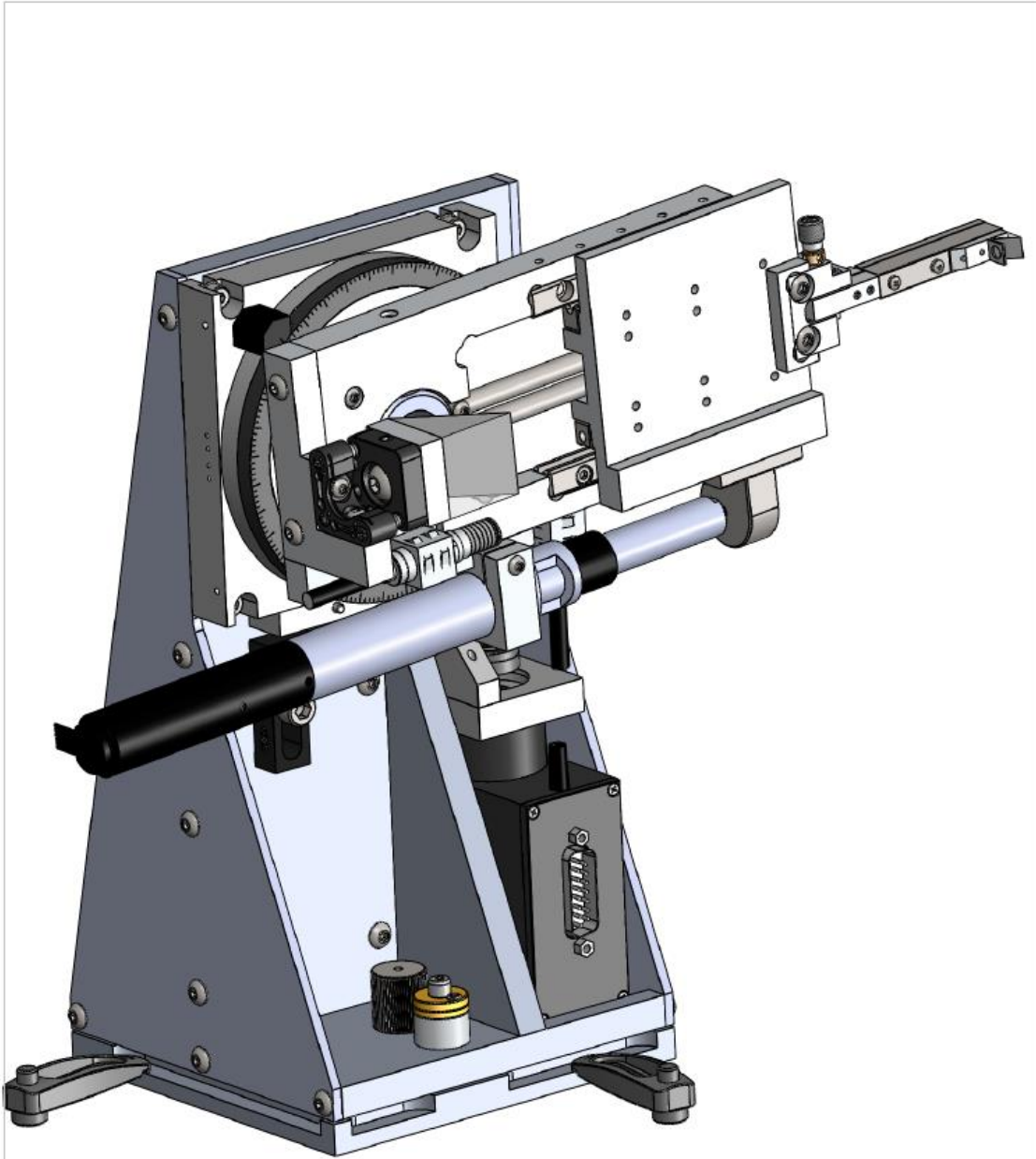
13. Greenwood, Darryl P. "Bandwidth specification for adaptive optics systems." *Journal of the Optical Society of America* 67, no. 3 (1977): 390-393.

14. Bufton, Jack L. "Comparison of vertical profile turbulence structure with stellar observations." *Applied optics* 12, no. 8 (1973): 1785-1793.

15. Fried, David L. "Anisoplanatism in adaptive optics." *Journal of the Optical Society of America* 72, no. 1 (1982): 52-52.

16. Foy, R. "Laser Guide Stars." In *High Angular Resolution in Astrophysics*, pp. 193-229. Springer Netherlands, 1997

17. Michau, Vincent, Thierry Fusco, Jean-Marc Conan, Clelia Robert, Brice Le Roux, and Gerard Rousset. "MCAO for astronomical and near-to-ground applications." In *Optical Science and Technology, the SPIE 49th Annual Meeting*, pp. 170-181. International Society for Optics and Photonics, 2004.

18. Myers, Richard M. "Recent progress and perspectives for GLAO and MOAO." In *SPIE Astronomical Telescopes+ Instrumentation*, pp. 773622-773622. International Society for Optics and Photonics, 2010.

19. Ragazzoni, Roberto, Enrico Marchetti, and Francois Rigaut. "Modal tomography for adaptive optics." *Astronomy and Astrophysics* 342 (1999): L53-L56.

20. Puech, M., H. Flores, M. Lehnert, B. Neichel, T. Fusco, P. Rosati, J-G. Cuby, and G. Rousset. "Coupling MOAO with integral field spectroscopy: specifications for the VLT and the E-ELT." *Monthly Notices of the Royal Astronomical Society* 390, no. 3 (2008): 1089-1104.

21. Eikenberry, Stephen, David Andersen, Rafael Guzman, John Bally, Salvador Cuevas, Murray Fletcher, Rusty Gardhouse et al. "IRMOS: The near-infrared multi-object spectrograph for the TMT." In *Astronomical Telescopes and Instrumentation*, pp. 62695W-62695W. International Society for Optics and Photonics, 2006.

22. Cuby, Jean-Gabriel, Simon Morris, Philip Parr-Burman, Matthew Lehnert, Chris Evans, Thierry Fusco, Pascal Jagourel et al. "EAGLE: an MOAO fed multi-IFU working in the NIR on the E-ELT." In *SPIE Optical Engineering+ Applications*, pp. 74390J-74390J. International Society for Optics and Photonics, 2009.

23. Assémat, Francois, Eric Gendron, and Francois Hammer. "The FALCON concept: multi-object adaptive optics and atmospheric tomography for integral field spectroscopy–principles and performance on an 8-m telescope." *Monthly Notices of the Royal Astronomical Society* 376, no. 1 (2007): 287-312.

24. Andersen, David R., Michael Fischer, Rodolphe Conan, Murray Fletcher, and Jean-Pierre Véran. "VOLT: the Victoria Open Loop Testbed." In *SPIE Astronomical*

Telescopes+ Instrumentation, pp. 70150H-70150H. International Society for Optics and Photonics, 2008.

25. Gavel, Donald, Scott Severson, Brian Bauman, Daren Dillon, Marco Reinig, Christopher Lockwood, Dave Palmer et al. "Villages: an on-sky visible wavelength astronomy AO experiment using a MEMS deformable mirror." In *MOEMS-MEMS 2008 Micro and Nanofabrication*, pp. 688804-688804. International Society for Optics and Photonics, 2008.

26. Myers, Richard M., Zoltán Hubert, Timothy J. Morris, Eric Gendron, Nigel A. Dipper, Aglaé Kellerer, Stephen J. Goodsell et al. "CANARY: the on-sky NGS/LGS MOAO demonstrator for EAGLE." In *SPIE Astronomical Telescopes+ Instrumentation*, pp. 70150E-70150E. International Society for Optics and Photonics, 2008.

27. Noll, Robert J. "Zernike polynomials and atmospheric turbulence." *Journal of the Optical Society of America* 66, no. 3 (1976): 207-211.

28. Tyler, Glenn A. "Bandwidth considerations for tracking through turbulence." *Journal of the Optical Society of America* 11, no. 1 (1994): 358-367.

29. Howell, Steve B. *Handbook of CCD astronomy*. No. 5. Cambridge University Press, 2006.

30. Seidelmann, P. Kenneth, ed. *Explanatory supplement to the astronomical almanac*. University Science Books, 2006.

31. Stone, Ronald C. "An accurate method for computing atmospheric refraction." *Publications of the Astronomical Society of the Pacific* (1996): 1051-1058.

32. Roe, Henry G. "Implications of Atmospheric Differential Refraction for Adaptive Optics Observations1." *Publications of the Astronomical Society of the Pacific* 114, no. 794 (2002): 450-461.

33. Iye, Masanori, Hiroshi Karoji, Hiroyasu Ando, Norio Kaifu, and Keiichi Kodaira. "Current performance and on-going improvements of the 8.2 m Subaru Telescope." arXiv preprint astro-ph/0405012 (2004).

34. http://www.naoj.org/Introduction/telescope.html (accessed March 16, 2014).

35. Lardiere, Olivier, Reston Nash, J. P. Markes, Dave Andersen, Colin Bradley, and Célia Blain. "Final opto-mechanical design of Raven, a MOAO science demonstrator for Subaru." In *Proc. of SPIE Vol*, vol. 8447, pp. 844753-1. 2012.

36. Lamontagne, Frédéric, Min Wang, Jean-François Lavigne, and Marc-André Boucher. "Design of the calibration unit for the MOAO demonstrator Raven." In *Second International Conference on Adaptive Optics for Extremely Large Telescopes. Online at http://ao4elt2. lesia. obspm. fr, id. P6*, vol. 1, p. 6P. 2011.
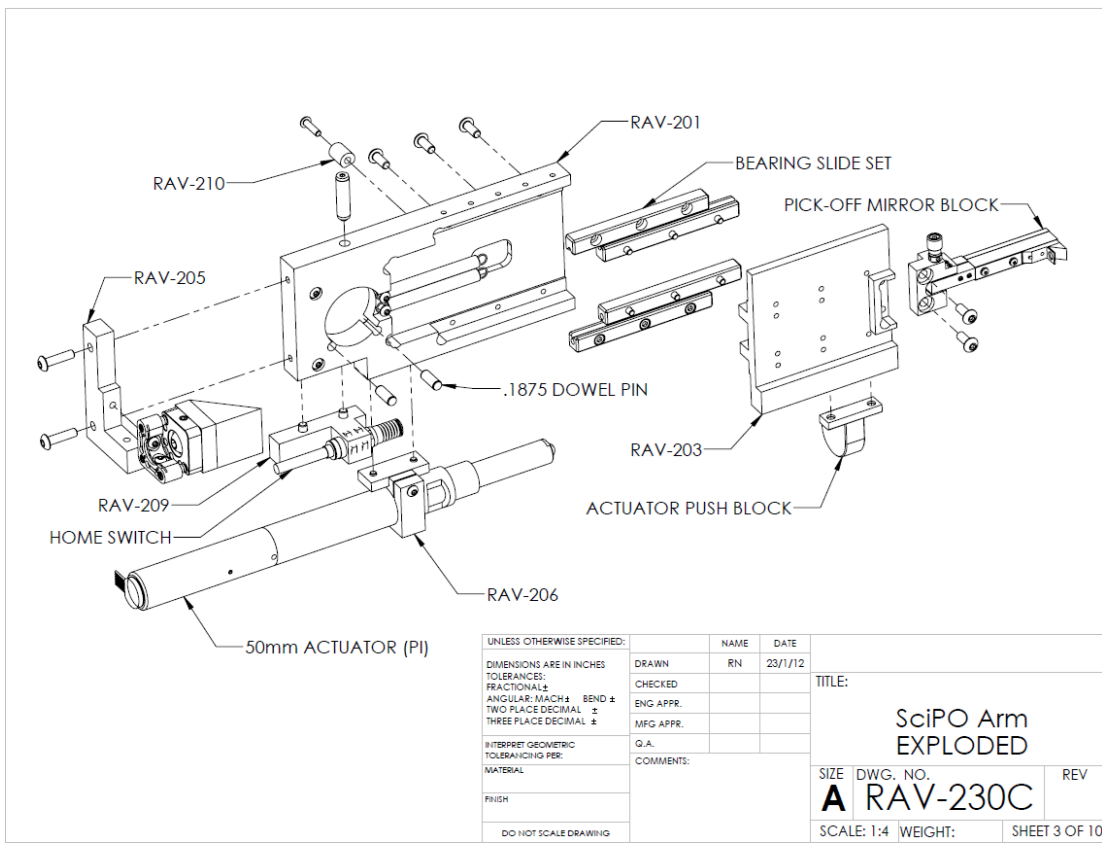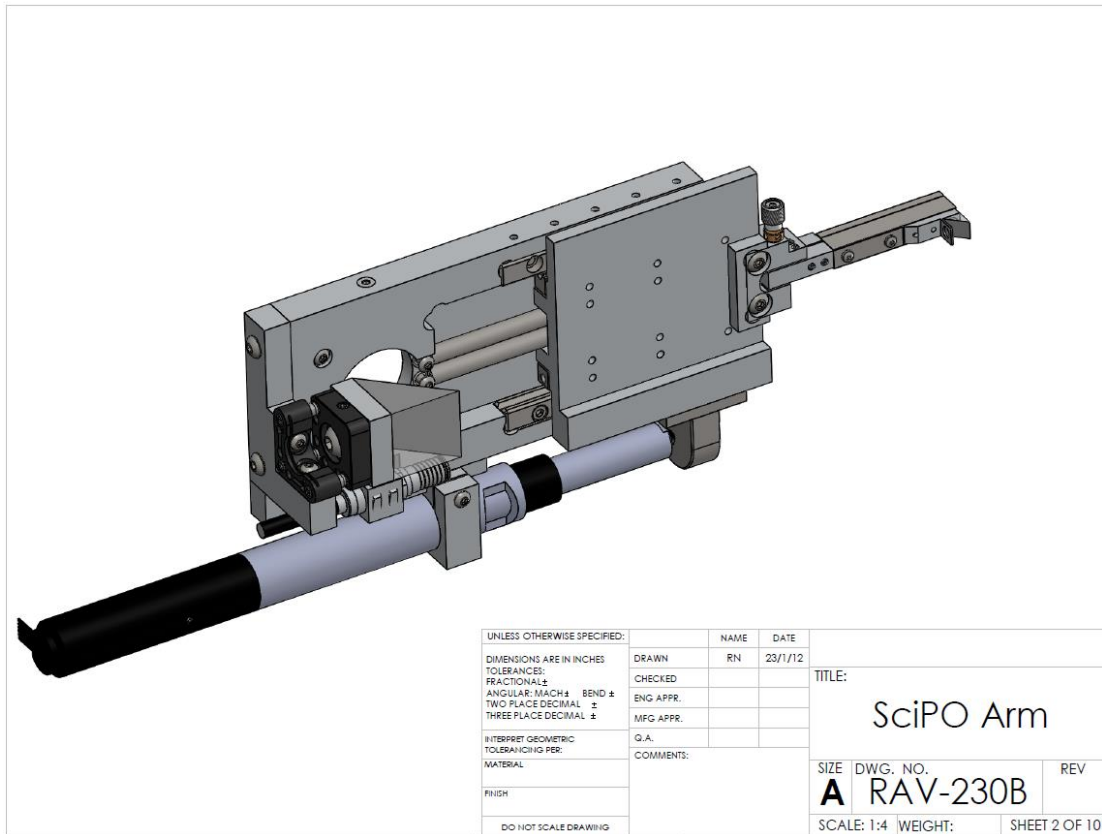
37. Lavigne, J-F., F. Lamontagne, G. Anctil, M. Wang, M. Tremblay, O. Lardiere, R. Nash et al. "Design and test results of the calibration unit for the MOAO demonstrator RAVEN." In *SPIE Astronomical Telescopes+ Instrumentation*, pp. 844754-844754. International Society for Optics and Photonics, 2012.

38. Mantravadi, Samuel V., Troy A. Rhoadarmer, and Robert S. Glas. "Simple laboratory system for generating well-controlled atmospheric-like turbulence." In *Optical Science and Technology, the SPIE 49th Annual Meeting*, pp. 290-300. International Society for Optics and Photonics, 2004.

39. Guyon, Olivier. "High Sensitivity Wavefront Sensing with a Nonlinear Curvature Wavefront Sensor." *Publications of the Astronomical Society of the Pacific* 122, no. 887 (2010): 49-62.

40. Esposito, Simone, and Armando Riccardi. "Pyramid Wavefront Sensor behavior in partial correction Adaptive Optic systems." *ASTRONOMY AND ASTROPHYSICS-BERLIN-* 369, no. 2 (2001): L9-L12.

41. Blain, Celia, Rodolphe Conan, Colin Bradley, Onur Keskin, Peter Hampton, and Aaron Hilton. "Magnetic ALPAO and piezo-stack CILAS deformable mirrors characterization." In *Adaptive Optics: Methods, Analysis and Applications*, p. ATuC6. Optical Society of America, 2007.

42. Andersen, David R., Kate J. Jackson, Célia Blain, Colin Bradley, Carlos Correia, Meguru Ito, Olivier Lardière, and Jean-Pierre Véran. "Performance modeling for the raven multi-object adaptive optics demonstrator." *Publications of the Astronomical Society of the Pacific* 124, no. 915 (2012): 469-484.

43. Jackson, Kate, Carlos Correia, Olivier Lardière, David Andersen, and Colin Bradley. "Tomographic wavefront error estimation and measurement for Raven, a multi-object adaptive optics demonstrator." In *SPIE Astronomical Telescopes+ Instrumentation*, pp. 84475F-84475F. International Society for Optics and Photonics, 2012.

44. Herriot, Glen, David Andersen, Jenny Atwood, Peter Byrnes, Marc-André Boucher, Corinne Boyer, Kris Caputa et al. "TMT NFIRAOS: adaptive optics system for the Thirty Meter Telescope." In *SPIE Astronomical Telescopes+ Instrumentation*, pp. 84471M-84471M. International Society for Optics and Photonics, 2012.
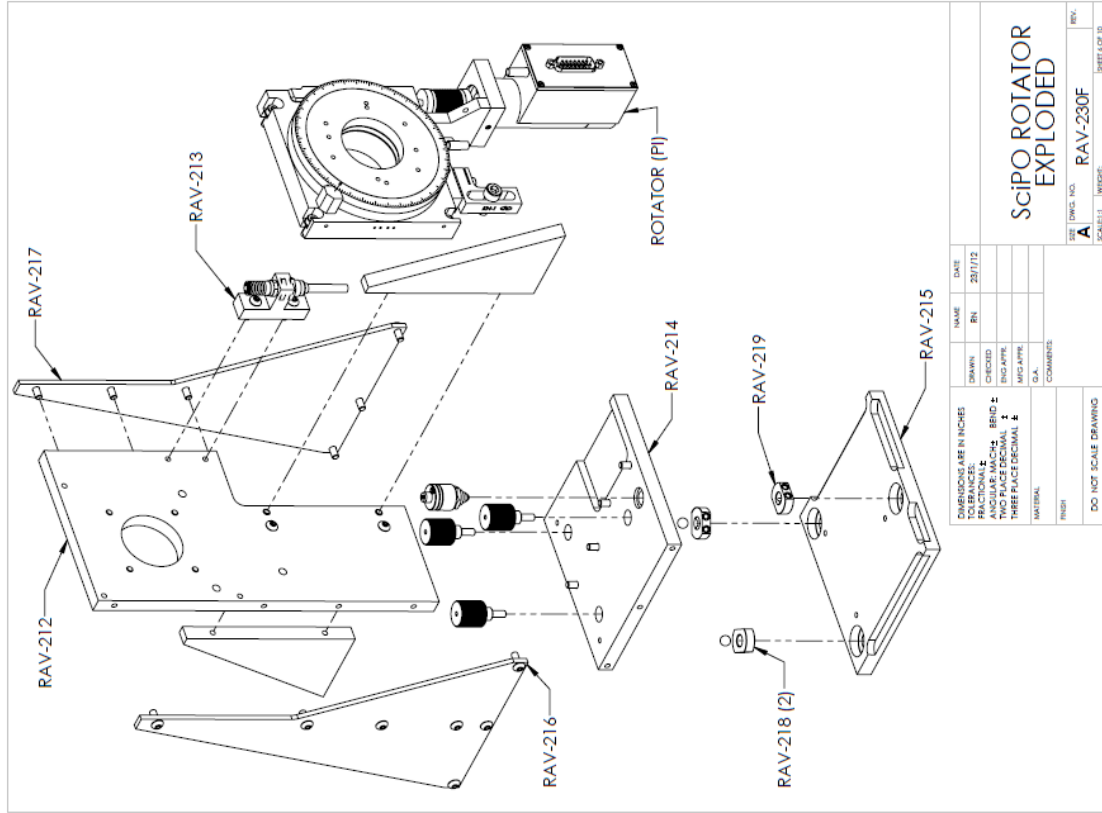
APPENDIX A

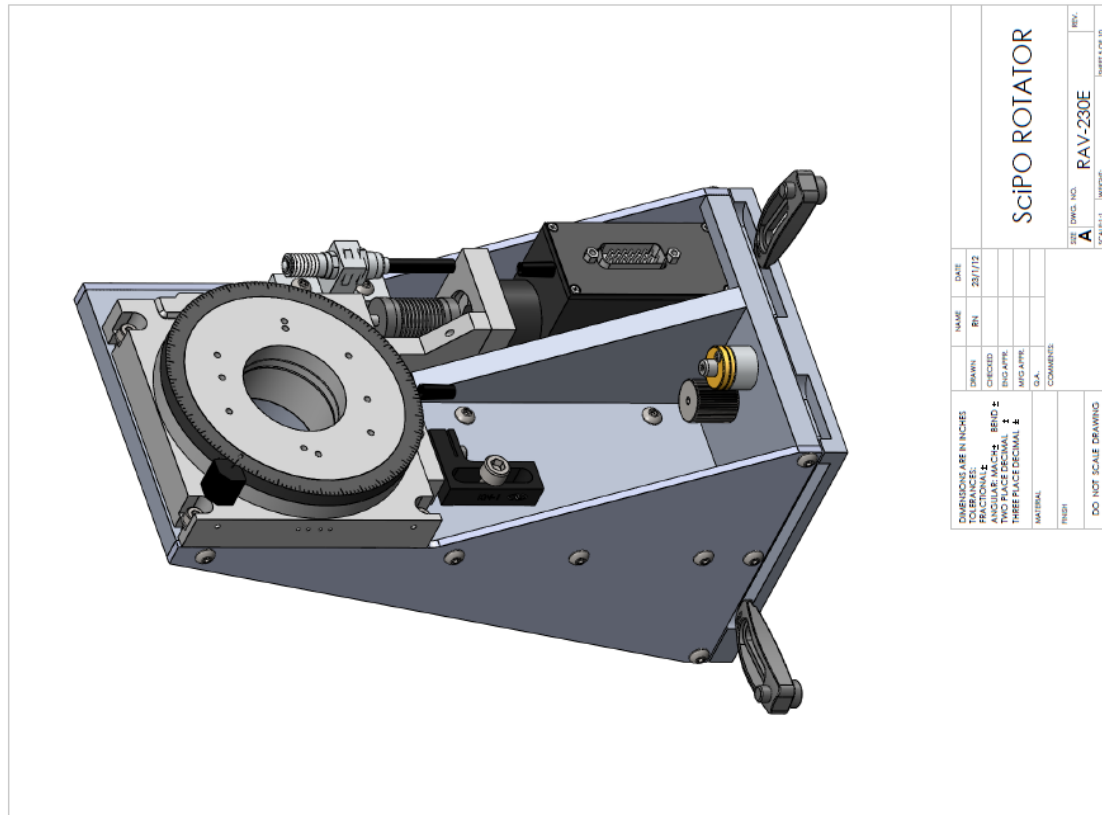## SCIENCE PICK-OFF ASSEMBLY DRAWINGS

UNLESS OTHERWISE SPECIFIED:		NAME	DATE			
DIMENSIONS ARE IN INCHES	DRAWN	RN	23/1/12			
TOLERANCES: FRACTIONAL± ANGULAR: MACH± BEND ± TWO PLACE DECIMAL ± THREE PLACE DECIMAL ±	CHECKED			TITLE:		
	ENG APPR.					
	MFG APPR.			SciPO Arm		
INTERPRET GEOMETRIC TOLERANCING PER:	Q.A.					
MATERIAL	COMMENTS:					
				SIZE	DWG. NO.	REV
FINISH				A	RAV-230B	
DO NOT SCALE DRAWING				SCALE: 1:4	WEIGHT:	SHEET 2 OF 10

RAV-201
RAV-210
BEARING SLIDE SET
PICK-OFF MIRROR BLOCK
RAV-205
.1875 DOWEL PIN
RAV-203
ACTUATOR PUSH BLOCK
RAV-209
HOME SWITCH
RAV-206
50mm ACTUATOR (PI)

UNLESS OTHERWISE SPECIFIED:		NAME	DATE			
DIMENSIONS ARE IN INCHES	DRAWN	RN	23/1/12			
TOLERANCES: FRACTIONAL± ANGULAR: MACH± BEND ± TWO PLACE DECIMAL ± THREE PLACE DECIMAL ±	CHECKED			TITLE:		
	ENG APPR.					
	MFG APPR.			SciPO Arm EXPLODED		
INTERPRET GEOMETRIC TOLERANCING PER:	Q.A.					
MATERIAL	COMMENTS:					
				SIZE	DWG. NO.	REV
FINISH				A	RAV-230C	
DO NOT SCALE DRAWING				SCALE: 1:4	WEIGHT:	SHEET 3 OF 10

RAV-217
RAV-213
ROTATOR (PI)
RAV-214
RAV-219
RAV-215
RAV-212
RAV-216
RAV-218 (2)

SciPO ROTATOR
EXPLODED
RAV-230F

SciPO ROTATOR
RAV-230E

APPENDIX B

DIGITAL FILTER DESIGN

Digital filters are used for modifying the frequency response of an output signal compared to its input signal. They are useful for attenuating noise, smoothing data, preventing resonance, and distributing or combining signals. For digital systems like the RTC, filters create the current output signal by combining previous output signal values with current and previous input values. The generic equation for an n-order digital filter with input signal x output and signal y at time-step i is as follows:

$$y_i = a_1 y_{i-1} + a_2 y_{i-2} + \cdots + a_n y_{i-n} + b_0 x_i + b_1 x_{i-1} + \cdots + b_n x_{i-n}$$

Where a and b are coefficients chosen to best implement the filters desired properties. Raven's utilizes several **low-pass filters** and **high-pass** filters. Low-pass filters attenuate input signals with frequencies higher than their **cut-off frequency**, and high-pass filters attenuate input signals with frequencies lower than their cut-off frequency. The signal attenuation at the cut-off frequency is by definition 50% or -3dB ($10^{-3/10} \cong 0.5$). Increasing the filter order will more steeply attenuated signals past the cut-off frequency, but impart a larger phase error (lag). Tools like Matlab can be used to select the filter coefficients depending on the desired filter style and design parameters. As an example, the magnitude and phase plot of a second order low-pass Butterworth filter with a cut-off frequency of 12.5 Hz and a sampling frequency of 250Hz is shown in Figure A-6-1.
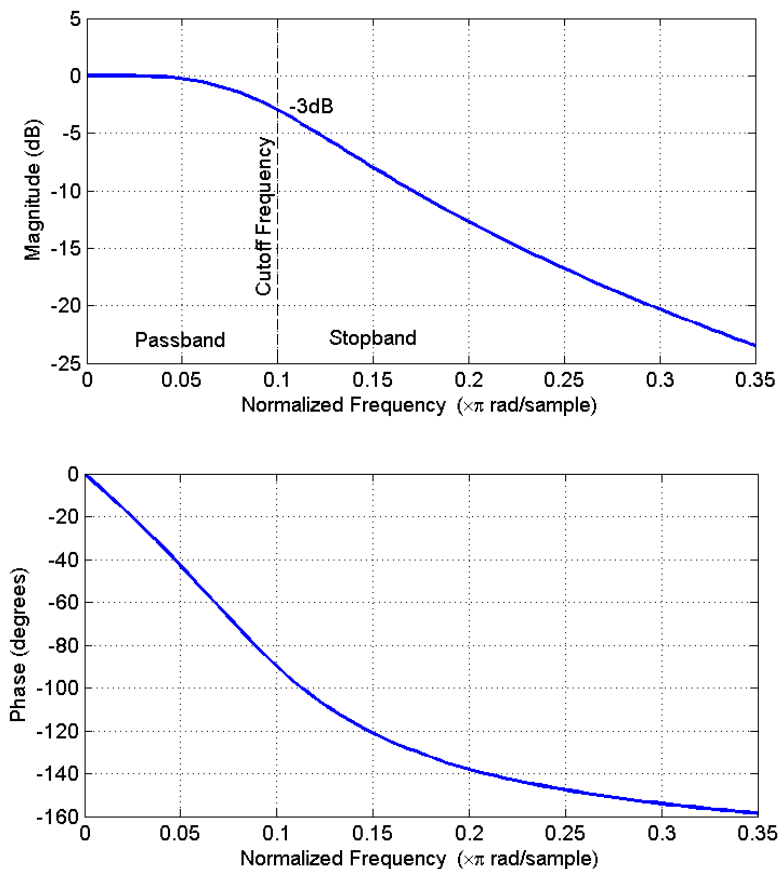
Figure A-6-1: Bode Plot of a second order low-pass Butterworth filter with a cut-off frequency of 12.5Hz. Data is sampled at a frequency of 250Hz. Frequencies in the pass-band are mostly unaffected by the filter, and frequencies in the stop-band are attenuated. The cut-off frequency occurs when the signal has been attenuated by 3dB. (a_1 = -1.56, a_2 = 0.64, b_0 = 0.42, b_1 = 0.04, b_2 = 0.20)

The magnitude plot shows that input frequencies within the **pass band** will not be significantly affected. Alternatively, input signals within the **stop band** will be attenuated. The phase plot shows a phase lag that increases with frequency. Sample data put through a low-pass filter and a high-pass filter with the same corner frequency is shown in Figure A-6-2.
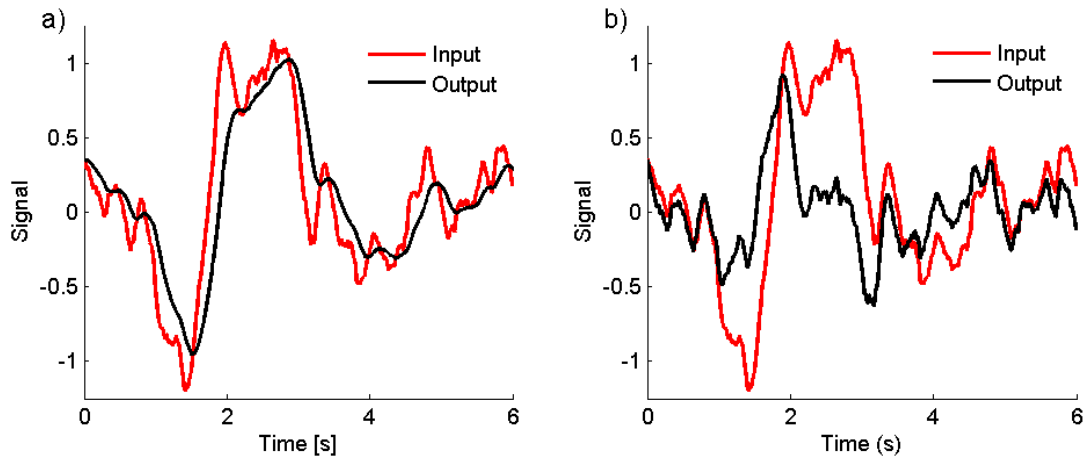
Figure A-6-2: a) Low Pass Filtered Data. The output (black line) follows the slower component of the input (red), smoothing it but creating a phase delay. b) High Pass Filtered Data. The output responds to the faster component of the input, but does not follow the same overall trend

Second-order Butterworth filters similar to the one described above are used throughout Raven because of their simplicity and flat pass-band. All Filter coefficients were generated using the Matlab *butter* function.

APPENDIX C

DERIVATION OF TWO-NGS LINEAR TRANSFORM EQUATIONS

Linear transform equation for field rotation, global scaling and offset:

$$\begin{bmatrix} X \\ Y \end{bmatrix}_i = \begin{bmatrix} \cos\theta & -\sin\theta \\ \sin\theta & \cos\theta \end{bmatrix}_i \begin{bmatrix} S & 0 \\ 0 & S \end{bmatrix}_i \begin{bmatrix} X \\ Y \end{bmatrix}_0 + \begin{bmatrix} X_{Offset} \\ Y_{Offset} \end{bmatrix}_i$$

The equation is the same for the two NGS being used:

$$\begin{bmatrix} X_1 \\ Y_1 \end{bmatrix}_i = \begin{bmatrix} \cos\theta & -\sin\theta \\ \sin\theta & \cos\theta \end{bmatrix}_i \begin{bmatrix} S & 0 \\ 0 & S \end{bmatrix}_i \begin{bmatrix} X_1 \\ Y_1 \end{bmatrix}_0 + \begin{bmatrix} X_{Offset} \\ Y_{Offset} \end{bmatrix}_i$$

$$\begin{bmatrix} X_2 \\ Y_2 \end{bmatrix}_i = \begin{bmatrix} \cos\theta & -\sin\theta \\ \sin\theta & \cos\theta \end{bmatrix}_i \begin{bmatrix} S & 0 \\ 0 & S \end{bmatrix}_i \begin{bmatrix} X_2 \\ Y_2 \end{bmatrix}_0 + \begin{bmatrix} X_{Offset} \\ Y_{Offset} \end{bmatrix}_i$$

Subtract one from another:

$$\Delta X_0 = [X_1 - X_2]_0 \quad \Delta Y_0 = [Y_1 - Y_2]_0$$
$$\Delta X_i = [X_1 - X_2]_i \quad \Delta Y_i = [Y_1 - Y_2]_i$$

$$\begin{bmatrix} \Delta X \\ \Delta Y \end{bmatrix}_i = \begin{bmatrix} \cos\theta & -\sin\theta \\ \sin\theta & \cos\theta \end{bmatrix} \begin{bmatrix} S & 0 \\ 0 & S \end{bmatrix} \begin{bmatrix} \Delta X \\ \Delta Y \end{bmatrix}_0$$

Multiply to create two equations:

$$\Delta X_i = S(\cos\theta\,\Delta X_0 - \sin\theta\,\Delta Y_0)$$
$$\Delta Y_i = S(\sin\theta\,\Delta X_0 + \cos\theta\,\Delta Y_0)$$

Divide to remove scaling term:

$$\frac{\Delta X_i}{\Delta Y_i} = \frac{\cos\theta\,\Delta X_0 - \sin\theta\,\Delta Y_0}{\cos\theta\,\Delta Y_0 + \sin\theta\,\Delta X_0}$$

Divide by $\cos\theta$ to remove $\sin\theta$ terms:

$$\frac{\Delta X_i}{\Delta Y_i} = \frac{\Delta X_0 - \tan\theta\,\Delta Y_0}{\Delta Y_0 + \tan\theta\,\Delta X_0}$$

Solve for $\tan\theta$:

$$\tan\theta = \frac{\Delta Y_i \Delta X_0 - \Delta X_i \Delta Y_0}{\Delta X_i \Delta X_0 + \Delta Y_i \Delta Y_0}$$

Use result to solve for $\sin\theta$ and $\cos\theta$:

$$\sin \theta = \frac{\Delta Y_i \Delta X_0 - \Delta X_i \Delta Y_0}{\Delta X_i{}^2 \Delta X_0{}^2 + \Delta Y_i{}^2 \Delta Y_0{}^2}$$

$$\cos \theta = \frac{\Delta X_i \Delta X_0 + \Delta Y_i \Delta Y_0}{\Delta X_i{}^2 \Delta X_0{}^2 + \Delta Y_i{}^2 \Delta Y_0{}^2}$$

With the angular terms solved, the scaling term is easily derived by inserting it into a previous equation:

$$S = \sqrt{\frac{\Delta X_i{}^2 + \Delta Y_i{}^2}{\Delta X_0{}^2 + \Delta Y_0{}^2}}$$